Structure and Properties of Layered Intermetallic Compounds and Supertetrahedral Phosphidosilicates

Dissertation von Peiqi Chen

München 2025

Dissertation zur Erlangung des Doktorgrades
der Fakultät für Chemie und Pharmazie
der Ludwig-Maximilians-Universität München

Structure and Properties of Layered Intermetallic Compounds and Supertetrahedral Phosphidosilicates

Peiqi Chen

aus

Shenzhen, China

2025

Erklärung

Diese Dissertation wurde im Sinne von §7 der Promotionsordnung vom 28. November 2011 von Herrn Prof. Dr. Dirk Johrendt betreut.

Eidesstattliche Versicherung

Diese Dissertation wurde eigenständig und ohne unerlaubte Hilfe erarbeitet.KI-basierte Werkzeuge (ChatGPT) wurden ausschließlich zur sprachlichen Glättung und formalen Überarbeitung verwendet; inhaltliche Analysen und wissenschaftliche Ergebnisse stammen allein von der Verfasserin/dem Verfasser.

München, November 24, 2025

Peiqi Chen

Dissertation eingereicht am:	01.10.2025
1. Gutachter:	Prof. Dr. Dirk Johrendt
2. Gutachter:	Prof. Dr. Constantin Hoch
Mündliche Prüfung am:	13.11.2025

Danksagung

My special thanks go to Prof. Dr. Dirk Johrendt for giving me the opportunity to complete my doctoral thesis in his research group. I would also like to thank him for the freedom to implement my research ideas, for the constructive expert discussions and suggestions regarding these topics, and for the opportunity to participate in conferences.

I would like to thank all members of the Johrendt working group (AK Johrendt), whom I got to know over the past few years and who have enriched everyday lab life: Arthur Haffner, Catrin Löhnert, Marlo Schöneich, Martin Weidemann, and Valentin Weippert, for the warm welcome into the team, their constant willingness to help, and the pleasant working atmosphere. I would especially like to thank our “Muddi” Catrin Löhnert, who always cared deeply about each one of us. She generously shared her experience and gave us so much advice — both scientific and personal. Even after her retirement, her presence and support left a lasting impact on me personally.

A very special thank you goes to Nadine, who was always there with an open ear and an open heart. She cared deeply, listened patiently, and helped me navigate not just the challenges of my PhD, but life itself during this time. Her presence gave me strength when I needed it most, and I’m endlessly grateful for her unwavering support.

Bettina, Valentin, and Arthur, who each graduated during the first two years of my PhD, helped me understand how everything worked in the lab and made the beginning of this journey much easier. I would also like to thank Marlo for guiding me from the very beginning of my lab work and showing me the different parts of our lab with so much patience. Martin brought warmth and mystery, always kind in his own quiet way. Dominik was incredibly patient, whether it was helping repair the EDX or explaining theory — I learned a lot from him. Kristian, though always busy, was full of ideas and gave me great help with crystal structures. And Julian, during the last year of my PhD, it was great fun working on the same topic with him, sharing ideas and getting his thoughtful suggestions. Thahn, not officially in our group but always around, was a constant presence — friendly, helpful, and a part of our everyday life. I came here far from home, hesitant and afraid to ask questions at first, but everyone in the group encouraged me to be curious, to speak up, and to grow. This support helped me overcome cultural barriers and truly feel like I belonged — for that, I thank you all from the bottom of my heart.

I am very grateful to my intern Chuyi Liu for her contributions to my dissertation.

I would also like to thank the former and current members of the Schnick, Hoch, and Lotsch research groups for the pleasant working atmosphere, many beautiful moments, and

the exciting and helpful discussions during coffee breaks.

Thomas Müller, Dieter Rau, and Wolfgang Wünschheim—I thank you for always helping me with technical problems quickly and without complications. I would especially like to thank Wolfgang for always being there for me and for his numerous helpful tips. I would also like to thank the Zeiss equipment repair team.

Finally, I would like to thank my family and my friends who supported me not only during this thesis but throughout my studies. Without the fun adventures and vacations, the time during my studies and this doctoral thesis would not have passed as quickly. I want to thank my family for their financial and emotional support. Thank you for their encouraging words and open ears during all kinds of challenges.

My very special thanks go to Wenhan, my boyfriend. I feel so lucky to have met him in Munich, in this wonderful place that brought us together. His understanding, patience, and encouragement carried me through all the difficulties, highs, and lows of my studies and this doctoral thesis. Thank you for always believing in me and for being someone I can truly rely on.

Contents

Chapter 1

Introduction

The discovery of novel quantum and energy materials remains a central theme in chemistry and physics. Among these, two rapidly developing and technologically relevant areas are the search for new superconductors with topological or layered structural features and the development of advanced solid-state electrolytes for next-generation batteries. This thesis explores both fronts through the investigation of two distinct structural families: honeycomb-derived intermetallic compounds and supertetrahedral phosphidosilicates.

The RTX intermetallic compounds ($R =$ rare earth, $T =$ transition metal, $X =$ p-block element) are a structurally and chemically diverse class of materials, known to crystallize in more than 30 different structure types, including CeFeSi-, ZrNiAl-, and TiNiSi-type frameworks [1]. Their structural flexibility allows the formation of layered motifs, honeycomb networks, and polymorphic variants that are highly sensitive to pressure, temperature, and composition. Depending on the specific R, T, and X components, these compounds exhibit a wide range of magnetic and electronic behaviors such as Kondo interactions, intermediate valence states, heavy fermion behavior, and even unconventional superconductivity. In particular, the realization of honeycomb lattices in RTX systems provides an exciting platform for exploring Dirac physics and potential topological superconductivity.

Parallel to this, the demand for safer and higher energy-density batteries has sparked interest in all-solid-state batteries (ASSBs), where solid electrolytes replace flammable liquid counterparts. A critical requirement for solid electrolytes is high ionic conductivity, which is strongly influenced by the underlying crystal structure. Recently, phosphidosilicates—especially those built from SiP_4 tetrahedra—have attracted attention due to their structural tunability and framework openness. For instance, $Li_{10}Si_2P_6$, $Li_3Si_3P_7$ and $Li_{14}SiP_6$ with conductivities reaching 10^{-3} $S\,cm^{-1}$ [2, 3]. Furthermore, the extension to sodium and potassium analogues opens a path toward sustainable and earth-abundant alternatives to lithium-ion technologies.

The initial aim of this thesis was to synthesize layered intermetallic compounds that could potentially host superconductivity and to explore novel A–Si–P phosphidosilicates as solid electrolytes. Although superconductivity was not observed in the synthesized RPtAs and AEPtPn compounds, their structural richness and physical properties contribute valuable insights into the broader landscape of honeycomb-derived intermetallics. Similarly, the structural motifs discovered in the supertetrahedron phosphidosilicates provide a basis for future investigations into alkali-ion conductors with tunable frameworks.

1.1 Crystal chemistry and Physical properties of pnictides with layered structures

To place these results within a broader structural context, it is instructive to recall that the AlB_2 structure type, first determined in 1935 by Hoffmann [4], represents one of the simplest inorganic structure types. It crystallizes in space group $P6/mmm$ (No.191) with Al atoms on the $1a$ site and B atoms forming trigonal-prismatic hexagonal nets on the $2d$ site. Owing to this archetypal honeycomb arrangement, 46 binary and ternary intermetallic structure types have been derived from AlB_2. For binary RT_2 and RX_2 as well as ternary RTX, R_2TX_3, and $R_3T_2X_4$ compounds (R = alkaline earth, rare earth, or actinoid; T = transition metal; X = main-group element), AlB_2-related structures emerge when R atoms occupy the Al sites and T/X atoms form the hexagonal nets. In binary cases, only distortions of the T/X hexagons are observed, whereas substitution variants allow ordered or disordered hexagons with $T : X$ ratios of T_0X_6, T_1X_5, T_2X_4, T_3X_3, or T_4X_2, which may remain planar or become puckered.

The hexagonal and trigonal derivatives of AlB_2 share common structural motifs: (i) planar hexagonal nets and (ii) puckered or distorted hexagons arising from stacking variations. In all cases, the R layers are close-packed (three in-plane R–R neighbors), occasionally complemented by two additional ones along the hexagonal or pseudo-hexagonal axis, depending on the c/a ratio.

The simplest ternary ordering variant of the AlB_2 type is the SrPtSb structure [5], where planar hexagons alternate between Pt and Sb atoms, resulting in mutual trigonal-planar coordination. Planar hexagons are also realized in the Ni_2In-type structure [6], where Ni and In form ordered Ni_3In_3 hexagons while additional Ni occupies the Al sites, with alternating hexagon layers rotated by 60° leading to c-axis doubling. A related case is the ZrBeSi-type [7], featuring Be_3Si_3 hexagons separated by Zr atoms; it can be regarded as a ternary ordered derivative of the Ni_2In type, adopted by numerous silicides, germanides, and pnictides.

In $CaIn_2$ [8], the hexagonal layers are puckered, doubling the c-axis and yielding a lonsdaleite-like (hexagonal diamond) tetrahedral network. The orientation of these puckered hexagons depends on the valence electron concentration (VEC), i.e., the average number of valence electrons per atom, with VEC = 4 favoring diamond-like and VEC = 5 arsenic-like substructures. Ternary substitution variants and related ZrBeSi derivatives likewise show puckered, ordered layers, reducing the symmetry to non-centrosymmetric $P6_3mc$, often accompanied by twinning. Such hexagonal and trigonal AlB_2-derived motifs are of particular importance for the R–Pt–As system, which adopts several ordered variants of this family.

Whereas the hexagonal and trigonal derivatives form a continuous series of AlB_2-related structures without discontinuities, the orthorhombic branch represents a symmetry-reduced alternative with distinct structural features. A symmetry reduction to the orthorhombic system enables greater decoupling of atomic positions within the hexagons, leading to puckering and tilting that markedly alter the R atoms' coordination sphere. Instead of the 6+2 neighbors found in hexagonal superstructures, the number of nearest R neighbors is reduced to four. All orthorhombic and monoclinic variants derive from the orthohexagonal setting (space group $Cmmm$) of $P6/mmm$. While this setting does not permit complete ordering of atoms in a 1:1:1 composition, the orthorhombic symmetry allows structural expansion along one direction owing to the loss of threefold rotational symmetry.

Among the orthorhombic derivatives of AlB_2, the KHg_2 [9] ($CeCu_2$ [10]) and TiNiSi [11] structure types are of particular relevance, as they also occur in R–Au–Pb and R–Pt–Pb systems discussed below. In the KHg_2 structure, the Hg atoms form strongly puckered and tilted hexagons, giving rise to interlayer Hg–Hg bonds and nearly equal intra- and interlayer distances, while the K atoms are arranged in zig-zag chains between the puckered layers. The TiNiSi type, derived from KHg_2 by ordering on the Ni/Si sublattice, displays variable degrees of puckering: from weakly puckered, quasi-two-dimensional $[Zn_3Sn_3]$ layers in EuZnSn to the nearly tetrahedral, three-dimensional [NiSi] framework in TiNiSi. These structural features—tilted hexagons, interlayer bonding, and tunable dimensionality—form the basis for understanding the orthorhombic variants realized in the Au–Pb and Pt–Pb compounds.

1.1.1 R-Pt-As Pnictides

According to the literature [12], some alkaline-earth platinum pnictides $AE\mathrm{Pt}Pn (AE =$ Ca, Sr, Ba; $Pn =$ P, As, Sb) exhibit diverse hexagonal structure types that are structurally derived from the AlB_2 type and characterized by PtPn honeycomb networks [5, 13]. In these compounds, the AE occupies the Al site, while the Pt and Pn (pnicogen) are statistically distributed or ordered at the B sites of the honeycomb layers (Figure 1.1 (a)).

Among these compounds, BaPtAs crystallizes in the SrPtSb-type structure [5], which consists of alternating stacked Ba and ordered planar PtAs honeycomb layers stacked along the c-axis. The stacking sequence forms a -Pt(As)-Pt(As)- layered motif, as shown in the Figure 1.1 (b). Related $EuPt_xAs$ ($0.6 \leq x \leq 0.75$) also crystallize in this structure type [13].

In contrast, SrPtAs crystallizes in the KZnAs-type structure, another ordered variant of the AlB_2-type structure, in which PtAs honeycomb layers are stacked such that each As atom lies above a Pt atom and vice versa, leading to a -Pt(As)-As(Pt)- stacking configuration, as shown in Figure 1.1(c). The structure is globally centrosymmetric (space group $P6_3/mmc$), although the spatial inversion symmetry is locally broken in the PtAs honeycomb network.

This type of locally non-centrosymmetric stacking is also present in $RE\mathrm{PtAs} (RE =$ Y, Sm, Gd, Dy, Ho, Er, Tm, Yb, Lu), which also crystallize in the hexagonal space group ($P6_3/mmc$, D_{6h}^4, No.194) but with a different structure type compared to SrPtAs and BaPtSb [14], as shown in Figure 1.1(e). Notably, the YPtAs-type structures possess a significantly longer c - axis than KZnAs-type variants, reflecting the increased layer separation.

Multiple polymorphs have been reported for BaPtAs, depending on synthesis conditions. These include the SrPtSb-type ($P\overline{6}m2$, D^1_{3h}, No.187), YPtAs-type ($P6_3/mmc$, D^4_{6h} No.194) and LaIrSi-type ($P2_13$, T^4, No.198), the latter being a ternary ordered variant of the cubic $SrSi_2$-type structure($P4_132$, O^7, No.213) [5, 15].

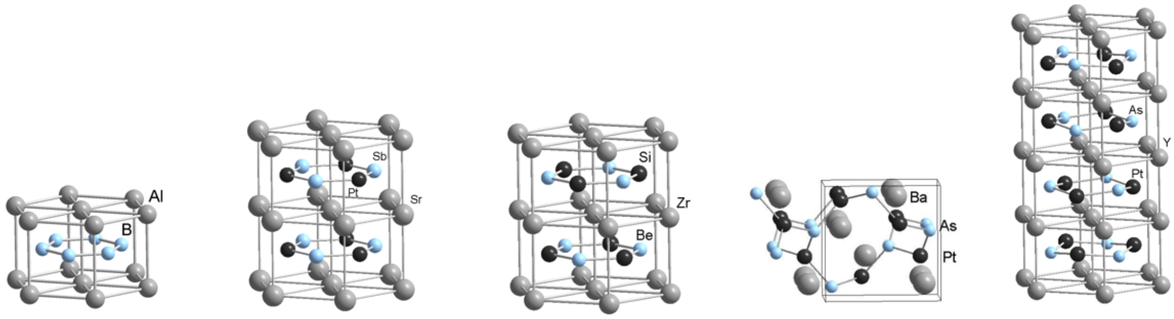

(a) AlB_2 type (b) SrPtPb type (c) ZrBeSi type (d) LaIrSi type (e) YPtAs type

Figure 1.1: Crystal structure of the (a) AlB_2-type $SrPt_xP_{2-x}$ ($P6/mmm$, D^1_{6h}, No.191), (b) SrPtSb-type BaPtAs ($P\overline{6}m2$, D^1_{3h}, No.187)(c) ZrBeSi-type SrPtAs ($P6_3/mmc$, D^4_{6h}, No.194) (d) LaIrSi-type BaPtAs ($P2_13$, T^4, No.198) (e) YPtAs-type BaPtAs ($P6_3/mmc$, D^4_{6h}, No.194)

CaPtAs and EuPtAs crystallize in a structure type related to the AlB_2-type structure (space group $I4_1md$, No. 109) [13], though the infinite honeycomb networks typical for this type are replaced by a rotated spatial arrangement. In these two structures, trigonal-planar are no longer arranged in two-dimensional infinite networks, but instead, rotated by 90° relative to each other according to $z/4$, creating a closed three-dimensional PtAs network, as shown in Figure 1.2 (a). In CaPtAs, interconnected hexagons still occur, whereas this is no longer the case with EuPtAs. The Eu atoms reside at 4a sites, centered in coordination polyhedra formed by trigonal Pt-As hexagons, whose axes are at right angles. In the [001] projection, the Ca sites in CaPtAs are coordinated similarly, situated within hexagonal prisms composed of Pt or As atoms, consistent with the AlB_2 geometry (Figure 1.2 (b)) [16].

The isotropic compounds $SrPt_4P_6$, $SrPt_4As_6$ and $BaPt_4As_6$ [17]crystallize in monoclinic derivatives of the pyrite-type structure ($C2/c$, Z=4), in which one alkaline-earth atom replaces a pnictogen dimer. These structures feature characteristic P–P or As–As dumbbells with bond lengths around 242-247 pm, closely matching the covalent radii sum (242 pm) and comparable to $PtAs_2$ [18].

1.1.2 R-Au-Pb compounds

The *RE*-Au-Pb system seems to have a similar trend as the *RE*-Pt-Pb system. A wide range of compounds RE_2Au_2Pb (RE = Y, La, Ce, Pr, Nd, Sm, Gd, Tb, Dy, Ho, Er,

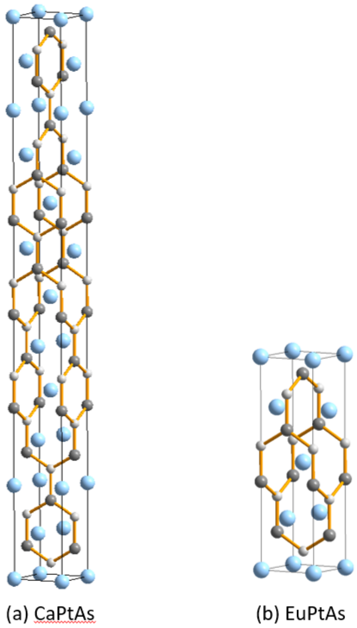
(a) CaPtAs (b) EuPtAs

Figure 1.2: Structure of CaPtAs and EuPtAs (space group $I4_1md$, No.109) Blue circle: Ca/Eu; Black circles: Pt; Grey circles: As.

Tm, Yb, and Lu) and Yb_2Pt_2Pb crystallize in the Er_2Au_2Sn structure type, space group $P4_2$/mnm (Pearson code tP20) [19–21]. In addition, multiple structure types have been identified for RAuPb compounds depending on the specific rare-earth element.

Light rare-earth REAuPb members (RE = La, Ce, Pr, Nd, Sm) crystallize in the $CaIn_2$ structure type (space group $P6_3/mmc$) [22], with RE atoms at the $2b$ Wyckoff sites and Au/Pb statistically occupying the $4f$ sites [23]. In contrast, heavy rare-earth REAuPb members (RE = Y, Gd, Tb, Dy, Ho, Er) crystallize in the cubic MgAgAs structure type (space group $F\bar{4}3m$) with 4Au in 0,0,0, 4R in $\frac{1}{4}$, $\frac{1}{4}$, $\frac{1}{4}$ and 4Pb in $\frac{3}{4}$, $\frac{3}{4}$, $\frac{3}{4}$ [23]. The lattice parameters of the RAuPb plumbides in the order of the periodic table and the structure type have been listed in Table 1.1. This transition in structure type reflects a lanthanide contraction trend and is accompanied by a marked decrease in unit cell volume.

The EuAuPb compound crystallizes in the orthorhombic KHg_2 type structure (space group $Imma$)[11, 24] which is isopointal with the commonly referenced $CeCu_2$-type [25, 26]. In this structure, the gold and lead atoms are randomly distributed on the mercury site, resulting in a high atomic displacement parameter U_{22} due to partial site disorder. The [AuPb] network is three-dimensional and leaves channels that are filled by the europium atoms.

A unit cell volume analysis across the RE-Au-Pb series reveals a sharp increase in atomic volume when transitioning from the $CaIn_2$-type to MgAgAs-type via the EuAuPb-type, consistent with structural behavior observed in RPdSb alloys [27], as shown in Figure 1.3. This evolution is attributed to increasing compression of R-(Au, Pb) and (Au, Pb)-(Au, Pb) bonds with decreasing rare-earth ionic radii. This may be the reason for the preferential stability of the MgAgAs-type structure under chemical pressure from rare-

Table 1.1: Crystallographic data for the RAuPb systems

compound	structure type	space group	Lattice parameters(pm)			reference(s)
			a	b	c	
LaAuPb	$CaIn_2$	$P6_3/mmc$	482	-	784.2	[23]
CeAuPb	$CaIn_2$	$P6_3/mmc$	480.2	-	773.9	[23]
PrAuPb	$CaIn_2$	$P6_3/mmc$	478.5	-	768.1	[23]
NdAuPb	$CaIn_2$	$P6_3/mmc$	476.4	-	762.8	[23]
SmAuPb	$CaIn_2$	$P6_3/mmc$	474.2	-	757.5	[23]
EuAuPb	KHg_2	$Imma$	487.0(1)	763.3(3)	841.2(3)	[24]
GdAuPb	MgAgAs	$F\bar{4}3m$	672.9	-	-	[23]
TbAuPb	MgAgAs	$F\bar{4}3m$	674.7	-	-	[23]
DyAuPb	MgAgAs	$F\bar{4}3m$	672.8	-	-	[23]
HoAuPb	MgAgAs	$F\bar{4}3m$	671.8	-	-	[23]
ErAuPb	MgAgAs	$F\bar{4}3m$	669.4	-	-	[23]

earth elements of smaller radii.

Yb_2Au_2Pb [21] and Yb_2Pt_2Pb [20] crystallize in an Zr_3Al_2-derived structure (Pearson code *tp*20, space group $P4_2/mnm$), comprising slabs of trigonal prisms and cubes formed by Yb atoms. Gold and lead atoms are centrally located in these polyhedra. A doubling of the c-axis is observed due to displacement-induced slab stacking, as shown in Figure 1.4.

Unlike the rare-earth members, Ca_2Au_2Pb, the only alkaline-earth member in this family, crystallizes in the Mo_2FeB_2 type (Pearson code *tP*10, space group $P4/mbm$), another ternary derivative of the U_3Si_2 structure, as shown in Figure 1.5 [28]. Here, Ca atoms form slabs of trigonal prisms and cubes, with Au and Pb occupying the centers [28].

Beyond rare-earths, alkali-metal–gold–lead systems such as K_3Au_5Pb [29] crystallize in a substitution variant of the $MgCu_2$-type, comprising corrugated $^2_\infty[\mathrm{Au(1)Au(2)_{2/2}Au(3)_{1/2}}]$ tetrahedral layers that are crosslinked by zigzag $^2_\infty[\mathrm{Pb_{2/2}}]$ chains via Au(1)–Pb contacts, yielding an overall three-dimensional framework. The M_3AuSn_4 family (M = K, Rb, Cs) crystallizes in monoclinic layered structures that can be interpreted using the Zintl–Klemm concept. In these compounds, the Sn atoms form a covalently bonded polyanionic framework of interconnected Sn tetrahedra, while Au atoms are incorporated into the framework and alkali-metal cations are located between the layers, maintaining charge balance. The related M_3AuPb_4 phases are isostructural but deviate from ideal Zintl behavior: although Pb atoms form a comparable framework, weaker Pb–Pb interactions and more delocalized electronic states diminish the Zintl character. These structural frameworks highlight the

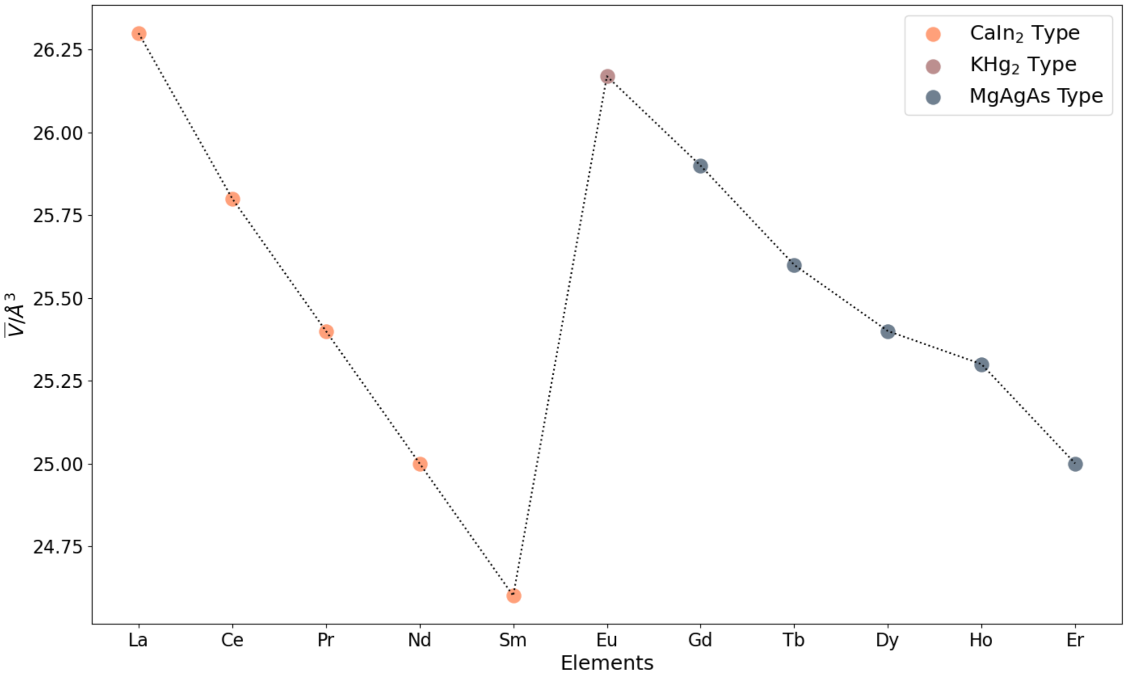

Figure 1.3: Average atomic volume of *RE*-Au-Pb alloys

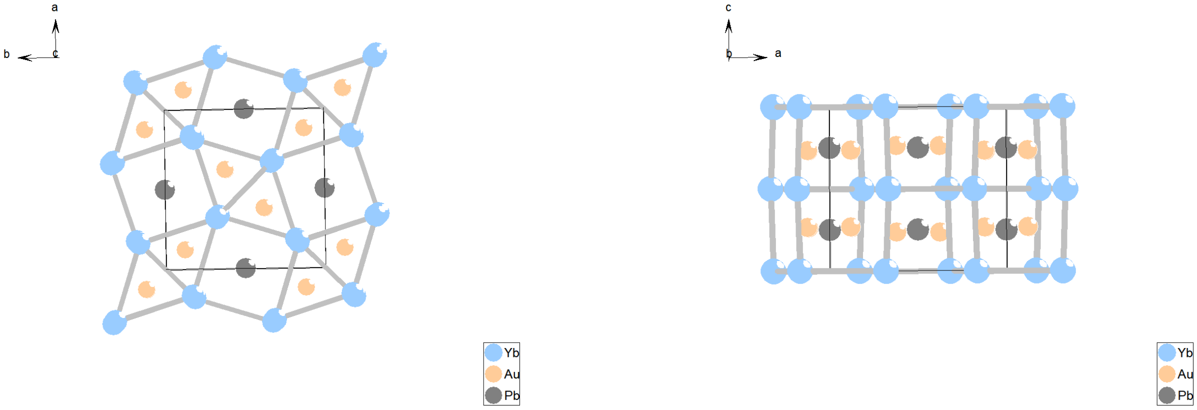

Figure 1.4: Projection of the crystal structure of Yb_2Au_2Pb along the c and b axes. The CsCl and AlB_2 like slabs are emphasized.

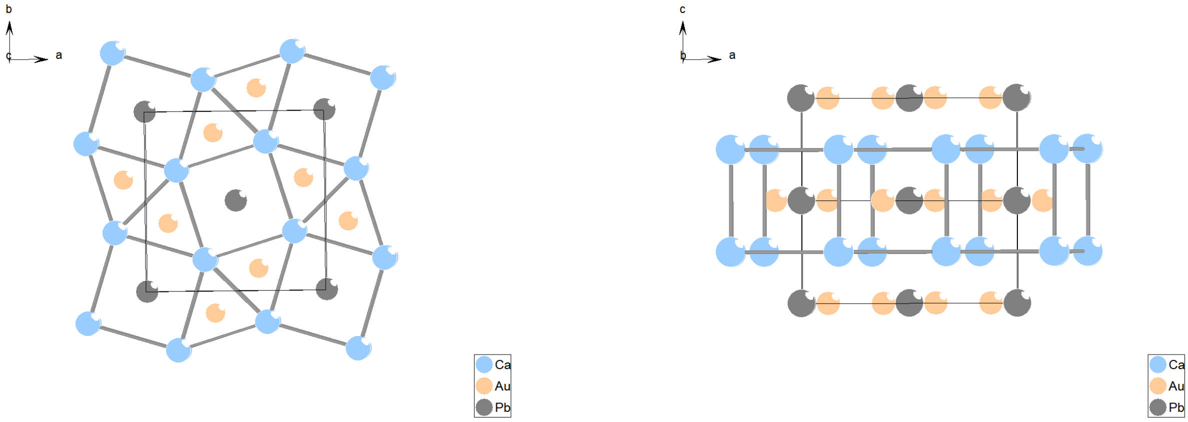

Figure 1.5: Projection of the crystal structure of Ca_2Au_2Pb along the c and b axis.

contrasting bonding regimes between the stannides and plumbides, reflecting the balance between covalency and metallicity in Au–Sn/Pb networks [30].

1.1.3 R-Pt-Pb compounds

The *R*-Pt-Pb compounds also show structural diversity across different rare-earth and alkaline-earth compositions. In the CaPtX (X = Si, Ge, Sn, Pb) series, the choice of the p-block element X strongly influences the crystal structure formed under ambient conditions. CaPtPb crystallizes in the three-dimensional four-connected (3D4C) net of the TiNiSi-type structure even at normal pressure, as shown in Figure 1.6(a). Substitution of Si by more metallic elements such as Ge, Sn, or Pb stabilizes the TiNiSi-type 3D4C structure at ambient pressure [31]. Trimorphic CaPtSi has been shown to crystallize in three different structures under varying synthesis pressure: (I) Cubic phase (LaIrSi-type structure), Pt and Si form a three-dimensional three-connected (3D3C) net;(II) Monoclinic phase (EuNiGe-type structure), platinum and silicon form an ordered two-dimensional three-connected (2D3C) net [32]; (III) orthorhombic phase (TiNiSi-type structure), platinum and silicon are arranged in an ordered three-dimensional four-connected (3D4C) net [11].

In contrast to these AlB_2-derived structures, the substitutional solid solution series $Ce_{1-x}Pb_xPt_2$ ($0 \leq x \leq 0.5$) crystallizes in the cubic $MgSnCu_4$-type structure, adopting the space group $F\bar{4}3m$ (No.216) [33] (Figure 1.6(b)). This demonstrates that within the *R*–Pt–Pb system, not only can AlB_2 derivatives be stabilized, depending on the choice of rare-earth and p-block elements.

Moreover, GdPtPb adopts the hexagonal ZrNiAl-type structure (space group $P\bar{6}2m$, No.189), in which the Gd atoms form a distorted Kagomé sublattice that underlies its noncollinear antiferromagnetic ordering at 15.5 K [34], as shown in Figure 1.6(c). RE_2Pt_2Pb (RE = Y, La, Ce, Pr, Nd, Sm, Gd, Tb, Dy, Ho, Er, Tm, and Lu) crystallizes in the Mo_2FeB_2-type [19] (space group $P4/mbm$, No.127), known as the ordered U_2Si_2-type. Ce_2M_2Pb (M = Au, Pt) are isostructural [35](Figure 1.6(d)). Yb_2Pt_2Pb crystallizes with the Er_2Au_2Sn [36] type structure, a ternary ordered version of the Zr_3Al_2-type [20], composed of CsCl- and AlB_2-related slabs (YbPb and $YbPt_2$) [20], with Pt–Pt distances slightly longer than in *fcc* platinum [37] (Figure 1.6(e)).The compounds LaPtPb and CePtPb grow in the hexagonal Fe_2P structure, as reported in Ref. [38].

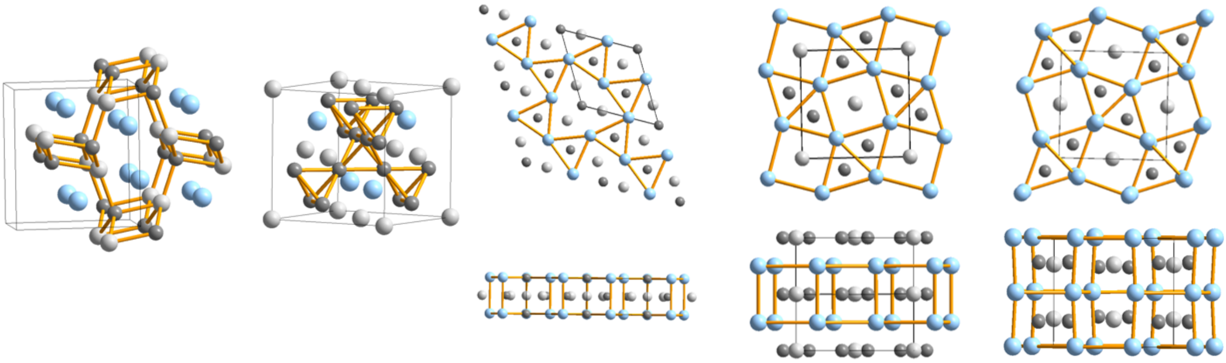

(a) CaPtPb (b) $Ce_{1-x}Pt_2Pb_x$ (c) GdPtPb (d) Ce_2Pt_2Pb (e) Yb_2Pt_2Pb

Figure 1.6: Crystal structure of the (a) TiNiSi-type CaPtPb ($Pnma$, No.62), (b) $MgSnCu_4$-type $Ce_{1-x}Pb_xPt_2$($F\bar{4}3m$,No.216), (c) ZrNiAl-type GdPtPb ($P\bar{6}2m$, No.189), (d) Mo_2FeB_2-type Ce_2Pt_2Pb ($P4/mbm$, No.127), (e) Er_2Au_2Sn-type Yb_2Pt_2Pb ($P4_2/mnm$, No.136)

Additional intermetallics in the *R*-Pt-Pb family include $Eu_2Pt_3Pb_5$ and $SrPt_2Pb_4$, recently reported as the first ternary phases in their respective systems [39], as shown in Figure 1.7. These two are the first ternary compounds in these systems and crystallize in closely related $Y_2Rh_3Sn_5$ [40] and $NdPh_2Sn_4$ [41] structure types, respectively. Both feature extended Pt_xPb_y polyanion networks with cations embedded in their channels. These structures are associated with typical intermetallic appearance—silvery luster, brittle nature, and moderate moisture sensitivity.

Notably, the stability of EuTX (T = Pt, X = Pb) compounds is highly dependent on surface area and crystal form. While well-formed single crystals are relatively air-stable, ground powders rapidly degrade in moist environments, necessitating storage under inert conditions [24].

So far, more than 180 rare earth-transition metal-plumbides have been reported. They crystallize with 23 different structure types. Apart from the few Pb-rich plumbides with $Yb_3Rh_4Sn_{13}$ and related structures, only plumbides with 33 at% or even lower lead content have been reported. Some ternary systems exhibit large liquid ranges in the lead-rich regions at 870°C. Through phase analytical investigations at lower temperatures, one will possibly get access to new lead-rich phases. Only YbAgPb and $La_4Rh_3Pb_4$ show peculiar structure types, which have first been observed for a plumbide. All other plumbides exhibit relatively simple structure types, which have been observed for silicates, germanides, stannides, gallides, or indides. One may expect that the lead characteristic structure will form in the lead-rich parts of the ternary systems, similar to the gallium and indium-based

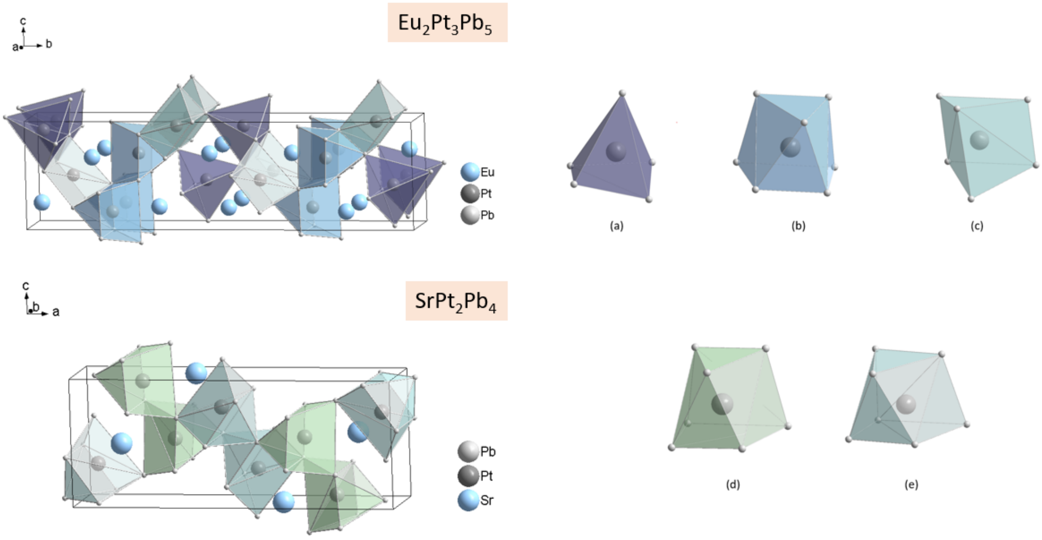

Figure 1.7: Unit cell of $Eu_2Pt_3Pb_5$ and types of Pt atom coordination:(a) distorted tetragonal pyramid $PtPb_5$;(b) edge-sharing heptahedra $PtPb_7$; (c) distorted trigonal prisms $PtPb_6$.Unit cell of $SrPt_2Pb_4$ and its types of Pt atom coordination: (d) edge-sharing heptahedra $PtPb_7$; (e) vertices-sharing heptahedra $PtPb_7$

phase diagrams. A few R-T-Pb and R_2T_2Pb plumbides that have been characterized for their magnetic behavior show very interesting properties. Also in this field, the plumbides exhibit a large potential for new phenomena and can thus be considered a vivid area for the future.

1.2 Physical properties

Equiatomic layered intermetallics of the general formula $RE - T - X$ (RE = rare-earth metal, T = transition metal, X = p-block element) exhibit a broad range of physical properties. Their behavior is primarily determined by the nature of the rare-earth element, the transition metal, and the structure type. In many of these compounds, localized 4f electrons lead to magnetic phenomena. For instance, LaPtPb and CePtPb crystallize in the hexagonal ZrNiAl-type structure, while LaPtPb shows a non-magnetic ground state and CePtPb is paramagnetic [38]. EuAuPb has a magnetic moment of 6.8 μ_B/Eu atom in the paramagnetic range and shows antiferromagnetic ordering at 7K [24, 42]. The stable antiferromagnetic ground state was also evident from the negative Weiss constant of -14K and the monotonically increasing magnetization curve. Many EuTX compounds (T = transition metal, X = p-element) appear as silvery single crystals with a metallic luster and brittle nature. Their air stability varies widely: plumbides are moisture sensitive and quickly deteriorate, while pnictides are more stable. Generally, single crystals are more stable than powders due to lower surface area exposure [24].

Superconductivity is a quantum phenomenon in which a material exhibits zero electrical resistance below a critical temperature (T_c) [43]. In conventional superconductors, electron pairing (Cooper pairs) is mediated by phonons, and symmetry plays a key role. High-symmetry crystal frameworks are often favorable for conventional superconductivity, while lower-symmetry, layered structures can host unconventional pairing mechanisms. In layered transition-metal pnictides, iron-based superconductors like REFeAsO (RE = rare earth elements), AEFe$_2$As$_2$ (AE = alkali earth elements), and AFeAs (A = alkali elements) are prominent examples [44, 45]. High crystal symmetries favor conventional superconductivity [46] while structure motifs such as Fe-As tetrahedra or CuO$_4$ squares are important for high temperature superconductors [47–49]. The most common method to induce superconductivity is the application of pressure, which compresses crystal structures, changing the interactions of atoms' atomic orbitals and, consequently, their hybridization, and, consequently, the electronic bandwidth, the Fermi surface, and the electron-phonon coupling. Such structural instabilities under pressure can strongly influence superconductivity; for instance, in CaFe$_2$As$_2$, a collapse of the tetragonal c-axis under pressure has been associated with the destruction of superconductivity [50, 51].

Several layered platinum arsenides, such as SrPtSb-type and YPtAs-type structures of BaPtAs, both exhibit superconductivity, while the cubic LaIrSi-type does not. Among them, the hexagonal compounds with ordered honeycomb networks SrPtAs and BaPtSb exhibit superconductivity at 2.4 and 1.64 K [12, 52], respectively. The local noncentrosymmetric structure of the ordered PtAs honeycomb network, strong spin-orbit coupling of Pt, and weak coupling between the PtAs layers make SrPtAs a unique medium to study theoretically predicted exotic superconductivity [53–61], such as the singlet-triplet mixed state [54], chiral d-wave state [55], and f-wave state [56].

Topological aspects of superconductivity have also attracted considerable interest. A topological superconductor (SC) is characterized by a superconducting gap in the bulk and protected Majorana fermions on the boundaries or in vortex cores under an externally applied magnetic field [62, 63]. While signatures of topological superconductivity have been observed in one-dimensional chains with proximity-induced superconductivity [64, 65], the realization of intrinsic topological superconductivity in two dimensions remains an exciting and relatively unexplored field [66–68].

Despite structural similarities to known superconductors, compounds like LaPtPb, CePtPb [38], and Sr$_2$Pt$_{8-x}$As [69] do not exhibit superconductivity at low temperatures, likely due to factors such as magnetic pair-breaking from 4f moments [38], unfavorable electronic filling [69], structural complexity including vacancy modulation [70], and pressure-sensitive phase stability—underscoring [70] that a layered structure alone is insufficient, and superconductivity emerges only when structural, electronic, and magnetic conditions are optimally balanced.

Beyond superconductivity, the studied compounds show a range of interesting physical behaviors. Most RTX-type compounds exhibit metallic conductivity, and in some cases, relatively low electrical resistivity anisotropy, despite their layered nature. Sr$_2$Pt$_{8-x}$As are notably influenced by its incommensurately modulated structure and ordered platinum vacancies. These features contribute to anisotropic yet interconnected electronic conduction paths. Interestingly, its transport behavior follows the Mooij correlation [71], an empirical relation stating that in highly disordered metals, once the resistivity is above a threshold value 150-200 $\mu\Omega\,\mathrm{cm}$, the temperature coefficient $d\rho/dT$ changes sign from metallic to non-metallic. This observation extends the relevance of the Mooij correlation to materials with modulated vacancy order [69].

$BaPt_2As_3$, adopting a $P2_1/c$ monoclinic structure, features alternating Ba_2Pt and Pt_3P_6 layers. The layer separation and Pt coordination environments provide possible low-dimensional conduction pathways and make it a candidate for anisotropic transport behavior. The structural complexity of these compounds, coupled with observed ordering phenomena, warrants further investigation of their resistivity, carrier mobility, and potential for unconventional transport behavior [18]. Similarly, the presence of P–P and As–As dumbbells in $SrPt_4Pn_6$ and $BaPt_4As_6$ suggests localized bonding and electron pair formation, which may significantly influence their electronic transport properties. Such bonding motifs, typical of pyrite-type derivatives, often correlate with semiconducting or semimetallic behavior [17].

Overall, the layered intermetallics studied here exhibit a broad range of physical properties, from magnetic ordering and metallicity to vacancy-induced anisotropy, reinforcing their potential as candidates for future investigations of unconventional electronic states.

1.3 Supertetrahedral Networks in Group I Phosphidosilicates

All-solid-state batteries (ASSBs) that employ solid instead of liquid electrolytes are widely regarded as next-generation energy storage devices due to their potential for higher energy densities and faster charging rates compared to conventional systems [72–77]. In these batteries, the solid electrolyte plays a critical role, and its ionic conductivity is a key performance metric. ASSBs typically consist of three major components: cathode, anode, and an ion-conducting electrolyte. Cathode materials must be redox-active to facilitate electron and ion transport during charging and discharging, often incorporating transition metals with multiple oxidation states. Anodes, in contrast, are typically composed of intercalated or pure metals with low electrochemical potentials. In both electrodes, additional requirements such as ion accessibility and structural stability are crucial [78–82].

For the electrolyte, the most important property is its ability to conduct only ions—preventing short circuits or self-discharge. Traditional electrolytes are often based on alkali salts dissolved in aprotic solvents or polymers [83, 84], whereas solid electrolytes offer improved energy density, thermal stability, and the potential for using lithium metal anodes [73, 77, 85–87] Therefore, solid-state electrolytes require rigid anionic frameworks with loosely bound cations to facilitate fast ion transport. Structural modifications, including softening the anionic framework to reduce Coulombic interactions, have been found to enhance ionic conductivity in chalcogenotetrelates and pentelides [88–101].

Phosphidosilicates, which feature SiP_4 tetrahedra connected via shared vertices or edges, form structural motifs ranging from isolated units to chains, layers, or complex three-dimensional networks. Some examples are isolated $[Si_2P_6]^{10-}$ anions in Na_5SiP_3 [102], infinite $^1_\infty[SiP_{4/2}]^{2-}$ chains in K_2SiP_2 [103], double layers of SiP_4 tetrahedron in KSi_2P_3 [104], and interpenetrating three dimensional $[SiP_{4/2}]^{2-}$ networks in $MgSiP_2$ [105].Furthermore, several compounds such as $AlSiP_3$ [106] or $Ca_3Si_8P_{14}$ [107] are polyphosphides with short P-P bonds between neighboring tetrahedra, which distinguishes Phosphidosilicates from structurally comparable oxido- and nitridosilicates where homonuclear bonds between oxygen and nitrogen atoms do not form. Phosphidosilicates with transition- [108–111] and rare-earth metals [112] are also known.

Several lithium-ion-conducting materials have already demonstrated high conductivity. Garnet-type oxides like doped $Li_7La_3Zr_2O_{12}$ and $Li_{1.4}Al_{0.4}Ti_{0.6}(PO_4)_3$ achieve conductivities of up to 10^{-3} $S\,cm^{-1}$ at room temperature. Even higher conductivities $1.6{\cdot}10^{-4}$ to $2.5{\cdot}10^{-2}$ $S\,cm^{-1}$ have been observed in nanostructured thiophosphates [113], halide argyrodites [88, 114], $Li_{10}GeP_2S_{12}$-type materials [89], and rare-earth halides [115–117]. In 2016, the discovery of orthosilicate Li_8SiP_4 a conductivity of $1.2{\cdot}10^{-4}$ $S\,cm^{-1}$ and an activation energy of 0.37 eV [118] revitalized interest in phosphidosilicates as promising solid electrolytes. $Li_{10}Si_2P_6$, $Li_3Si_3P_7$ and $Li_{14}SiP_6$ with conductivities reaching 10^{-3} $S\,cm^{-1}$ [2, 3].

However, lithium-based systems face limitations in scalability and cost, prompting interest in sodium and potassium analogues that use more earth-abundant elements [78, 119–122]. Supertetrahedral phosphidosilicates, composed of SiP_4 tetrahedra assembled into larger Tn units (n = 2–6), offer diverse structural motifs with potential for ionic conduction. A supertetrahedron or supertetrahedral cluster is a segment of the sphalerite-type structure. The number of constituting tetrahedra in a Tn supertetrahedron is $tn = n(n+1)(n+2)/6$ where n is the number of tetrahedra along the cluster edges [123]. These supertetrahedra can appear isolated, vertex-sharing, or fused via common base units [124–128] forming intricate 3D networks or layered frameworks, often resembling hierarchical variants of HgI_2-type structures [129], as shown in Figure 1.8 and Figure 1.9.

Li_2SiP_2 contains solely T2 supertetrahedra (4 SiP_4, heteroadamantane), forming interpenetrating diamond-like networks, while $LiSi_2P_3$ is composed of T4 (20 SiP_4) and T5 (35 SiP_4) supertetrahedra sharing a common SiP_4 tetrahedron [127, 130]. These structures promote Li^+-ion mobility. Supertetrahedral growth has also been studied in Na-based systems. The relation between the phases T3T3 and T5T5 can be rationalized by adding 3×"Si_3P_4" to the formula: $Na_{23}Si_{19}P_{33}$ (T3T3)+3×"Si_3P_4" → $Na_{23}Si_{28}P_{45}$ (T3T4)+3×"Si_3P_4" → $Na_{23}Si_{37}P_{57}$ (T4T4)+3×"Si_3P_4" → $Na_{23}Si_{37}P_{57}$ (T4T5 or T5T5). The formula is $Na_{23}Si_{9n+19}P_{12n+33}$ (n = 0-3) [128]. Adding charge-neutral "Si_3P_4" to the anionic framework reduces the charge density, thus reducing the effective charge acting on the Na^+-ions.

$Na_{19}Si_{13}P_{25}$ have two different motives: one with two edge-sharing tetrahedral bridged by a vertex-sharing SiP_4 unit and and one with an additional P–P bond. $Na_{23}Si_{19}P_{33}$ features vertex-linked T3 tetrahedron in a $Li_9B_{19}S_{33}$ - type structure[131]. $Na_{23}Si_{37}P_{57}$ contains only T4 units [128], while $Na_{23}Si_{28}P_{45}$ contains T3 and T4 tetrahedra, whereby every T3 shares vertices to two other T3, one T4 and is fused with another T4 tetrahedra [128]. In contrast to the complex patterns of $Na_{23}Si_{28}P_{45}$ the crystal structure of LT-

$NaSi_2P_3$ and HT-$NaSi_2P_3$ are relatively simple. LT-$NaSi_2P_3$ contains T4 and T5 units connected tetrahedrally, HT-$NaSi_2P_3$ contains only T5 entiles. These T5 supertetrahedra lack one Si atom in their centers, a feature also seen in compounds like $[In_{34}S_{54}]^{6-}$[132], $LiSi_2P_3$[127] and HP-B_2S_3[133], which may help maintain charge neutrality.

Na^+ vacancies appear in most of these compounds (except $Na_{19}Si_{13}P_{25}$ and $Na_{23}Si_{19}P_{33}$), attributed to the increasing voids between the supertetrahedra anionic networks. These findings are typical for compounds that exhibit a high mobility of Na^+-ions [134]. The replacement of a T3 supertetrahedron by a Si_3P_8 unit in $Na_{19}Si_{13}P_{25}$ creates additional space for the migration of Na^+-ions.

Potassium phosphidosilicates show similar potential, currently only the compounds K_2SiP_2 [103], the layered T3 KSi_2P_3 [104] and T5 supertetrahedra structured KSi_2P_3-$tI960$ [135]. KSi_2P_3 contains T3 entities fused via common SiP_4 tetrahedra [104], forming layers with the K^+ ions residing between them [123]. A high-temperature tetragonal phase, KSi_2P_3-$tI960$ [135], resembles the diamond-type network of HT-$NaSi_2P_3$[128]. Every T5 cluster features a missing silicon site in its center, affecting the adjacent four phosphorus atoms by shifting them slightly towards the vacancy. KSi_2P_3-$tI960$ undergoes *translationsgleiche*(t2) symmetry reductions from space group $I4_1/acd$ to monoclinic subgroups of KSi_2P_3-$oF1952$ (space group $Fddd$) and KSi_2P_3-$mC928$ (space group $C2/c$) [135].

Recent studies indicate that the ionic conductivity in supertetrahedral phosphidosilicates increases with cluster size [128]. These insights support the continued exploration of alkali–Si–P supertetrahedral frameworks as promising candidates for next-generation solid-state electrolytes.

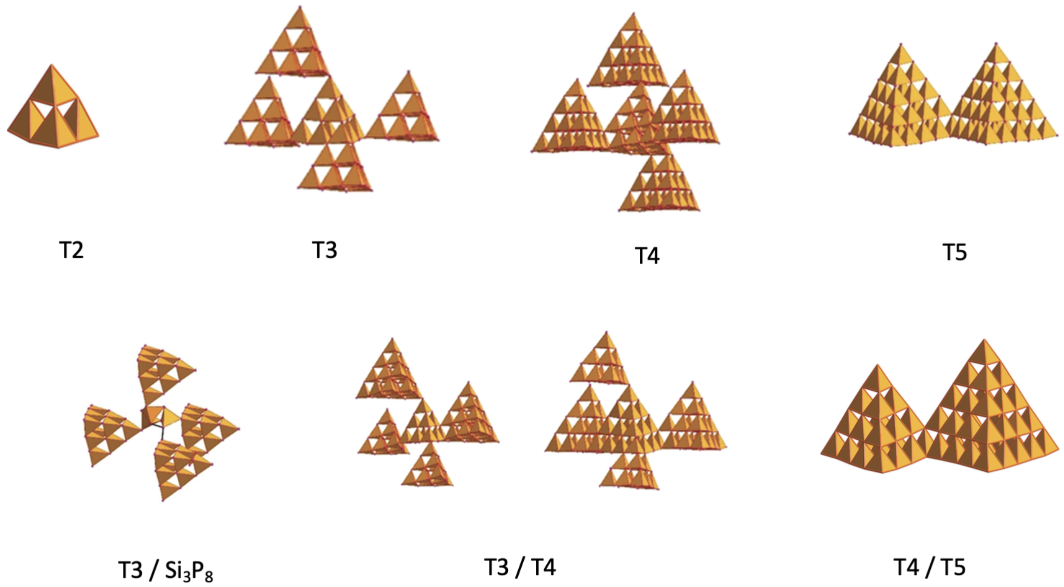

Figure 1.8: Supertetrahedral building units of Li_2SiP_2(T2), $LiSi_2P_3$(T3), $Na_{23}Si_{37}P_{57}$ (T4), HT-$NaSi_2P_3$(T5), $Na_{19}Si_{13}P_{25}$ (T3/Si_3P_8), $Na_{23}Si_{28}P_{45}$(T3/T4), $LiSi_2P_3$(T4/T5)

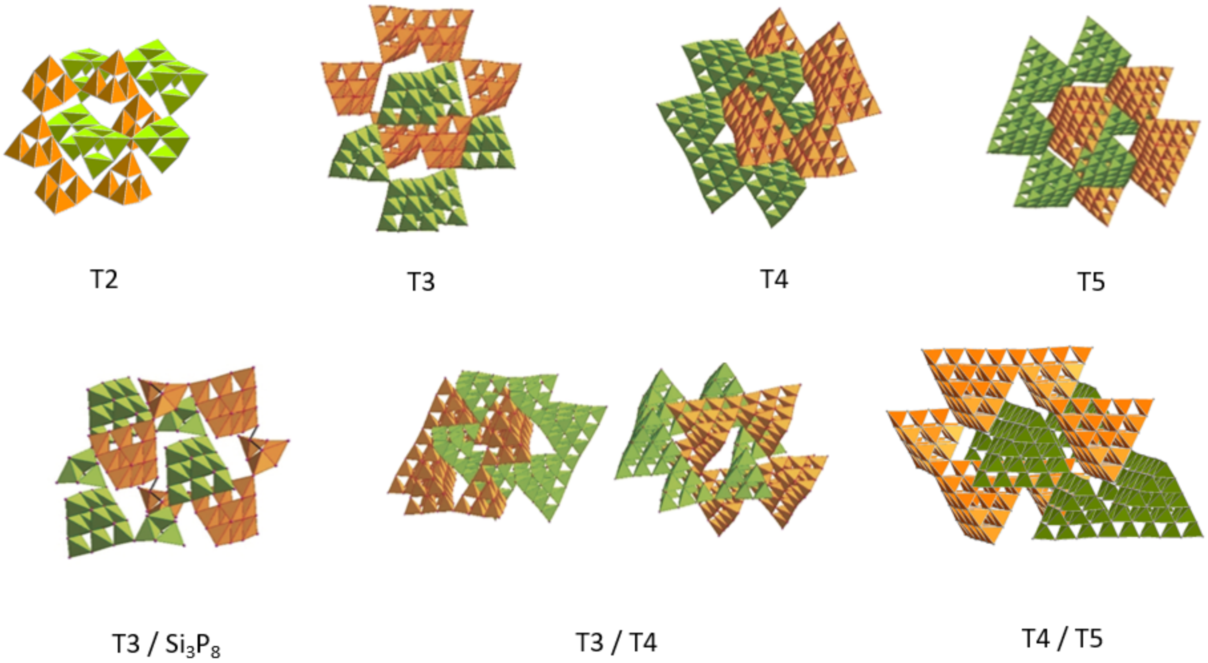

Figure 1.9: Crystal structure of Li_2SiP_2(T2)[127] , $LiSi_2P_3$(T3), $Na_{23}Si_{37}P_{57}$ (T4), HT-$NaSi_2P_3$(T5), $Na_{19}Si_{13}P_{25}$ (T3/Si_3P_8), $Na_{23}Si_{28}P_{45}$(T3/T4)[128], $LiSi_2P_3$(T4/T5) [127]

1.4 Topics and structure of the thesis

This thesis investigates the research and characterization of previously unknown platinum-arsenides and plumbides pnictides with alkaline-earth metals and rare-earth metals, aiming to discover new structural motifs or enhanced properties that may contribute a minor aspect to addressing current or future challenges.

In the following chapters, we will first discuss the crystal structure of the NdPtAs and compare the physical properties with related Pt-As system compounds. The latter have been investigated concerning their magnetic and electrical properties since they have comparably simple crystal structures. This facilitates the calculation of the electronic structure and various properties. In the following Chapter 3, we focus on the Au plumbides sample AEAuPb (AE= Ca, Sr, Ba), which has a similar honeycomb lattice as the EuAuPb. Chapter 4 deals with the discovery of the related plumbides SrPtPb and EuPtPb. Chapter 5 hints at the discovery and ionic conduction investigation with the heavy alkaline metal ions of Rubidium in the supertetrahedra phosphidosilicates. We also extend the substituting elements in the phosphidosilicates to quaternary systems with the purpose of possibly ionic conduction by further Si diluting with the incorporation of Al^{3+} cations in $RbSi_2P_3$.

References

[1] S. Gupta and K. G. Suresh. Review on magnetic and related properties of RTX compounds. *J. Alloys Compd.*, 618:562–606, 2015.

[2] H. Eickhoff, L. Toffoletti, W. Klein, G. Raudaschl-Sieber, and T. F. Fässler. Synthesis and characterization of the lithium-rich phosphidosilicates $Li_{10}Si_2P_6$ and $Li_3Si_3P_7$. *Inorg. Chem.*, 56(11):6688–6694, 2017.

[3] S. Strangmüller, H. Eickhoff, D. Müller, W. Klein, G. Raudaschl-Sieber, H. Kirchhain, C. Sedlmeier, V. Baran, A. Senyshyn, V. L. Deringer, et al. Fast ionic conductivity in the most lithium-rich phosphidosilicate $Li_{14}SiP_6$. *JACS*, 141(36):14200–14209, 2019.

[4] W. Hofmann and W. Jäniche. Die struktur von aluminiumborid AlB_2. *Z. Phys. Chem.*, 31(1):214–222, 1936.

[5] G. Wenski and A. Mewis. Trigonal-planar koordiniertes platin: Darstellung und struktur von $SrPtAs(Sb), BaPtP(As, Sb)$, $SrPt_xP_{2-x}$, $SrPt_xAs_{0,90}$ und $BaPt_xAs_{0,90}$. *Z. Anorg. Allg. Chem.*, 535(4):110–122, 1986.

[6] F. Laves and H. J. Wallbaum. Über einige neue vertreter des NiAs-typs und ihre kristallchemische bedeutung. *Z. angew. Mineral*, 4:17–46, 1942.

[7] J. W. Nielsen and N. C. Baenziger. The crystal structures of ZrBeSi and $ZrBe_2$. *Acta Crystallogr.*, 7(1):132–133, 1954.

[8] A. Iandelli. MX_2-verbindungen der erdalkali-und seltenen erdmetalle mit gallium, indium und thallium. *Z. Anorg. Allg. Chem.*, 330(3-4):221–232, 1964.

[9] E. J. Duwell and N. C. Baenziger. The crystal structures of KHg and KHg_2. *Acta Crystallogr.*, 8(11):705–710, 1955.

[10] A. C. Larson and D. T. Cromer. The crystal structure of $CeCu_2$. *Acta Crystallogr.*, 14(1):73–74, 1961.

[11] C. B. Shoemaker and David P. Shoemaker. A ternary alloy with $PbCl_2 - typestructure : TiNiSi(E)$. *Acta Crystallogr.*, 18(5):900–905, 1965.

[12] K. Kudo, Y. Saito, T. Takeuchi, S. Ayukawa, T. Kawamata, S. Nakamura, Y. Koike, and M. Nohara. Superconductivity in BaPtSb with an ordered honeycomb network. *J. Phys. Soc. Jpn.*, 87(6):063702, 2018.

[13] G. Wenski and A. Mewis. Ternäre varianten des AlB_2-typs. darstellung und struktur von Ca(Eu)PtX ($X = P, As, Sb$), $CaPt_xP_{2-x}$, $EuPt_xP(As)_{2-x}$ und $CaPt_xAs_{0,9}$. *Z. Anorg. Allg. Chem.*, 543(12):49–62, 1986.

[14] G. Wenski and A. Mewis. REPtX compounds with structures related to AIB_2- and $MgAgAs-type$ (RE = Y, rare earth element; X = P, As, Sb). *Z. Kristallogr. Cryst. Mater.*, 176(1-2):125–134, 1986.

[15] K. Kudo, T. Takeuchi, H. Ota, Y. Saito, S. Y. Ayukawa, K. Fujimura, and M. Nohara. Superconductivity in hexagonal BaPtAs: SrPtSb- and YPtAs-type structures with ordered honeycomb network. *J. Phys. Soc. Jpn.*, 87(7):073708, 2018.

[16] R. D. Hoffmann and R. Pöttgen. AlB_2-related intermetallic compounds–a comprehensive view based on group-subgroup relations. *Kristallogr. – Cryst. Mater.*, 216(3):127–145, 2001.

[17] G. Wenski and A. Mewis. Ternäre varianten des pyrit-typs: Darstellung und struktur von $SrPt_4P_6$, $SrPt_4As_6$, $BaPt_4As_6$ und $BaPt_2P_3$/ternary pyrite-type derivatives: Preparation and crystal structure of $SrPt_4P_6$, $SrPt_4As_6$, $BaPt_4As_6$ and $BaPt_2P_3$. *Z. Naturforsch. B*, 42(4):507–513, 1987.

[18] S. Furuseth, K. Selte, A. Kjekshus, P. H. Nielsen, B. Sjöberg, and E. Larsen. Redetermined crystal structures of $PdAs_2$, $PdSb_2$, $PtP_2, PtAs_2$, $PtSb_2$, $a-PtBi_2$, and $AuSb_2$. *Acta Chem. Scand.*, 19:735–741, 1965.

[19] G. Melnyk, L. D. Gulay, and W. Tremel. Crystal structures of new ternary compounds in $RE-Pt-Pb$ and $RE-Au-Pb$ systems (RE= rare earth metal). *J. Alloys Compd.*, 528:70–73, 2012.

[20] R. Pöttgen, P. E. Arpe, C. Felser, D. Kußmann, R. Müllmann, B. D. Mosel, B. Künnen, and G. Kotzyba. Structure and properties of YbZnSn, YbAgSn, and Yb_2Pt_2Pb. *J. Solid State Chem.*, 145(2):668–677, 1999.

[21] M. L. Fornasini, F. Merlo, and M. Pani. Crystal structure of ytterbium gold plumbide (2/2/1), Yb_2Au_2Pb. *Z. Kristallogr., New Cryst. Struct.*, 216(1-4):24–24, 2001.

[22] A. Iandelli. On compounds of the mx formula formed from rare earth elements and P, As, Sb, Bi, S, Se, Te, compounds with thulium and lutetium. *Atti Accad. Naz. Lincei, Rend., Cl. Sci. Fis. Mat. Nat., Ser. 8*, 37:160–160, 1964.

[23] R. Marazza, D. Rossi, and R. Ferro. On the ternary rare earth alloys: RAuPb compounds. *J. Less-Common Met.*, 138(2):189–193, 1988.

[24] P. E. Arpe. Synthese und strukturchemische untersuchungen an ternären plumbiden des ytterbiums. *Universität Münster: Staatsexamensarbeit*, 1998.

[25] L. M. Gelato and E. Parthé. Structure tidy–a computer program to standardize crystal structure data. *J. Appl. Crystallogr.*, 20(2):139–143, 1987.

[26] E. Parthé and L. M. Gelato. The standardization of inorganic crystal-structure data. *Acta Crystallogr., A, Found. Crystallogr.*, 40(3):169–183, 1984.

[27] R. Marazza, D. Rossi, and R. Ferro. $CaIn_2$-type and MgAgAs-type RESbPd compounds (RE = rare earth element). *J. Less-Common Met.*, 75(2):P25–P28, 1980.

[28] M. L. Fornasini, F. Merlo, and M. Pani. Crystal structure of calcium gold plumbide (2/2/1), Ca_2Au_2Pb. *Z. Kristallogr., New Cryst. Struct.*, 216(1-4):23–23, 2001.

[29] U. Zachwieja and J. Wlodarski. K_3Au_5Pb: eine schichtstruktur mit $[AuAu_{3/2}]$-goldtetraedern und $[Pb_{2/2}]$-blei-ketten. *Z. Anorg. Allg. Chem.*, 624(10):1569–1572, 1998.

[30] U. Zachwieja, J. Müller, and J. Wlodarski. Zintl-verbindungen mit gold: M_3AuSn_4 mit M= K, Rb, Cs und M_3AuPb_4 mit M= Rb, Cs. *Z. Anorg. Allg. Chem.*, 624(5):853–858, 1998.

[31] J. Evers, G. Oehlinger, K. Polborn, and B. Sendlinger. From a three-to a four-connected net in trimorphic CaPtSi at high pressure. *J. Solid State Chem.*, 103(1):45–56, 1993.

[32] B. D. Oniskovets, V. K. Bel'skii, V. K. Pecharskii, and O. I. Bodak. Crystalline structure of EuNiGe. *Z. Kristallogr.*, 32(4):888–890, 1987.

[33] K. T. Matsumoto, Y. Saiga, Y. F. Inoue, and T. Takabatake. Formation of a superlattice structure and suppression of the magnetic order in $Ce_{1-x}Pb_xPt_2$ ($0 \leq x < 0.5$). *J. Alloys Compd.*, 633:329–332, 2015.

[34] S. Manni, S. L. Bud'ko, and P. C. Canfield. GdPtPb: A noncollinear antiferromagnet with distorted kagome lattice. *Phys. Rev. B*, 96(5):054435, 2017.

[35] R. Pöttgen, A. Fugmann, R. D. Hoffmann, U. C. Rodewald, and D. Niepmann. Intermetallic cerium compounds with ordered U_3Si_2 type structure. *Z. Naturforsch. B*, 55(2):155–161, 2000.

[36] R. Pöttgen. Er_2Au_2Sn and other ternary rare earth metal gold stannides with ordered Zr_3Al_2-type structure. *Z. Naturforsch. B*, 49(10):1309–1313, 1994.

[37] J. Donohue. Structures of the elements. *John Wiley and Sons, Inc.*, 1974.

[38] R. Movshovich, J. M. Lawrence, M. F. Hundley, J. Neumeier, J. D. Thompson, A. Lacerda, and Z. Fisk. Magnetism in CePtPb. *Phys. Rev. B*, 53(9):5465, 1996.

[39] A. Y. Makhaneva, E. Y. Zakharova, S. N. Nesterenko, S. M. Kazakov, K. A. Lyssenko, A. N. Azarevich, A. V. Bogach, and A. N. Kuznetsov. $Eu_2Pt_3Pb_5$ and $SrPt_2Pb_4$—lead-based intermetallics with $Y_2Rh_3Sn_5/NdRh_2Sn_4$-type polyanionic platinum–lead 3d frameworks. *Dalton Trans.*, 54(6):2393–2402, 2025.

[40] M. Meot-Meyer, G. Venturini, B. Malaman, J. Steinmetz, and B. Roques. De nouveaux stannures ternaires de rhodium et d'elements des terres rares: $TR_2Rh_3Sn_5$ OU TR= Y, Gd, Tb, Dy, Ho. structure cristalline et proprietes electriques et magnetiques de $Y_2Rh_3Sn_5$. *Mater. Res. Bull.*, 19(9):1181–1186, 1984.

[41] M. Meot-Meyer, G. Venturini, B. Malaman, and B. Roques. De nouveaux stannures ternaires de rhodium et d'elements des terres rares: $TR_{1+x}Rh_2Sn_{4-x}$, $0 \leq x \leq 0.5$, TR= La−Sm. *Mater. Res. Bull.*, 20(8):913–919, 1985.

[42] R. Pöttgen and D. Johrendt. Equiatomic intermetallic europium compounds: syntheses, crystal chemistry, chemical bonding, and physical properties. *Chem. Mater.*, 12(4):875–897, 2000.

[43] V. L. Ginzburg, D. A. Kirzhnits, A. K. Agyei, and J. L. Birman. *High-temperature superconductivity.* Springer, 1982.

[44] K. Ishida, Y. Nakai, and H. Hosono. To what extent iron-pnictide new superconductors have been clarified: a progress report. *J. Phys. Soc. Jpn.*, 78(6):062001, 2009.

[45] Y. Kamihara, T. Watanabe, M. Hirano, and H. Hosono. Iron-based layered superconductor $La[O_{1-x}F_x]FeAs$ (x= 0.05- 0.12) with $T_c = 26K$. *JACS*, 130(11):3296–3297, 2008.

[46] B. T. Matthias. Chapter ↓ superconductivity in the periodic system. In *Prog. Low Temp. Phys.*, volume 2, pages 138–150. Elsevier, 1957.

[47] J. Paglione and Richard L. Greene. High-temperature superconductivity in iron-based materials. *Nat. Phys.*, 6(9):645–658, 2010.

[48] R. J. Cava. Structural chemistry and the local charge picture of copper oxide superconductors. *Science*, 247(4943):656–662, 1990.

[49] F. Hayashi, H. Lei, J. G. Guo, and H. Hosono. Modulation effect of interlayer spacing on the superconductivity of electron-doped FeSe-based intercalates. *Inorg. Chem.*, 54(7):3346–3351, 2015.

[50] M. S. Torikachvili, S. L. Bud'ko, N. Ni, and P. C. Canfield. Pressure induced superconductivity in $CaFe_2As_2$. *Phys. Rev. Lett.*, 101(5):057006, 2008.

[51] E. Gati, S. Köhler, D. Guterding, B. Wolf, S. Knöner, S. Ran, S. L. Bud'Ko, P. C. Canfield, and M. Lang. Hydrostatic-pressure tuning of magnetic, nonmagnetic, and superconducting states in annealed $Ca(Fe_{1-x}Co_x)_2As_2$. *Phys. Rev. B*, 86(22):220511, 2012.

[52] Y. Nishikubo, K. Kudo, and M. Nohara. Superconductivity in the honeycomb-lattice pnictide SrPtAs. *J. Phys. Soc. Jpn.*, 80(5):055002, 2011.

[53] S. J. Youn, M. H. Fischer, S. H. Rhim, M. Sigrist, and D. F. Agterberg. Role of strong spin-orbit coupling in the superconductivity of the hexagonal pnictide SrPtAs. *Phys. Rev. B, Condens. Matter Mater. Phys.*, 85(22):220505, 2012.

[54] J. Goryo, M. H. Fischer, and M. Sigrist. Possible pairing symmetries in SrPtAs with a local lack of inversion center. *Phys. Rev. B, Condens. Matter Mater. Phys.*, 86(10):100507, 2012.

[55] M. H. Fischer, T. Neupert, C. Platt, A. P. Schnyder, W. Hanke, J. Goryo, R. Thomale, and M. Sigrist. Chiral d-wave superconductivity in SrPtAs. *Phys. Rev. B*, 89(2):020509, 2014.

[56] W. S. Wang, Y. Yang, and Q. H. Wang. Triplet f-wave pairing in SrPtAs. *Phys. Rev. B*, 90(9):094514, 2014.

[57] A. Akbari and P. Thalmeier. Gap function of hexagonal pnictide superconductor SrPtAs from quasiparticle interference spectrum. *EPL*, 106(2):27006, 2014.

[58] M. Sigrist, D. F. Agterberg, M. H. Fischer, J. Goryo, F. Loder, S. H. Rhim, D. Maruyama, Y. Yanase, T. Yoshida, and S. J. Youn. Superconductors with staggered non-centrosymmetricity. *J. Phys. Soc. Jpn.*, 83(6):061014, 2014.

[59] M. H. Fischer and J. Goryo. Symmetry and gap classification of non-symmorphic SrPtAs. *J. Phys. Soc. Jpn.*, 84(5):054705, 2015.

[60] J. Goryo, Y. Imai, W. B. Rui, M. Sigrist, and A. P. Schnyder. Surface magnetism in a chiral d-wave superconductor with hexagonal symmetry. *Phys. Rev. B*, 96(14):140502, 2017.

[61] S. Sumita and Y. Yanase. Unconventional superconducting gap structure protected by space group symmetry. *Phys. Rev. B*, 97(13):134512, 2018.

[62] M. Sato and Y. Ando. Topological superconductors: a review. *Rep. Prog. Phys.*, 80(7):076501, 2017.

[63] X. L. Qi and S. C. Zhang. Topological insulators and superconductors. *Rev. Mod. Phys.*, 83:1057–1110, Oct 2011.

[64] V. Mourik, K. Zuo, S. M. Frolov, S. R. Plissard, E. P. Bakkers, and L. P. Kouwenhoven. Signatures of majorana fermions in hybrid superconductor-semiconductor nanowire devices. *Science*, 336(6084):1003–1007, 2012.

[65] S. Nadj-Perge, I. K. Drozdov, J. Li, H. Chen, S. Jeon, J. Seo, A. H. MacDonald, B A. Bernevig, and A. Yazdani. Observation of majorana fermions in ferromagnetic atomic chains on a superconductor. *Science*, 346(6209):602–607, 2014.

[66] B. Lian, X. Q. Sun, A. Vaezi, X. L. Qi, and S. C. Zhang. Topological quantum computation based on chiral majorana fermions. *PNAS*, 115(43):10938–10942, 2018.

[67] Q. L. He, L. Pan, A. L. Stern, E. C. Burks, X. Y. Che, G. Yin, J. Wang, B. Lian, Q. Zhou, E. S. Choi, et al. Retracted: Chiral majorana fermion modes in a quantum anomalous hall insulator–superconductor structure. *Science*, 357(6348):294–299, 2017.

[68] G. C. Ménard, S. Guissart, C. Brun, R. T. Leriche, M. Trif, F. Debontridder, D. Demaille, D. Roditchev, P. Simon, and T. Cren. Two-dimensional topological superconductivity in Pb/Co/Si (111). *Nat. Commun.*, 8(1):2040, 2017.

[69] E. Martino, A. Arakcheeva, G. Autes, A. Pisoni, M. D. Bachmann, K. A. Modic, T. Helm, O. V. Yazyev, P. J. W. Moll, L. Forró, et al. $\mathrm{Sr_2Pt_{8-x}As}$: a layered incommensurately modulated metal with saturated resistivity. *IUCr*, 5(4):470–477, 2018.

[70] M. Fujioka, M. Ishimaru, T. Shibuya, Y. Kamihara, C. Tabata, H. Amitsuka, A. Miura, M. Tanaka, Y. Takano, H. Kaiju, et al. Discovery of the Pt-based superconductor $\mathrm{LaPt_5As}$. *JACS*, 138(31):9927–9934, 2016.

[71] J. H. Mooij. Electrical conduction in concentrated disordered transition metal alloys. *Phys. Status Solidi A*, 17(2):521–530, 1973.

[72] M. Armand and J. M. Tarascon. Building better batteries. *Nat.*, 451(7179):652–657, 2008.

[73] J. C. Bachman, S. Muy, A. Grimaud, H. H. Chang, N. Pour, S. F. Lux, O. Paschos, F. Maglia, S. Lupart, P. Lamp, et al. Inorganic solid-state electrolytes for lithium batteries: mechanisms and properties governing ion conduction. *Chem. Rev.*, 116(1):140–162, 2016.

[74] Y. M. Wang, S. F. Song, C. H. Xu, N. Hu, J. Molenda, and L. Lu. Development of solid-state electrolytes for sodium-ion battery–a short review. *Nano Mater. Sci.*, 1(2):91–100, 2019.

[75] Z. Z. Zhang, Y. J. Shao, B. Lotsch, Y. S. Hu, H. Li, J. Janek, L. F. Nazar, C. W. Nan, J. Maier, M. Armand, et al. New horizons for inorganic solid state ion conductors. *Energy Environ. Sci.*, 11(8):1945–1976, 2018.

[76] R. J. Chen, W. J. Qu, X. Guo, L. Li, and F. Wu. The pursuit of solid-state electrolytes for lithium batteries: from comprehensive insight to emerging horizons. *Mater. Horiz.*, 3(6):487–516, 2016.

[77] Y. G. Lee, S. Fujiki, C. Jung, N. Suzuki, N. Yashiro, R. Omoda, D. S. Ko, T. Shiratsuchi, T. Sugimoto, S. Ryu, et al. High-energy long-cycling all-solid-state lithium metal batteries enabled by silver–carbon composite anodes. *Nat. Energy*, 5(4):299–308, 2020.

[78] N. Yabuuchi, K. Kubota, M. Dahbi, and S. Komaba. Research development on sodium-ion batteries. *Chem. Rev.*, 114(23):11636–11682, 2014.

[79] D. Kundu, E. Talaie, V. Duffort, and L. F. Nazar. Natriumionenbatterien für die elektrochemische energiespeicherung. *Angew. Chem.*, 127(11):3495–3513, 2015.

[80] S. W. Kim, D. H. Seo, X. H. Ma, G. Ceder, and K. Kang. Electrode materials for rechargeable sodium-ion batteries: potential alternatives to current lithium-ion batteries. *Adv. Energy Mater.*, 2(7):710–721, 2012.

[81] M. S. Islam, R. Dominko, C. Masquelier, C. Sirisopanaporn, A. R. Armstrong, and P. G. Bruce. Silicate cathodes for lithium batteries: alternatives to phosphates? *J. Mater. Chem.*, 21(27):9811–9818, 2011.

[82] W. Lee, S. Muhammad, C. Sergey, H. Lee, J. Yoon, Y. M. Kang, and W. S. Yoon. Advances in the cathode materials for lithium rechargeable batteries. *Angew. Chem. Int. Ed.*, 59(7):2578–2605, 2020.

[83] V. Palomares, M. Casas-Cabanas, E. Castillo-Martínez, M. H. Han, and T. Rojo. Update on na-based battery materials. a growing research path. *Energy Environ. Sci.*, 6(8):2312–2337, 2013.

[84] H. Kim, J. Hong, K. Y. Park, H. Kim, S. W. Kim, and K. Kang. Aqueous rechargeable Li and Na ion batteries. *Chem. Rev.*, 114(23):11788–11827, 2014.

[85] Y. K. Sun. Promising all-solid-state batteries for future electric vehicles, 2020.

[86] K. B. Hatzell, X. C. Chen, C. L. Cobb, N. P. Dasgupta, M. B. Dixit, L. E. Marbella, M. T. McDowell, P. P. Mukherjee, A. Verma, V. Viswanathan, et al. Challenges in lithium metal anodes for solid-state batteries. *ACS Energy Lett.*, 5(3):922–934, 2020.

[87] H. Liu, X. B. Cheng, J. Q. Huang, H. Yuan, Y. Lu, C. Yan, G. L. Zhu, R. Xu, C. Z. Zhao, L. P. Hou, et al. Controlling dendrite growth in solid-state electrolytes. *ACS Energy Lett.*, 5(3):833–843, 2020.

[88] M. A. Kraft, S. P. Culver, M. Calderon, F. Böcher, T. Krauskopf, A. Senyshyn, C. Dietrich, A. Zevalkink, J. Janek, and W. G. Zeier. Influence of lattice polarizability on the ionic conductivity in the lithium superionic argyrodites Li_6PS_5X (X= Cl, Br, I). *JACS*, 139(31):10909–10918, 2017.

[89] N. Kamaya, K. Homma, Y. Yamakawa, M. Hirayama, R. Kanno, M. Yonemura, T. Kamiyama, Y. Kato, S. Hama, K. Kawamoto, et al. A lithium superionic conductor. *Nat. Mater.*, 10(9):682–686, 2011.

[90] P. Bron, S. Johansson, K. Zick, J. Schmedt auf der Günne, S. Dehnen, and B. Roling. $Li_{10}SnP_2S_{12}$: an affordable lithium superionic conductor. *JACS*, 135(42):15694–15697, 2013.

[91] E. Rangasamy, Z. C. Liu, M Gobet, K. Pilar, G. Sahu, W. Zhou, H. Wu, S. Greenbaum, and C. D. Liang. An iodide-based $Li_7P_2S_8I$ superionic conductor. *JACS*, 137(4):1384–1387, 2015.

[92] H. Yamane, M. Shibata, Y. Shimane, T. Junke, Y. Seino, S. Adams, K. Minami, A. Hayashi, and M. Tatsumisago. Crystal structure of a superionic conductor, $Li_7P_3S_{11}$. *Solid State Ion.*, 178(15-18):1163–1167, 2007.

[93] Y. Inoue, K. Suzuki, N. Matsui, M. Hirayama, and R. Kanno. Synthesis and structure of novel lithium-ion conductor $Li_7Ge_3PS_{12}$. *J. Solid State Chem.*, 246:334–340, 2017.

[94] F. Tsuji, N. Tanibata, A. Sakuda, A. Hayashi, and M. Tatsumisago. Preparation of sodium ion conductive $Na_{10}GeP_2S_{12}$ glass-ceramic electrolytes. *Chem. Lett.*, 47(1):13–15, 2018.

[95] M. Duchardt, U. Ruschewitz, S. Adams, S. Dehnen, and B. Roling. Vacancy-controlled na+ superion conduction in $Na_{11}Sn_2PS_{12}$. *Angew. Chem. Int. Ed.*, 57(5):1351–1355, 2018.

[96] A. Hayashi, K. Noi, A. Sakuda, and M. Tatsumisago. Superionic glass-ceramic electrolytes for room-temperature rechargeable sodium batteries. *Nat. Commun.*, 3(1):856, 2012.

[97] S. Takeuchi, K. Suzuki, M. Hirayama, and R. Kanno. Sodium superionic conduction in tetragonal Na_3PS_4. *J. Solid State Chem.*, 265:353–358, 2018.

[98] L. Zhang, D. C. Zhang, K Yang, X. L. Yan, L. M. Wang, J. L. Mi, B. Xu, and Y. M. Li. Vacancy-contained tetragonal Na_3SbS_4 superionic conductor. *Adv. Sci.*, 3(10):1600089, 2016.

[99] Z. X. Yu, S. L. Shang, J. H. Seo, D. W. Wang, X. Y. Luo, Q. Q. Huang, S. R. Chen, J. Lu, X. L. Li, Z. K. Liu, et al. Exceptionally high ionic conductivity in $Na_3P_{0.62}As_{0.38}S_4$ with improved moisture stability for solid-state sodium-ion batteries. *Adv. Mater.*, 29(16):1605561, 2017.

[100] A. Hayashi, N. Masuzawa, S. Yubuchi, F. Tsuji, C. Hotehama, A. Sakuda, and M. Tatsumisago. A sodium-ion sulfide solid electrolyte with unprecedented conductivity at room temperature. *Nat. Commun.*, 10(1):5266, 2019.

[101] S. Harm, A. K. Hatz, C. Schneider, C. Hoefer, C. Hoch, and B. V. Lotsch. Finding the right blend: interplay between structure and sodium ion conductivity in the system $Na_5AlS_4 - Na_4SiS_4$. *Front. Chem.*, 8:90, 2020.

[102] B. Eisenmann and M. Somer. Neue ternäre alkaliphosphide mit kupfer, zink und cadmium: $K_2CuP, NaZnP$ und K_4CdP_2 on new ternary alkali metal phosphides: $K_2CuP, NaZnP$ and K_4CdP_2. *Z. Naturforsch. B*, 40(11):1419–1423, 1985.

[103] B. Eisenmann and M. Somer. K_2SiP_2, ein phosphidopolysilikat (iv)/K_2SiP_2, a phosphidopolysilicate (iv). *Z. Naturforsch. B*, 39(6):736–738, 1984.

[104] K. Feng, L. Kang, W. L. Yin, W. Y. Hao, Z. S. Lin, J. Y. Yao, and Y. C. Wu. KSi_2P_3: A new layered phosphidopolysilicate (iv). *J. Solid State Chem.*, 205:129–133, 2013.

[105] A. J. Springthorpe and J. G. Harrison. $MgSiP_2$: a new member of the II IV V_2 family of semiconducting compounds. *Nat.*, 222(5197):977–977, 1969.

[106] H. G. von Schnering and G. Menge. $AlSiP_3$, a compound with a novel wurtzite-pyrite intergrowth structure. *J. Solid State Chem.*, 28(1):13–19, 1979.

[107] X. Zhang, T. T. Yu, C. L. Li, S. P. Wang, and X. T. Tao. Synthesis and crystal structures of the calcium silicon phosphides $Ca_2Si_2P_4, Ca_3Si_8P_{14}$ and $Ca_3Si_2P_4$. *Z. Anorg. Allg. Chem.*, 641(8-9):1545–1549, 2015.

[108] J. Wallinda and W. Jeitschko. $Ni_{1.282(4)}Si_{1.284(5)}P_3$ or $NiSi_2P_3$: two solutions with different atom distributions for one single-crystal x-ray data set, both refined to residuals of less than 2.5%. *J. Solid State Chem.*, 114(2):476–480, 1995.

[109] H. Vincent, J. Kreisel, C. H. Perrier, O. Chaix-Pluchery, P. Chaudouet, R. Madar, F. Genet, and G. Lucazeau. Synthesis, crystal structure, raman spectroscopy, and physical characterization of a new cobalt phospho-silicide $CoSi_3P_3$. *J. Solid State Chem.*, 124(2):366–373, 1996.

[110] P. Kaiser and W. Jeitschko. Preparation and crystal structures of the ternary compounds Ag_2SiP_2 and AuSiP. *Z. Naturforsch. B*, 52(4):462–468, 1997.

[111] P. Kaiser and W. Jeitschko. Preparation and crystal structure of the copper silicon polyphosphide Cu_4SiP_8. *Z. Anorg. Allg. Chem.*, 622(1):53–56, 1996.

[112] P. Kaiser and W. Jeitschko. The rare earth silicon phosphides $LnSi_2P_6$ (Ln = La, Ce, Pr, and Nd). *J. Solid State Chem.*, 124(2):346–352, 1996.

[113] Z. C. Liu, W. J. Fu, E. A. Payzant, Xiang Yu, Z. Wu, N. J. Dudney, J. Kiggans, K. L. Hong, A. J. Rondinone, and C. D. Liang. Anomalous high ionic conductivity of nanoporous β-Li_3PS_4. *JACS*, 135(3):975–978, 2013.

[114] M. A. Kraft, S. Ohno, T. Zinkevich, R. Koerver, S. P. Culver, T. Fuchs, A. Senyshyn, S. Indris, B. J. Morgan, and W. G. Zeier. Inducing high ionic conductivity in the lithium superionic argyrodites $Li_{6+x}P_{1-x}Ge_xS_5I$ for all-solid-state batteries. *JACS*, 140(47):16330–16339, 2018.

[115] X. Li, J. W. Liang, J. Luo, M. N. Banis, C. H. Wang, W. H. Li, S. X. Deng, C. Yu, F. P. Zhao, Y. F. Hu, et al. Air-stable Li_3InCl_6 electrolyte with high voltage compatibility for all-solid-state batteries. *Energy Environ Sci.*, 12(9):2665–2671, 2019.

[116] H. J. Steiner and H. D. Lutz. Neue schnelle ionenleiter vom typ $\mathrm{M}^{3}_{\mathrm{I}}\mathrm{M}^{\mathrm{III}}\mathrm{Cl}_6(\mathrm{M}^{\mathrm{I}} = \mathrm{Li, Na, Ag}; \mathrm{M}^{\mathrm{III}} = \mathrm{In, Y})$. *Z. Anorg. Allg. Chem.*, 613(7):26–30, 1992.

[117] T. Asano, A. Sakai, S. Ouchi, M. Sakaida, A. Miyazaki, and S. Hasegawa. Solid halide electrolytes with high lithium-ion conductivity for application in 4 v class bulk-type all-solid-state batteries. *Adv. Mater.*, 30(44):1803075, 2018.

[118] L. Toffoletti, H. Kirchhain, J. Landesfeind, W. Klein, L. van Wüllen, H. A. Gasteiger, and T. F. Fässler. Lithium ion mobility in lithium phosphidosilicates: crystal structure, 7Li, 29Si, and 31 P MAS NMRspectroscopy, and impedance spectroscopy of $\mathrm{Li_8SiP_4}$ and $\mathrm{Li_2SiP_2}$. *Chem. Eur. J.*, 22(49):17635–17645, 2016.

[119] H. Nazir, M. Batool, F. J. Bolivar Osorio, M. Isaza-Ruiz, X. Xu, K. Vignarooban, P. Phelan, Inamuddin, and A. M. Kannan. Recent developments in phase change materials for energy storage applications: A review. *Int. J. Heat Mass Transf.*, 129:491–523, 2019.

[120] M. Sawicki and L. L. Shaw. Advances and challenges of sodium ion batteries as post lithium ion batteries. *Rsc Advances*, 5(65):53129–53154, 2015.

[121] H. Pan, Y. S. Hu, and L. Q. Chen. Room-temperature stationary sodium-ion batteries for large-scale electric energy storage. *Energy Environ. Sci.*, 6(8):2338–2360, 2013.

[122] H. Vikström, S. Davidsson, and M. Höök. Lithium availability and future production outlooks. *Appl. Energy*, 110:252–266, 2013.

[123] H. Li, J. Kim, T. L. Groy, M. O'Keeffe, and O. M. Yaghi. 20 å $\mathrm{Cd_4In_{16}S_35_{14}}$-supertetrahedral T4 clusters as building units in decorated cristobalite frameworks. *JACS*, 123(20):4867–4868, 2001.

[124] X. F. Xu, W. Wang, D. L. Liu, D. D. Hu, T. Wu, X. H. Bu, and P. Y. Feng. Pushing up the size limit of metal chalcogenide supertetrahedral nanocluster. *JACS*, 140(3):888–891, 2018.

[125] Z. Q. Li, C. J. Mo, Y. Guo, N. N. Xu, Q. Y. Zhu, and J. Dai. Discrete supertetrahedral CuInS nanoclusters and their application in fabrication of cluster-sensitized $\mathrm{TiO_2}$ photoelectrodes. *Journal of Materials Chemistry A*, 5(18):8519–8525, 2017.

[126] M. Döch, A. Hammerschmidt, S. Pütz, and B. Krebs. Isolated $\mathrm{B_{10}Se_{20}}$-macrotetrahedra in the novel quarternary selenoborate $\mathrm{Li_{6-2x}Sr_{2+x}B_{10}Se_{20}}$ $(\mathrm{x} \approx 0.7)$. *Phosphorus, Sulfur, and Silicon*, 179(4-5):933–935, 2004.

[127] A. Haffner, T. Bräuniger, and D. Johrendt. Supertetrahedral networks and lithium-ion mobility in $\mathrm{Li_2SiP_2}$ and $\mathrm{LiSi_2P_3}$. *Angew. Chem. Int. Ed.*, 55(43):13585–13588, 2016.

[128] A. Haffner, A. K. Hatz, I. Moudrakovski, B. V. Lotsch, and D. Johrendt. Fast sodium-ion conductivity in supertetrahedral phosphidosilicates. *Angew. Chem.*, 130(21):6263–6268, 2018.

[129] M. Hostettler and D. Schwarzenbach. Phase diagrams and structures of HgX_2 $(X = I, Br, Cl, F)$. *C. R. Chim.*, 8(2):147–156, 2005.

[130] M. O'Keeffe, M. Eddaoudi, H. Li, T. Reineke, and O. M. Yaghi. Frameworks for extended solids: geometrical design principles. *J. Solid State Chem.*, 152(1):3–20, 2000.

[131] F. Hiltmann, P. Zum Hebel, A. Hammerschmidt, and B. Krebs. Li5b7s13 und li9b19s33: Zwei lithiumthioborate mit neuen hochpolymeren anionengerüsten. *Z. Anorg. Allg. Chem.*, 619(2):293–302, 1993.

[132] C. Wang, X. H. Bu, N. F. Zheng, and P. Y. Feng. Nanocluster with one missing core atom: a three-dimensional hybrid superlattice built from dual-sized supertetrahedral clusters. *JACS*, 124(35):10268–10269, 2002.

[133] T. Sasaki, H. Takizawa, K. Uheda, T. Yamashita, and T. Endo. High-pressure synthesis and crystal structure of B_2S_3. *J. Solid State Chem.*, 166(1):164–170, 2002.

[134] A. Lasia. Applications of electrochemical impedance spectroscopy to hydrogen adsorption, evolution and absorption into metals. In *Modern aspects of electrochemistry*, pages 1–49. Springer, 2002.

[135] A. Haffner, A. K. Hatz, O. E. Zeman, C. Hoch, B. V. Lotsch, and D. Johrendt. Polymorphism and fast potassium-ion conduction in the T5 supertetrahedral phosphidosilicate KSi_2P_3. *Angew. Chem. Int. Ed.*, 60(24):13641–13646, 2021.

Chapter 2

Structural and Physical Properties of NdPtAs

2.1 Abstract

The ternary compound NdPtAs ($a = b = 4.3070(1)$Å, $c = 15.7054(4)$Å) has been prepared by reaction of the elements at 900°C. Single-crystal X-ray diffraction reveals that NdPtAs crystallizes in the hexagonal space group $P6_3/mmc$, belonging to the YPtAs-type structure characterized by puckered Pt–As honeycomb layers alternating with Nd layers along the c-axis. EDX confirms the elemental composition consistent with NdPtAs The presence of 15.81% NdAs as a secondary phase is indicated by powder X-ray diffraction. Magnetic susceptibility data follow modified Curie–Weiss behavior at high temperatures, yielding an effective magnetic moment of $\mu_{\mathrm{eff}} = 3.12\ \mu_{\mathrm{B}}$ and a negative Weiss constant $\theta_{\mathrm{P}} = -9.83(10)$ K, indicative of antiferromagnetic interactions. A clear anomaly in both susceptibility and resistivity at ~ 9 K signals the onset of long-range magnetic order. Isothermal magnetization measurements support antiferromagnetic behavior at low temperatures. The structural and magnetic similarities to SmPtAs suggest conserved magnetic exchange mechanisms across the *RE*PtAs series.

2.2 Introduction

Layered transition-metal pnictides with honeycomb networks have garnered significant attention due to their rich structural diversity and intriguing physical properties, including unconventional superconductivity and possible topological states [1–3]. Particular attention has been drawn to SrPtAs and $SrPt_2As_2$, which exhibit superconducting transition temperatures T_{c} - values of 2.4K and 5.2K, respectively [4].

A key structural motif in this family is derived from the AlB_2- type structure, where the *AE* occupies the Al site, while the transition and pnicogen atoms form planar honeycomb networks [5, 6]. A representative example is SrPtAs, which crystallizes in the ZrBeSi-type structure ($P6_3/mmc$, D^4_{6h}, No.194), an ordered variant of the AlB_2- type structure.

In this structure, platinum and arsenic atoms are alternately arranged in the B-site of the honeycomb layer, while the alkaline earth atom (e.g., Sr) occupies the interstitial site analogous to Al in AlB_2 [6]. These honeycomb layers stack along the c-axis in such a manner that each As atom lies directly beneath a Pt atom, and vice versa, resulting in a globally centrosymmetric structure with locally broken inversion symmetry in the PtAs honeycomb network. Theoretical studies have suggested that this symmetry breaking, combining with strong spin-orbit coupling from Pt, and weak interplay coupling between the PtAs layers, predict to give rise to several exotic superconducting states [7–15], such as the singlet-triplet mixed state[8], chiral *d*-wave state [9], and *f*-wave state[10]. In the latter, superconductivity occurs near a charge-density-wave (CDW) state, indicating an inelastic electron-phonon interaction. Another remarkable compound is $Ca_{10}(Pt_4As_8)(Fe_{2-x}Pt_xAs_2)_5$, which despite significant Pt doping and the presence of metallic PtAs-block layers between FeAs- layers, exhibits a superconducting transition at approximately 38 K [2, 16–20].

Variations on the ideal honeycomb geometry occur in compounds such as CaPtAs and EuPtAs, which maintain a relationship to the AlB_2-type motif but with rotated hexagonal PtAs units [5]. In these compounds, the honeycomb layers are rotated by 90° along $z/4$, forming a three-dimensional network. While CaPtAs retains interconnected hexagons, this continuity is lost in EuPtAs. Despite these differences, both maintain trigonal hexagons Pt-As coordination and hexagonal prismatic environments for the *AE*/ *RE* atom (Ca or Eu) at the $4a$ Wyckoff position [5].

Additional complexity arises in *AE*/ *RE*PtAs pnictides [5, 6, 21]. For instance, BaPtAs has been reported to crystallize in multiple structure types depending on heat treatments, including SrPtSb-type ($P\overline{6}m2$, D^1_{3h}, No.187), YPtAs-type ($P6_3/mmc$, D^4_{6h}, No.194) and LaIrSi-type ($P2_13$, T^4, No.198) [22]. Each of these structures involves different stacking sequences and coordination geometries of Pt and As atoms. Meanwhile, a broader family of rare-earth platinum arsenides *RE*PtAs (RE = Y, Sm, Gd, Dy, Ho, Er, Tm, Yb, Lu) have also reported with the YPtAs-type structure ($P6_3/mmc$) [23]. These materials introduce the possibility of coupling between localized $4f$ magnetism and the electronic structure of the PtAs honeycomb layers, which may further enrich their physical behavior.

Despite the growing number of structurally characterized compounds in this family, no report exists for NdPtAs. Its structural type, electronic ground state, and physical behavior have not been comprehensively explored. In this work, we report the synthesis and structural characterization of NdPtAs, placing it in the context of the broader *RE*–Pt–As family. Our aim is to determine whether NdPtAs conforms to known structural trends and to provide a basis for future investigation into its potential electronic and magnetic properties.

2.3 Results and Discussion

The title compounds were synthesized via solid-state reactions involving multiple annealing steps of the respective elemental mixtures under an argon atmosphere in alumina crucibles. Following the synthesis, polycrystalline black powders were obtained containing approximately 15.81% NdAs as an impurity (Figure 2.1). Due to its high thermodynamic stability, NdAs consistently forms during the synthesis and could not be eliminated.

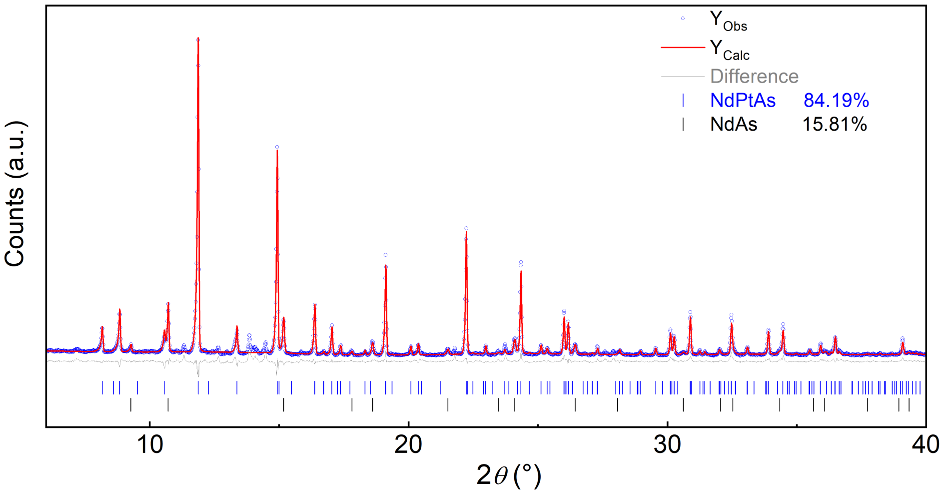

Figure 2.1: X-Ray powder pattern of NdPtAs (blue) with Rietveld fit (red) and difference plot (grey)

Small single crystals were selected from the samples for EDX analysis and single crystal X-ray diffraction analyses. EDX analysis confirmed that the compound has the expected chemical composition. Single crystal X-ray diffraction data were consistent with a hexagonal unit cell, and structure refinement in space group $P6_3/mmc$ yielded precise lattice parameters for the crystal investigated. The crystal structure was solved by direct methods and refined using the least squares approach with SHLEX. Crystallographic data are compiled in Table 2.1.

NdPtAs crystallizes in the YPtAs-type structure [22], which is related to the SmPtAs-type (Pearson symbol $hP12$, Wyckoff sequence $f_2\,b\,a$)) [24]. This atomic arrangement can be described as puckered honeycomb net layers composed of Pt and As atoms, stacked along the c-axis and separated by layers of Nd atoms.

Due to the three-connected two-dimensional PtAs networks, the structure is a derivative of the AlB_2-type. However, unlike the planar honeycomb layers of the ideal AlB_2-type, NdPtAs features slightly puckered hexagonal nets where Pt and As atoms are arranged in an ordered way. The structure is identical to that observed in other *RE*PtAs compounds [24], with a repeating sequence of two Pt atoms followed by two As atoms. Thus, the Nd atoms are coordinated by two distinct types of polyhedra - both consist of six Pt and six As atoms - forming slightly distorted hexagonal prisms, which can be described as combinations of two prisms and two antiprisms. The structure is shown in Figure 2.2.

The Pt–As bonding in NdPtAs can be compared to related compounds such as EuPtP and SrPtAs, where similar Pt–X (X = P–Sb) hexagonal nets are observed [5]. In these compounds, the Pt–X layers are typically planar, while in NdPtAs (and other *RE*PtAs [24] or *RE*PtSb [25] structures), the layers are slightly puckered. This puckering affects the layer stacking along the c-axis, but not to a degree that suggests strong covalent

Table 2.1: Crystallographic data for the refinement of NdPtAs.

Formula	NdPtAs
Space Group	$P6_3/mmc$ (No. 194)
a / Å	4.3070(1)
b / Å	4.3070(1)
c / Å	15.7054(4)
V_{cell} / Å^3	252.31(1)
Z	2
$\rho_{\text{X-ray}}$ / g cm^{-3}	10.9
μ / mm^{-1}	88.34
Θ-range / °	2.594-29.005
reflections measured	4849
independent reflections	158
parameters	13
R_σ	0.0078
R_{int}	0.0329
R_1 ($F^2 > 2\sigma$ (F^2)) / all	0.0227/0.0251
wR_2 ($F^2 > 2\sigma$ (F^2)) / all	0.0755/0.0782
GooF	0.983
$\Delta\rho_{\text{max/min}}$ / e Å^{-3}	2.006/-1.265

Table 2.2: Atomic coordinates, equivalent displacement parameters (Å^2) of NdPtAs. U_{eq} is defined as one third of the trace of the orthogonalized U_{ij} tensor

Atom	Wyckoff	x	y	z	U_{eq}
Pt1	4f	1/3	2/3	0.13031(4)	0.0081
As1	4f	1/3	2/3	0.62044(11)	0.0084
Nd1	2a	0	0	0	0.0065
Nd2	2b	0	0	1/4	0.0065

Table 2.3: Selected distances (Å) in NdPtAs.

atoms	distance(Å)	atoms	distance(Å)
Pt1—As1	2.4915(1)	Pt1—Nd1^{ii}	3.2205(4)
Pt1—As1^{i}	2.4915(2)	As1—Nd1^{i}	3.1243(11)
Pt1—As1^{ii}	2.4915(2)	As1—Nd1	3.1243(11)
Pt1—Nd2^{iii}	3.1172(4)	As1—Nd1^{ii}	3.1243(11)
Pt1—Nd2^{iv}	3.1172(4)	As1—Nd2^{iii}	3.2130(11)
Pt1—Nd2^{v}	3.1172(4)	As1—Nd2^{vii}	3.2130(11)
Pt1—Nd1^{i}	3.2205(4)	As1—Nd2^{v}	3.2130(11)
Pt1—Nd1^{vi}	3.2205(4)		

interactions between layers, as seen in more distorted structures like CaPtSb and EuPtSb (ordered $CeCu_2$ type) [5].

Figure 2.3 shows the temperature dependence of the magnetic susceptibility χ and inverse magnetic susceptibility χ^{-1} of NdPtAs, measured while warming in a dc field of 3 T after zero field cooling to the lowest temperature (1.9 K). The susceptibility χ increases with decreasing temperature T and exhibits an upturn below 50 K. A clear hump is seen around 9 K, indicating the onset of magnetic ordering. The temperature dependence of magnetic susceptibility $\chi(T)$ follows a modified Curie–Weiss law, $\chi = \chi_0 + \mathrm{C}/(\mathrm{T} - \theta_\mathrm{P})$ from which an effective magnetic moment μ_eff and a Weiss temperature θ_P can be extracted. The fitted Weiss constant Figure 2.3 shows the temperature dependence of the magnetic susceptibility χ and inverse magnetic susceptibility χ^{-1} of NdPtAs, measured while warming in a dc field of 3 T after zero field cooling to the lowest temperature (1.9 K). The susceptibility χ increases with decreasing temperature T and exhibits an upturn below 50 K. A clear hump is seen around 9 K, indicating the onset of magnetic ordering. The temperature dependence of magnetic susceptibility $\chi(T)$ follows a modified Curie–Weiss law, $\chi = \chi_0 + \mathrm{C}/(\mathrm{T} - \theta_\mathrm{P})$ from which an effective magnetic moment μ_eff and a Weiss temperature θ_P can be extracted. The fitted Weiss constant θ_P = -9.8(1) K indicates dominant antiferromagnetic interactions. The crystal structure of NdPtAs is identical to that of SmPtAs, both adopting the hexagonal YPtAs-type structure. Given their isotypic relationship, similar magnetic behavior may be anticipated for NdPtAs and SmPtAs. SmPtAs is known to undergo antiferromagnetic ordering of the electron spin [24]. The magnetic properties observed in NdPtAs—such as the negative Weiss constant, the low-temperature susceptibility anomaly, and the general Curie–Weiss behavior—support the assumption of a comparable antiferromagnetic ground state. The crystal structure of NdPtAs is identical to that of SmPtAs, both adopting the hexagonal YPtAs-type structure. Given this close

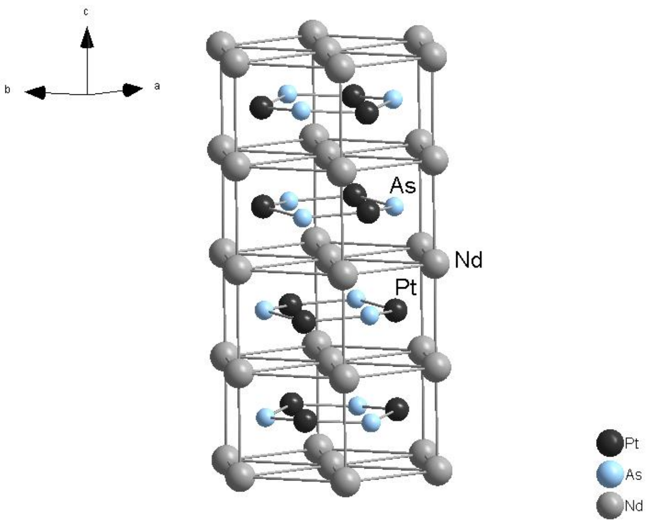

Figure 2.2: The crystal structure of NdPtAs. Neodymium, platinum, and arsenic atoms are drawn as light grey, black, and blue, respectively.

structural relationship, it is reasonable to expect that they exhibit similar magnetic behavior. SmPtAs is known to undergo antiferromagnetic ordering of the electron spin [24]. The magnetic properties observed in NdPtAs—such as the negative Weiss constant, the low-temperature susceptibility anomaly, and the general Curie–Weiss behavior—support the assumption of a comparable antiferromagnetic ground state.

The paramagnetic effective magnetic moments of the neodymium monopnictides are generally close to the free-ion value of Nd^{3+} (3.62 μ_B) [26–28]. For NdP and NdAs, Curie–Weiss fits typically yield $\mu_{\mathrm{eff}} \approx 3.6\ \mu_B$ [29], while for NdSb a slightly higher value of $\mu_{\mathrm{eff}} = 3.75\ \mu_B$ has been reported [30]. At higher temperatures, Curie–Weiss behavior is observed with an effective magnetic moment of 3.12 μ_B, lower than the free-ion value of 3.62 μ_B for Nd^{3+}. This discrepancy may partly arise from the 15.8 % NdAs side phase present in the sample. Such small deviations, either slightly below or above the free-ion value, are commonly attributed to crystal-field effects and weak hybridization of Nd $4f$ states with pnictogen p states.

Isothermal magnetization measurements at 1.9 K and 300 K are presented in Figure 2.4. At 1.9 K, the M–H curve shows a steep initial increase at low fields followed by an approximately linear dependence at higher fields, behavior that resembles a mixture of ferromagnetic-like and paramagnetic (or weakly antiferromagnetic) components rather than a simple antiferromagnetic order. In contrast, the linear M–H behavior at 300 K confirms the paramagnetic nature of the compound at room temperature.

The temperature dependence of the electrical resistivity of NdPtAs is shown in Figure 2.5. From the ρ data, a distinct change of slope is observed at approximately 9.4 K in the low-temperature region, indicating a magnetic transition. Such slope anomalies in resistivity data are often used as alternative estimates for the Néel temperature. The transition temperature obtained from resistivity is in good agreement with that inferred from sus-

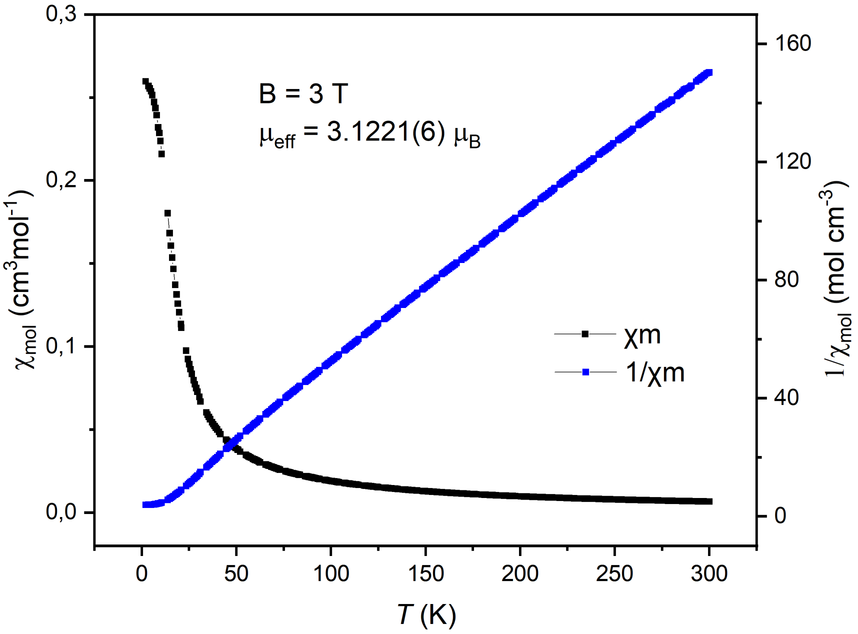

Figure 2.3: The magnetic susceptibility (left axis, black dot) and inverse magnetic susceptibility (right axis, blue dot) of NdPtAs measured from 2-300 K in an applied field of H = 3 T.

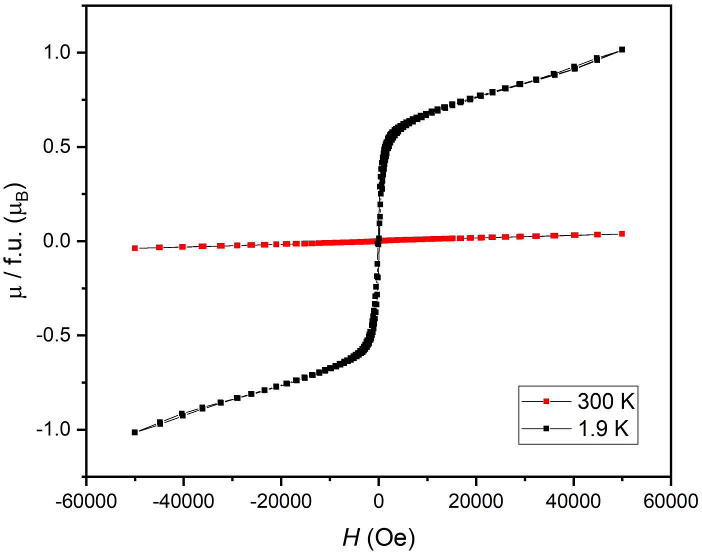

Figure 2.4: $M(H)$ curves for NdPtAs at 1.9 K and 300 K with an applied field of ± 50 kOe.

ceptibility measurements, supporting the assignment of an antiferromagnetic ground state in NdPtAs.

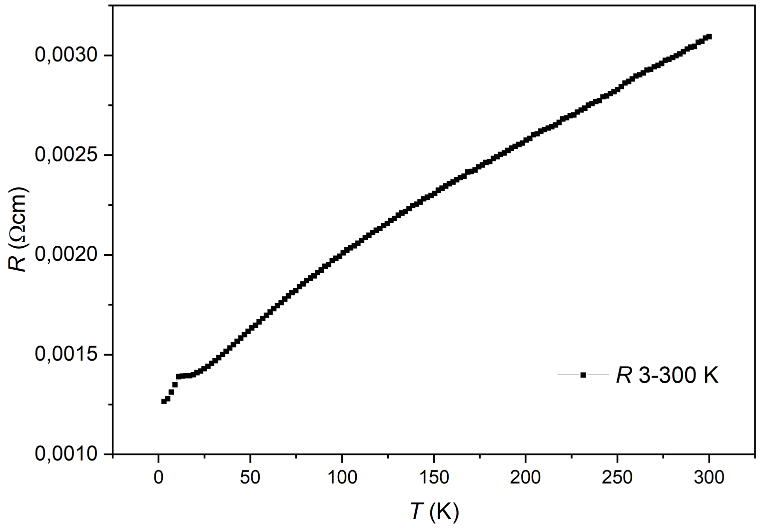

Figure 2.5: Temperature dependence of the specific resistivity of NdPtAs.

2.4 Experimental Section

Synthesis. NdPtAs was prepared by solid-state reaction of a stoichiometric mixture of metallic Neodym (111.04 mg, Alfa Aesar, 99.99%), platinum powder (136.52 mg, Agosi, 99.9%), arsenic powder (52.433 mg, Alfa Aesar, 99.999%). The reaction mixture was ground and filled in an alumina crucible under inert conditions in an argon-filled glovebox with concentrations of O_2 and H_2O <0.1 ppm. This mixture was sealed in a quartz tube and fired in a tube furnace to 600°C within 20h before the temperature was raised to 900°C and maintained for 20h. After cooling to room temperature, the still inhomogeneous product was ground thoroughly and reheated to the same temperature twice, yielding a polycrystalline and air-stable black powder.

Single Crystal X-ray Diffraction. Crystals of sufficient quality for diffraction experiments were selected under dried paraffin oil and mounted the crystal on a micro mount (MiTeGen, America, 50μ sample aperture). Diffraction was collected on a Brucker D8 Quest diffractometer with a microfocus Mo-$K\alpha$ X-ray source, Göbel mirror optics, and Photon II detector. The software package APEX3 [31] was used for data reduction and absorption correction. Space group determination was carried out with XPREP [32] based on systematically absent reflections. SHELX-97[33] was used for the structure solution and refinement. A visualization of the crystal structure was carried out with DIAMOND software.

Powder X-ray Diffraction. A polystalline sample was ground and sealed in Hilgenberg capillaries to avoid hydrolysis. Data were collected on a Stadi P powder diffractometer (STOE & Cie GmbH, Darmstadt, Germany) equipped with a Mythen 1K detector (Dectris, Baden, Switzerland) in Debye-Scherrer geometry with a Ge (111) monochromator and Ag $K\alpha$ radiation. Rietveld refinement based on single-crystal diffraction data was performed with TOPAS [34] software.

High-temperature Powder X-ray Diffraction. A powdered sample was filled and sealed with grease in a silica capillary (Hilgenberg GmbH) with a diameter of 0.4 mm. Data were collected between 298 and 1273 K with a Stoe Stadi-P diffractometer(Mo Kα, Ge(111) monochromator, IP-PSD detector) equipped with a graphite furnace. The data was analyzed with WINXPOW [35].

EDX Measurement. A Carl Zeiss EVO-MA with SE and BSE detectors controlled by the SmartSEM [36] software was used for scanning electron microscopy. EDX measurements were performed with the attached Bruker Nano EDX detector (X-Flash detector 410-M). Data evaluation was performed with the QUANTAX 200 software [37]. Signals from the alumina sample holder and adhesive carbon tabs were disregarded.

Resistivity Measurements. A sample was pressed into a pellet. Resistivity measurements were performed with a Quantum Design Inc. PPMS (Physical Property Measurement System) equipped with a resistivity option. The pellet was contacted with a four-point Van-der-Pauw press contact by Wimbush. Data were collected with the MULTIVU software between 150 and 300K with field strengths of ±50 KOe [38].

2.5 Conclusion

NdPtAs crystallizes in the YPtAs-type hexagonal structure $P6_3/mmc$, characterized by puckered Pt–As honeycomb layers interleaved with Nd layers, closely mirroring the structure of SmPtAs. Despite the presence of 15.8% NdAs as an impurity phase, magnetic measurements indicate antiferromagnetic ordering below $\sim$ 9 K. The effective magnetic moment μ_{eff} = 3.12 μ_{B} and negative Weiss constant θ_{P} = -9.83(10) K extracted from Curie–Weiss analysis are consistent with localized Nd^{3+} moments and dominant antiferromagnetic exchange interactions. The structural and magnetic similarities to SmPtAs. With this result, the *RE*PtAs (*RE* = La–Nd) series is now complete, and NdPtAs reinforces the structural and magnetic trends observed across the family.

References

[1] K. Kudo, Y. Nishikubo, and M. Nohara. Coexistence of superconductivity and charge density wave in $SrPt_2As_2$. *J. Phys. Soc. Jpn.*, 79(12):123710, 2010.

[2] I. R. Shein and A. L. Ivanovskii. Electronic bands, fermi surface, and elastic properties of new 4.2 K superconductor srptas with a honeycomb structure from first principles calculations. *Physica C Supercond.*, 471(19-20):594–596, 2011.

[3] V. V. Bannikov, I. R. Shein, and A. L. Ivanovskii. Structural and electronic properties and the fermi surface of the new non-centrosymmetric superconductors: 3.6 K $CaIrSi_3$ and 2.3 K $CaPtSi_3$. *JETP letters*, 92:343–347, 2010.

[4] Y. Nishikubo, K. Kudo, and M. Nohara. Superconductivity in the honeycomb-lattice pnictide SrPtAs. *J. Phys. Soc. Jpn.*, 80(5):055002, 2011.

[5] G. Wenski and A. Mewis. Ternäre varianten des AlB_2-typs. darstellung und struktur von Ca(Eu)PtX (X = P, As, Sb), $CaPt_xP_{2-x}$, $EuPt_xP(As)_{2-x}$ und $CaPt_xAs_{0,9}$. *Z. Anorg. Allg. Chem.*, 543(12):49–62, 1986.

[6] K. Kudo, Y. Saito, T. Takeuchi, S. Ayukawa, T. Kawamata, S. Nakamura, Y. Koike, and M. Nohara. Superconductivity in BaPtSb with an ordered honeycomb network. *J. Phys. Soc. Jpn.*, 87(6):063702, 2018.

[7] S. J. Youn, M. H. Fischer, S. H. Rhim, M. Sigrist, and D. F. Agterberg. Role of strong spin-orbit coupling in the superconductivity of the hexagonal pnictide SrPtAs. *Phys. Rev. B, Condens. Matter Mater. Phys.*, 85(22):220505, 2012.

[8] J. Goryo, M. H. Fischer, and M. Sigrist. Possible pairing symmetries in SrPtAs with a local lack of inversion center. *Phys. Rev. B, Condens. Matter Mater. Phys.*, 86(10):100507, 2012.

[9] M. H. Fischer, T. Neupert, C. Platt, A. P. Schnyder, W. Hanke, J. Goryo, R. Thomale, and M. Sigrist. Chiral d-wave superconductivity in SrPtAs. *Phys. Rev. B*, 89(2):020509, 2014.

[10] W. S. Wang, Y. Yang, and Q. H. Wang. Triplet f-wave pairing in SrPtAs. *Phys. Rev. B*, 90(9):094514, 2014.

[11] A. Akbari and P. Thalmeier. Gap function of hexagonal pnictide superconductor SrPtAs from quasiparticle interference spectrum. *EPL*, 106(2):27006, 2014.

[12] M. Sigrist, D. F. Agterberg, M. H. Fischer, J. Goryo, F. Loder, S. H. Rhim, D. Maruyama, Y. Yanase, T. Yoshida, and S. J. Youn. Superconductors with staggered non-centrosymmetricity. *J. Phys. Soc. Jpn.*, 83(6):061014, 2014.

[13] M. H. Fischer and J. Goryo. Symmetry and gap classification of non-symmorphic SrPtAs. *J. Phys. Soc. Jpn.*, 84(5):054705, 2015.

[14] J. Goryo, Y. Imai, W. B. Rui, M. Sigrist, and A. P. Schnyder. Surface magnetism in a chiral d-wave superconductor with hexagonal symmetry. *Phys. Rev. B*, 96(14):140502, 2017.

[15] S. Sumita and Y. Yanase. Unconventional superconducting gap structure protected by space group symmetry. *Phys. Rev. B*, 97(13):134512, 2018.

[16] S. Kakiya, K. Kudo, Y. Nishikubo, K. Oku, E. Nishibori, H. Sawa, T. Yamamoto, T. Nozaka, and M. Nohara. Superconductivity at 38 k in iron-based compound with platinum–arsenide layers $\mathrm{Ca_{10}(Pt_4As_8)(Fe_{2-x}Pt_xAs_2)_5}$. *J. Phys. Soc. Jpn.*, 80(9):093704, 2011.

[17] N. Ni, J. M. Allred, B. C. Chan, and R. J. Cava. High Tc electron doped $\mathrm{Ca_{10}(Pt_3As_8)(Fe_2As_2)_5}$ and $\mathrm{Ca_{10}(Pt_4As_8)(Fe_2As_2)_5}$ superconductors with skutterudite intermediary layers. *PNAS*, 108(45):E1019–E1026, 2011.

[18] K. Cho, M. A. Tanatar, H. Kim, W. E. Straszheim, N. Ni, R. J. Cava, and R. Prozorov. Doping-dependent superconducting gap anisotropy in the two-dimensional pnictide $\mathrm{Ca_{10}(Pt_3As_8)[(Fe_{1-x}Pt_x)_2As_2]_5}$. *Phys. Rev. B, Condens. Matter Mater. Phys.*, 85(2):020504, 2012.

[19] M. Neupane, C. Liu, S. Y. Xu, Y. J. Wang, N. Ni, J. M. Allred, L. A. Wray, N. Alidoust, H. Lin, R. S. Markiewicz, et al. Fermi-surface topology and low-lying electronic structure of the iron-based superconductor $\mathrm{Ca_{10}(Pt_3As_8)(Fe_2As_2)_5}$. *Phys. Rev. B*, 85(9):094510, 2012.

[20] S. V. Shulga and S. L. Drechsler. Low temperature value of the upper critical field h c 2 (0) of isotropic single band metals. *J. Low Temp. Phys.*, 129:93–102, 2002.

[21] G. Wenski and A. Mewis. Trigonal-planar koordiniertes platin: Darstellung und struktur von $\mathrm{SrPtAs(Sb), BaPtP(As, Sb)}$, $\mathrm{SrPt_xP_{2-x}}$, $\mathrm{SrPt_xAs_{0,90}}$ und $\mathrm{BaPt_xAs_{0,90}}$. *Z. Anorg. Allg. Chem.*, 535(4):110–122, 1986.

[22] K. Kudo, T. Takeuchi, H. Ota, Y. Saito, S. Y. Ayukawa, K. Fujimura, and M. Nohara. Superconductivity in hexagonal BaPtAs: SrPtSb- and YPtAs-type structures with ordered honeycomb network. *J. Phys. Soc. Jpn.*, 87(7):073708, 2018.

[23] G. Wenski and A. Mewis. REPtX compounds with structures related to $\mathrm{AIB_2}$- $\mathrm{and\,MgAgAs-type}$ ($\mathrm{RE = Y}$, rare earth element; $\mathrm{X = P, As, Sb}$). *Z. Kristallogr. Cryst. Mater.*, 176(1-2):125–134, 1986.

[24] M. Kuss, G. Wenski, A. Mewis, and H. U. Schuster. Magnetische eigenschaften von SEPtX-verbindungen (SE= seltenerdelement, $\mathrm{X = P, As}$). *Z. Anorg. Allg. Chem.*, 553(10):156–162, 1987.

[25] D. Rossi, R. Marazza, D. Mazzone, and R. Ferro. REInCd, REAsPd and RESbPt compounds (RE = rare earth element). *J. Less-Common Met.*, 78(1):P1–P5, 1981.

[26] K. H. J. Buschow, F. R. Boer, et al. *Physics of magnetism and magnetic materials*, volume 7. Springer, 2003.

[27] M. De and S. K. De. Magnetic and magneto-optical properties of NdX $(\mathrm{X{=}\,P, As, Sb, Bi})$. *J. Phys.: Condens. Matter.*, 11(32):6277, 1999.

[28] V. I. Ozhogin, V. G. Shapiro, and A. I. Kikoin. Table of physical data. *by AI Kikoin, M., Atomizdat*, pages 600–633, 1976.

[29] P. Bak and P. Lindgard. Magnetic properties of Nd-group V compounds. *J. Phys. C: Solid State Phys.*, 6(24):3774, 1973.

[30] G. Busch, O. Marinček, A. Menth, and O. Vogt. Magnetic properties of ordering rare-earth antimonides. *Phys. Lett.*, 14(4):262–264, 1965.

[31] Bruker AXS. *APEX3, version 2016.5–0.* Bruker AXS, Madison, Wisconsin, 2016.

[32] G. M. Sheldrick. XPREP, version 2008/2. bruker-axs, 2008.

[33] G. M. Sheldrick. Programs for crystallographic solution and refinement. *Acta Crystallogr. A*, 64:112–122, 2008.

[34] A Coelho. TOPAS-academic, version 4.1, coelho software, 2007.

[35] STOE & Cie GmbH. *WINXPOW, Version 3.0.2.5.* STOE & Cie GmbH, Darmstadt, Germany, 2011. Software.

[36] Carl Zeiss Microscopy Ltd. *SMARTSEM, Version 5.07 Beta.* Carl Zeiss Microscopy Ltd., Cambridge, UK, 2014. Software.

[37] Bruker Nano GmbH. *QUANTAX 200, Version 1.9.4.3448.* Bruker Nano GmbH, Berlin, Germany, 2013. Software.

[38] MPMS XL. with multivu software. *Quantum Design, Inc.: San Diego, CA.*, 7.

Chapter 3

Synthesis, Crystal Structure and Properties of the Plumbides *AE*AuPb (*AE* = Ca, Sr, Ba)

Peiqi Chen, Dirk Johrendt*

Accepted in ***Z. Naturforsch. B****, 2025*
DOI: 10.1515/znb-2025-0057

3.1 Abstract

The intermetallic compounds *AE*AuPb (*AE* = Ca, Sr, Ba) were synthesized from the elements and structurally characterized as isopointal to the orthorhombic KHg_2-type structure (*Imma*, CaAuPb: $a = 4.8068(9)$, $b = 7.3795(5)$, $c = 8.327(1)$ Å; SrAuPb: $a = 4.9038(2)$, $b = 7.7977(3)$, $c = 8.4651(4)$ Å; BaAuPb: $a = 5.0266(4)$, $b = 8.1804(4)$, $c = 8.6834(8)$ Å). Single-crystal X-ray diffraction of SrAuPb revealed mixed Au/Pb site occupancy, while isotypic CaAuPb and BaAuPb structures were obtained from powder X-ray diffraction. All three compounds exhibit metallic conductivity and weak, temperature-independent Pauli paramagnetism, consistent with nonmagnetic, delocalized electronic states. These results identify the *AE*AuPb series as nonmagnetic Au–Pb plumbides with mixed site occupancy and provide a basis for further exploration of spin–orbit coupling effects arising from the presence of gold and lead.

Keywords: ternary plumbides; KHg_2-type; mixed occupancy; Pauli-paramagnetism

3.2 Introduction

Equiatomic ternary intermetallic compounds *RTX* (*R* = alkaline earth, rare earth; *T* = transition metal; *X* = main group element of the *p* block) have been extensively studied due to their diverse crystal structures, rich physical properties, and complex bonding scenarios.[1–9] Among them, compounds that crystallize with structures derived from the AlB_2-type structure [10] and its ordered variants have drawn considerable interest, especially after the discovery of superconductivity with T_c = 39 K in MgB_2[11] with similar honeycomb-like layers. Their crystal chemistry has been extensively described in different articles alongside their physical properties.[12]

The series *RE*AuPb (*RE*= rare earth) has been reported to crystallize in the hexagonal $CaIn_2$-type structure (space group $P6_3/mmc$) up to *RE* = Sm. Compounds with the heavier rare earth elements Gd-Er and Y instead adopt the cubic MgAgAs-type structure.[13] A pronounced discontinuity in the unit cell volume is observed at the transition from the $CaIn_2$ type to the MgAgAs-type structure. An exception within the series is EuAuPb, which crystallizes in the orthorhombic KHg_2-type structure (space group *Imma*), thereby deviating from the general trend in the *RE*AuPb compounds.

Recently, EuAuBi and SrAuBi have emerged as layered polar semimetals exhibiting both superconductivity and strong spin-orbit coupling. EuAuBi exhibits a magnetic transition at 4 K and a superconducting transition at 2.2 K, accompanied by strong Rashba-type spin–orbit coupling.[14] Similarly, SrAuBi displays superconductivity at 4.2 K, along with ferroelectric-like lattice distortions.[15] Band calculations reveal Rashba-type spin splitting and symmetry-protected Dirac points near the Fermi level, potentially indicating unconventional superconductivity associated with surface states.

Despite a broad research landscape of equiatomic *RE*-based plumbides, little is known about analogous compounds with alkaline earth elements. Herein, we explore the compounds (Ca, Sr, Ba)AuPb, which have not been reported so far. Using single-crystal and powder X-ray diffraction, we demonstrate that these compounds are isopointal to the KHg_2 type, consistent with previously reported EuAuPb.[16]

3.3 Experimental

3.3.1 Synthesis

Samples of *AE*AuPb (*AE*= Ca, Sr, Ba) were synthesized via solid-state reaction starting from the elements. Calcium (Sigma Aldrich, 99.99%), strontium (Sigma Aldrich, 99.95%), barium (Sigma Aldrich, 99.99%), gold (Agosi, 99.99%), and lead (ThermoFisher, 99.999%) were employed as sublimed ingots. For SrAuPb, a weight ratio of Sr:Au:Pb = 1.1:1:1 was utilised, with an additional 10% of the nominal composition to ensure purity and prevent side phase formation. For CaAuPb and BaAuPb, stoichiometric 1:1:1 molar ratios were applied. The element mixtures were filled in alumina crucibles, sealed in silica ampules under an argon atmosphere, and heated to 800-900°C in tube furnaces. Optimised heating procedures yielded black polycrystalline samples. SrAuPb is air-stable, while CaAuPb and BaAuPb are highly air-sensitive. The solid-state synthesis from the elements proved to be effective, while attempts using flux methods were unsuccessful in producing phase-pure samples.

3.3.2 X-ray powder and Single Crystal Data

X-ray powder diffraction patterns were recorded using a Stadi-P diffractometer (STOE & Cie GmbH, Darmstadt, Germany, Ag$K\alpha$ radiation, $\lambda = 0.56\,\text{Å}$). Rietveld refinements based on structure models from single-crystal diffraction were performed using the TOPAS software.[17] Single-crystal X-ray data for SrAuPb were collected on a Bruker D8 Quest diffractometer with a Mo$K\alpha$ microfocus source, Göbel mirror optics, and a Photon II detector. APEX3 [18] was used for data reduction and absorption correction. Space group determination was carried out with XPREP.[19] based on systematically absent reflections. SHELX-97 [20] was used for the structure solution and refinement.

3.3.3 Physical Properties Measurement

Magnetization isotherms and susceptibility measurements were measured using a Physical Property Measurement System (PPMS, Quantum Design Inc.). The PPMS allowed for measurements with fields up to ± 50 KOe ($1\text{KOe} = 7.96 \times 10^4\,\text{A}\,\text{m}^{-1}$) and between temperatures of 1.9 K and 300 K. Data were collected with the MULTIVU software package. [21] Electrical resistivity measurements were performed with PPMS equipped with a resistivity option. The samples were compacted into pellets and contacted using a four-point Van-der-Pauw press contact.

3.4 Results

3.4.1 Crystal chemistry

Since X-ray diffraction cannot distinguish between Au and Pb atoms, both atom types were distributed on the $8h$ site of the space group *Imma* each with half occupancy. This mixed occupancy was consistently observed and refined with acceptable reliability factors, confirming the Au/Pb site disorder. The results of the X-ray crystal structure determination of SrAuPb are summarized in Table 3.1. SrAuPb is thus isotypic to EuAuPb,[16] the only compound in the *RE*AuPb series that crystallizes in the KHg_2 type. Poor crystal quality, notably twinning and weak scattering, did not allow single-crystal X-ray structure determinations of CaAuPb and BaAuPb; instead, their structures were determined from powder using Rietveld refinements with the single-crystal data of SrAuPb as starting parameters. The results for *AE*AuPb (*AE*= Ca, Ba) are presented in Table 3.2 and Figure 3.1. The lattice parameters expand according to the increasing cation sizes (Ca $<$ Eu $\approx$ Sr $<$ Ba). Table 3.3 shows the atomic positions and equivalent displacement parameters.

*AE*AuPb (*AE*= Ca, Sr, Ba) crystallize similar to the KHg_2-type structure (space group *Imma*),[22] an orthohombically distorted variant of the well-known AlB_2 type.[10] The KHg_2 structure [23] is also referred to as $CeCu_2$ type[22] in the literature. The Au/Pb atoms form puckered layers of orthohombically distorted hexagons. The Au/Pb–Au/Pb distances range from 2.840(1) Å to 3.244(1) Å (Table 3.4), which is close to the sum of the covalent radii of 2.82 Å for gold and lead.[24] The Figures 3.3a and 3.3b show that the

Table 3.1: Crystallographic data of SrAuPb.

Formula	SrAuPb
Space Group	*Imma* (No. 74)
a / Å	4.9038(2)
b / Å	7.7977(3)
c / Å	8.4651(4)
V_{cell} / Å^3	323.69(2)
Z	4
$\rho_{\text{X-ray}}$ / g cm^{-3}	10.09
μ/ mm^{-1}	113.2
θ range / deg	3.552- 30.461
Reflections measured	3714
Independent reflections	291
Parameters	12
R_σ	0.0374
R_{int}	0.0742
$R_1(F^2 > 2\sigma(F^2))$; all data	0.0537; 0.0537
$wR_2(F^2 > 2\sigma(F^2))$; all data	0.1402; 0.1402
GooF	1.175
$\Delta\rho_{max;min}$ / eÅ^{-3}	17.18; -2.89

Table 3.2: Crystallographic data for the refinement of CaAuPb and BaAuPb.

Formula	CaAuPb	BaAuPb
formula mass / g mol $^{-1}$	444.244	541.496
space group	*Imma* (No. 74)	*Imma* (No. 74)
a / Å	4.8068(9)	5.0267(4)
b / Å	7.3795(5)	8.1804(4)
c / Å	8.3267(16)	8.6834(8)
V_{cell} / Å^3	295.36(8)	357.06(5)
Z	4	4
$\rho_{\mathrm{X\text{-}ray}}$ / g cm^{-3}	9.991	10.073
R_{exp} ; R_{Bragg}	25.859; 4.540	17.885; 2.846
R_{p} ; R_{wp}	8.063; 6.132	6.576; 5.010
GooF	1.208	1.775

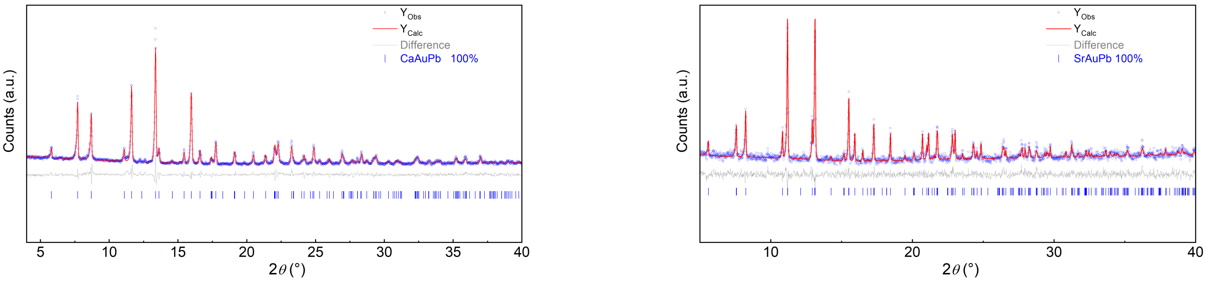

(a) CaAuPb

(b) SrAuPb

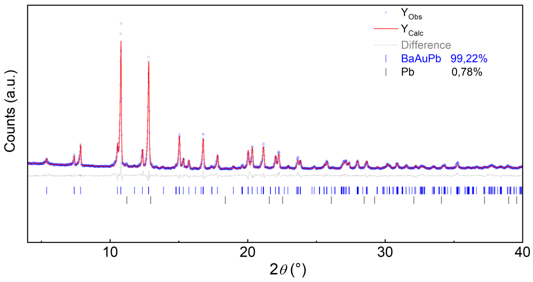

(c) BaAuPb

Figure 3.1: X-Ray powder patterns (blue) with Rietveld fit (red) and difference plot (grey) of AEAuPb (AE = Ca, Sr, Ba)

Table 3.3: Atomic coordinates, equivalent displacement parameters (Å^2) of AEAuPb (AE = Ca, Sr, Ba). U_{eq} is defined as one third of the trace of the orthogonalized U_{ij} tensor; for atoms refined isotropically, U_{eq} is equal to U_{iso} ($B_{\mathrm{iso}} = 8\pi^2 U_{\mathrm{iso}}$).

Atom	Wyckoff	x	y	z	U_{eq} / B_{iso}
CaAuPb					
Ca	4e	0	1/4	0.48(2)	$B_{\mathrm{iso}} = 3.1(4)$
Au/Pb	8h	0	0.037(1)	0.1648(8)	$B_{\mathrm{iso}} = 0.75(9)$
SrAuPb					
Sr	4e	0	1/4	0.5344(4)	$U_{\mathrm{eq}} = 0.0134(7)$
Au/Pb	8h	0	0.0419(1)	0.16533(9)	$U_{\mathrm{eq}} = 0.0135(5)$
BaAuPb					
Ba	4e	0	1/4	0.537(2)	$B_{\mathrm{iso}} = 1.26(12)$
Au/Pb	8h	0	0.037(1)	0.1656(9)	$B_{\mathrm{iso}} = 1.07(6)$

Table 3.4: Selected distances in *AE*AuPb (*AE* = Ca, Sr, Ba).

atoms	distance / Å	atoms	distance/ Å
Au/Pb—Au/Pb	2.791(5)	Au/Pb—Au/Pb	2.791(5)
Au/Pb—Au/Pb	2.800(1)	Au/Pb—Au/Pb	3.133(1)
Au/Pb—Ca	3.09(15)	Au/Pb—Ca	3.13(7)
Au/Pb—Ca	3.13(7)	Au/Pb—Ca	3.54(8)
Au/Pb—Ca	3.54(8)	Au/Pb—Ca	3.61(15)
Au/Pb—Au/Pb	2.840(1)	Au/Pb—Au/Pb	2.840(1)
Au/Pb—Au/Pb	2.875(1)	Au/Pb—Au/Pb	3.244(1)
Au/Pb—Sr	3.3916(17)	Au/Pb—Sr	3.412(2)
Au/Pb—Sr	3.521(3)	Au/Pb—Sr	3.5246(11)
Au/Pb—Sr	3.5246(11)	Au/Pb—Sr	3.3916(17)
Au/Pb—Au/Pb	2.896(8)	Au/Pb—Au/Pb	2.896(8)
Au/Pb—Au/Pb	2.963(15)	Au/Pb—Au/Pb	3.500(17)
Au/Pb—Ba	3.529(11)	Au/Pb—Ba	3.529(11)
Au/Pb—Ba	3.616(9)	Au/Pb—Ba	3.616(9)
Au/Pb—Ba	3.667(19)	Au/Pb—Ba	3.489(17)

mixed-occupancy Au/Pb atoms form honeycomb-like but puckered layers in the *ac* plane. In contrast to the nearly identical distances between atoms within and perpendicular to the hexagons in KHg_2, we observe that the bonds within the Au/Pb hexagons of *AE*AuPb are significantly shorter (14 %) than those perpendicular to the layers. This indicates that the *AE*AuPb compounds possess a more two-dimensional character, whereas KHg_2 exhibits a three-dimensional network. Consequently, we describe the *AE*AuPb compounds as isopointal [25] and not isotypic to KHg_2.

As shown in Figure 3.2, the structure arises through a symmetry descent from the AlB_2 prototype (space group $P6/mmm$) via the intermediate subgroup *Cmmm* to *Imma*, according to the Bärnighausen formalism. [26] In *AE*AuPb, the transition-metal site of the parent KHg_2-type structure is mixed-occupied by Au and Pb, and the alkaline earth atoms reside in channels formed within the Au–Pb network (Figure 3.3).

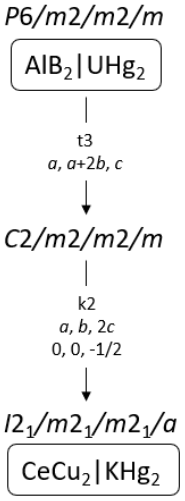

Figure 3.2: Crystal chemical relationship between the structures of AlB_2 and KHg_2. The space groups, the group-subgroup relationships, and the occupancy of the different Wyckoff sites are indicated.

A structure isotypic to EuAuPb was expected for SrAuPb due to similar radii of Sr^{2+} (1.17 Å) and Eu^{2+} (1.18 Å). [27] Surprisingly, Ca^{2+} (1.0 Å) and Ba^{2+} (1.35 Å) also form the KHg_2 type, deviating from the expected MgAgAs type for CaAuPb and ZrBeSi type for BaAuPb. This suggests that atomic sizes alone are insufficient, and electronic factors likely play an important role.

Although individual Au–Au, Au–Pb, and Pb–Pb contacts cannot be distinguished in SrAuPb, the observed Au/Pb–Au/Pb interlayer distances fall within the same range as reported for ordered *R*–Au–Pb compounds. [13] The nature of the less electronegative element have been discussed to influence the *s* electron density at the more electronegative gold atoms in Ref. [28]. As previously discussed for other *R*–Au–Pb plumbides, [13] the formation of different structural types in this system results from a complex interplay between electronic and geometrical factors. For comparison, the compound Ca_2Au_2Pb, [29] although crystallizing in a different structure type, provides a useful benchmark for bond lengths in Au–Pb-based intermetallics. The shortest contacts in Ca_2Au_2Pb include Au-Au 2.793(1)Å, Ca-Au 3.005(3)Å, Au-Pb 3.188(1)Å, Ca-Pb 3.535(1)Å and Ca-Ca 3.825(1)Å. These values support the interpretation of covalent and metallic bonding within the disordered (Au/Pb) networks and validate the bonding picture proposed for the *AE*AuPb (*AE* = Ca, Sr, Ba) compounds studied here.

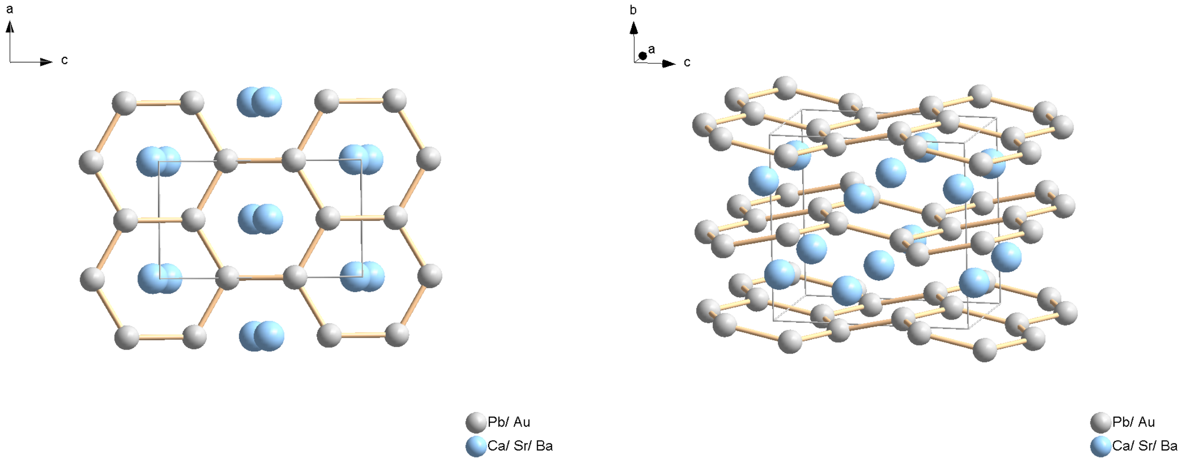

(a) (b)

Figure 3.3: Crystal structure of *AE*AuPb (*AE* = Ca, Sr, Ba)

3.4.2 Magnetic Susceptibility

The temperature-dependent magnetic susceptibilities of *AE*AuPb (*AE*= Ca, Sr, Ba) are shown in Figure 3.4. All three compounds show low magnetic moments and do not follow the Curie-Weiss law. This is expected, as none of the constituent elements contain unpaired electrons, and the resulting compounds are thus either diamagnetic or weakly Pauli-paramagnetic. SrAuPb and BaAuPb show weak paramagnetism, which does not change significantly with temperature. The susceptibility at 300 K ranges between $\chi = 0.10(5) \times 10^{-3}$ and $\chi = 0.09(2) \times 10^{-3}$ emu mol^{-1}. CaAuPb displays a slightly higher value of $\chi = 0.17(7) \times 10^{-3}$ emu mol^{-1} which increases at low temperatures. All samples exhibit at least 99% phase purity and are sufficiently homogeneous for reliable magnetic characterization. However, minor amounts of magnetic impurities give rise to an increase in susceptibility at low temperatures (Curie tail) in CaAuPb.

The magnetic susceptibility of EuAuPb has been reported in the literature. [16, 30] Measurements revealed Curie-Weiss paramagnetism with an effective magnetic moment of 6.8 μ_B/Eu and antiferromagnetic ordering at 7 K,[2] consistent with most divalent europium compounds (EuTX, T = transition metal, X = p element). [31–34] The comparison highlights the distinct difference between *AE*AuPb (*AE*= Ca, Sr, Ba), which are Pauli-paramagnetic, and EuAuPb, which shows strong localized $4f$ magnetism. Europium in

EuAuPb predominantly exists in the 2+ oxidation state, which provides a basis for substituting Eu with Sr in SrAuPb, as both elements have comparable atomic radii and typically exhibit a divalent oxidation state in intermetallic compounds.

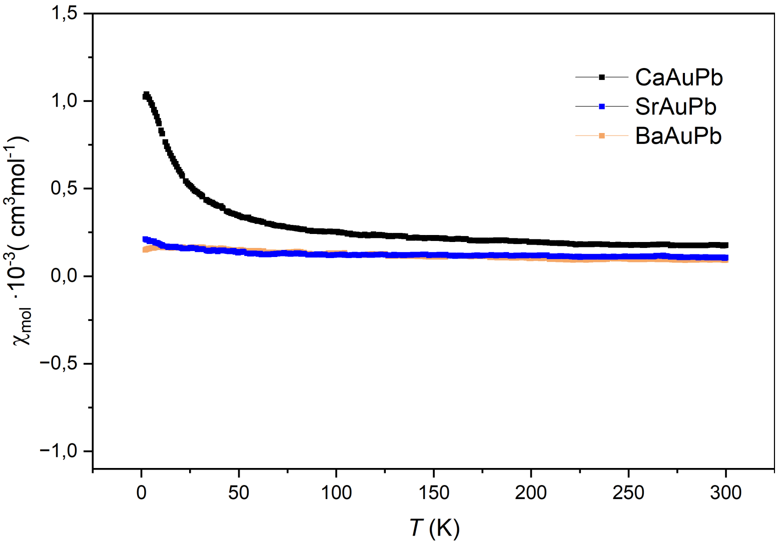

Figure 3.4: Susceptibility of *AE*AuPb (*AE* = Ca, Sr, Ba) for the temperature range 2.9-300 K.

3.4.3 Electrical Conductivity

The temperature-dependent electrical resistivity of *AE*AuPb (*AE* = Ca, Sr, Ba) is presented in Figure 3.5. All resistivity measurements revealed metallic behavior over the temperature range investigated. The resistivities decrease linearly from room temperature to approximately 7 K and show sharp drops near 6 K, which is the onset of superconductivity of a tiny lead impurity. The *AE*AuPb compounds can be classified as reasonably good metallic conductors. However, the irregular shape and polycrystalline nature of the samples, combined with grain boundary effects, prevented the determination absolute values.

3.5 Conclusion

The intermetallic compounds *AE*AuPb can be synthesized from the elements and crystallize isotypically in the orthorhombic KHg_2 type (space group *Imma*, No. 74). Single-crystal data revealed mixed Au/Pb occupancy in SrAuPb, while CaAuPb and BaAuPb structures were obtained from powder data. All three compounds exhibit metallic conductivity and weak, temperature-independent Pauli paramagnetism, consistent with nonmagnetic, delocalized electronic states. Comparison with the isostructural compound EuAuPb, which displays antiferromagnetic ordering and localized Eu^{2+} moments, supports structural and electronic compatibility between Eu^{2+} and Sr^{2+} cations. Our findings identify

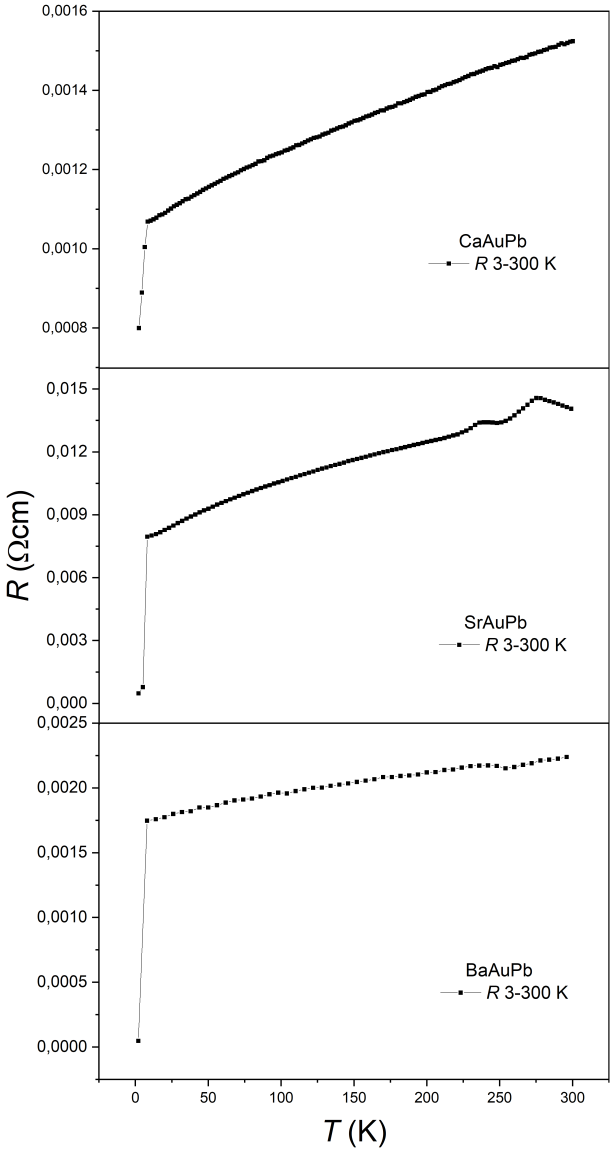

Figure 3.5: DC resistivity of AEAuPb (AE = Ca, Sr, Ba).

the *AE*AuPb (*AE* = Ca, Sr, Ba) series as examples of KHg_2 type Au-Pb plumbides featuring mixed Au/Pb site occupancy and nonmagnetic ground states. Further investigations are needed to determine the extent to which the heavy elements gold and lead may induce the formation of electronically non-trivial materials through effects of spin-orbit coupling.

Supporting information

CSD-2481650 (BaAuPb), CSD-2481651 (CaAuPb), and CSD-2481652 (SrAuPb) contain the supplementary crystallographic data for this paper. These data can be obtained free of charge via www.ccdc.cam.ac.uk/conts/retrieving.html.

References

[1] E. Parthé, L. Gelato, B. Chabot, M. Penzo, K. Cenzual, and R. Gladyshevskii. *TYPIX standardized data and crystal chemical characterization of inorganic structure types.* Springer Science & Business Media, Heidelberg, 2013.

[2] A. Szytula. *Handbook of crystal structures and magnetic properties of rare earth intermetallics.* CRC press, Boca Raton, 2020.

[3] M. L. Fornasini and F. Merlo. Equiatomic ternary phases formed by alkaline earths and rare earths. *J. Alloys Compd.*, 219(1-2):63–68, 1995.

[4] A. Szytuła. Structural aspects of chemical bonding in RTX intermetallic compounds. *Croat. Chem. Acta*, 72(2-3):171–186, 1999.

[5] S. Gupta and K. G. Suresh. Review on magnetic and related properties of RTX compounds. *J. Alloys Compd.*, 618:562–606, 2015.

[6] Q. S. Lin and G. J. Miller. Electron-poor polar intermetallics: complex structures, novel clusters, and intriguing bonding with pronounced electron delocalization. *Acc. Chem. Res.*, 51(1):49–58, 2018.

[7] P. Villars and K. Cenzual. Crystal structure database for inorganic compounds. *ASM Int.*, pages 2017–2018, 2012.

[8] M. Giovannini, I. Curlik, R. Freccero, P. Solokha, M. Reiffers, and J. Sereni. Crystal structure and magnetism of noncentrosymmetric Eu_2Pd_2Sn. *Inorg. Chem.*, 60(11):8085–8092, 2021.

[9] J. Chen, M. B Gamża, J. Banda, K. Murphy, J. Tarrant, M. Brando, and F. M. Grosche. Unconventional bulk superconductivity in YFe_2Ge_2 single crystals. *Phys. Rev. Lett.*, 125(23):237002, 2020.

[10] R. D. Hoffmann and R. Pöttgen. AlB_2-related intermetallic compounds–a comprehensive view based on group-subgroup relations. *Kristallogr. – Cryst. Mater.*, 216(3):127–145, 2001.

[11] J. Nagamatsu, N. Nakagawa, T. Muranaka, Y. Zenitani, and J. Akimitsu. Superconductivity at 39 k in magnesium diboride. *Nat.*, 410(6824):63–64, 2001.

[12] L. Eyring, K. A. Gschneidner, and G. H. Lander. *Handbook on the physics and chemistry of rare earths*, volume 32. Elsevier, North-Holland, 2002.

[13] R. Marazza, D. Rossi, and R. Ferro. On the ternary rare earth alloys: RAuPb compounds. *J. Less-Common Met.*, 138(2):189–193, 1988.

[14] H. Takahashi, K. Akiba, M. Takahashi, A. H. Mayo, M. Ochi, T. C. Kobayashi, and S. Ishiwata. Superconductivity in a magnetic rashba semimetal EuAuBi. *J. Phys. Soc. Jpn.*, 92(1):013701, 2023.

[15] H. Takahashi, T. Sasaki, A. Nakano, K. Akiba, M. Takahashi, A. H. Mayo, M. Onose, T. C. Kobayashi, and S. Ishiwata. Superconductivity in a ferroelectric-like topological semimetal SrAuBi. *npj Quantum Mater.*, 8(1):77, 2023.

[16] P. E. Arpe. Synthese und strukturchemische untersuchungen an ternären plumbiden des ytterbiums. *Universität Münster: Staatsexamensarbeit*, 1998.

[17] A Coelho. Topas-academic, version 4.1, coelho software, 2007.

[18] Bruker AXS. *Apex3, version 2016.5–0.* Bruker AXS, Madison, Wisconsin, 2016.

[19] G. M. Sheldrick. Xprep, version 2008/2. bruker-axs, 2008.

[20] G. M. Sheldrick. Programs for crystallographic solution and refinement. *Acta Crystallogr. A*, 64:112–122, 2008.

[21] MPMS XL. with multivu software. *Quantum Design, Inc.: San Diego, CA.*, 7.

[22] A. C. Larson and D. T. Cromer. The crystal structure of $CeCu_2$. *Acta Crystallogr.*, 14(1):73–74, 1961.

[23] E. J. Duwell and N. C. Baenziger. The crystal structures of KHg and KHg_2. *Acta Crystallogr.*, 8(11):705–710, 1955.

[24] B. Cordero, V. Gómez, A. E. Platero-Prats, M. Revés, J. Echeverría, E. Cremades, F. Barragán, and S. Alvarez. Covalent radii revisited. *Dalton Trans.*, (21):2832–2838, 2008.

[25] E. Parthe. The need to standardize structures to recognize structural relationships. *Acta Crystallogr., Sect. A: Found. Crystallogr.*, 43(a1):C301, 1987.

[26] H. Barnighausen. Group-subgroup relations between space groups: a useful tool in crystal chemistry. *MATCH Commun. Math. Comput. Chem.*, 9:139–175, 1980.

[27] R. D. Shannon and C. T. Prewitt. Effective ionic radii in oxides and fluorides. *Struct. Sci.*, 25(5):925–946, 1969.

[28] R. D. Hoffmann, R. Pöttgen, D. Kußmann, D. Niepmann, H. Trill, and B. D. Mosel. Transition metal–tin ordering in SrPtSn, SrAuSn and BaAuSn and ^{119}Sn mössbauer spectroscopy of CaPdSn, CaPtSn and SrAuSn. *Solid State Sci.*, 4(4):481–487, 2002.

[29] M. L. Fornasini, F. Merlo, and M. Pani. Crystal structure of calcium gold plumbide (2/2/1), Ca_2Au_2Pb. *Z. Kristallogr. N. Cryst. Struct.*, 216(1-4):23–23, 2001.

[30] R. Pöttgen and D. Johrendt. Equiatomic intermetallic europium compounds: syntheses, crystal chemistry, chemical bonding, and physical properties. *Chem. Mater.*, 12(4):875–897, 2000.

[31] C. Tomuschat and H. U. Schuster. Magnetic properties of the compound series EuBX with B = element of the first subgroup and X = element of the fifth main group. *Z. Anorg. Allg. Chem.*, 518(11):161–167, 1984.

[32] N. Lossau, H. Kierspel, J. Langen, W. Schlabitz, D. Wohlleben, A. Mewis, and Ch. Sauer. EuPtP: a new mixed valent europium-system. *Z. Phys. B: Condens. Matter*, 74:227–232, 1989.

[33] C. Lux, A. Mewis, N. Lossau, G. Michels, and W. Schlabitz. EuPtP, $\mathrm{Eu_{1-x}Gd_xPtP}$, and $\mathrm{Eu_{0.5}Sr_{0.5}PtP}$: Structures and intermediate valence. *Z. Anorg. Allg. Chem.*, 593(27):169, 1991.

[34] C. Lux, A. Mewis, S. Junk, A. Gruetz, and G. Michels. Kristallstrukturen und eigenschaften neuer ternärer iridiumphosphide. *J. Alloys Compd.*, 200(1-2):135–139, 1993.

Chapter 4

Crystal structures of new ternary compounds EuPtPb and SrPtPb

4.1 Abstract

The ternary intermetallic compounds SrPtPb and EuPtPb were synthesized via solid-state reaction methods, and their structures were confirmed to crystallize in the orthorhombic TiNiSi-type structure (space group *Pnma*) with complete ordering of platinum and lead atoms. X-ray powder diffraction indicated the presence of minor secondary phases, particularly in EuPtPb. SrPtPb exhibits metallic conductivity, and magnetic susceptibility measurements suggest weak, temperature-independent paramagnetism, deviating from Curie–Weiss behavior. A resistivity anomaly was observed near 275 K in SrPtPb, without hysteresis, potentially indicating a subtle phase instability. The anomalous magnetic behavior, downward curvature in χ^{-1} vs. T, and small effective moment may be attributed to crystal electric field effects, Pauli paramagnetism, or Kondo-like compensation. Due to impurity phases, no definitive physical property analysis was conducted for EuPtPb, although structural comparison with other *RE*PdPb analogues suggests a similar electronic configuration.

4.2 Introduction

In recent years, increasing interest has emerged in studying materials that simultaneously host Dirac nodal arcs and superconductivity, as such systems hold promise for realizing exotic surface phenomena associated with topological superconductivity [1–4]. A viable route toward engineering topological superconductors is to search for intrinsic superconductivity within topological materials—either in stoichiometric compounds at ambient pressure, under high pressure, or via chemical doping. Several such compounds have been discovered, including $Cu_xBi_2Se_3$ [5–7], Au_2Pb [8, 9], $PbTaSe_2$ [10], $\beta-PdBi_2$ [11, 12], S-doped $MoTe_2$ [13], $PtSn_4$ [14], $PtPb_4$ [15], etc., and in some cases, experimental evidence of Majorana zero modes has been claimed. $PtPb_4$ is a superconducting intermetallic compound with

Tc $\approx$ 2.8K.

Recent work [16] has introduced a distinctive isoelectronic family of intermetallic superconductors $BaPb_3$, $Ba_{0.89}Sr_{0.11}Pb_3$, $Ba_{0.5}Sr_{0.5}Pb_3$ and $SrPb_3$.These compounds, based on the stacking of Pb planes, form an intermetallic series with a rare hexagonal-to-cubic structural perovskite-like progression, which is unusual in metallic systems. They are moderate coupling superconductors, and calculations show that Pb primarily contributes to the electronic density of states at the Fermi level. Variations in Pb stacking appear to have only a minor influence on their superconducting behavior.

Parallel to these developments in superconductivity, significant attention has been directed toward the interactions between rare earth metals, transition metals, and lead, due to their rich structural and magnetic complexity [17].

For instance, Ce_2M_2Pb ($M=$ Au, Pt) crystallizes in Mo_2FeB_2-type (ordered U_3Si_2) structure [18], while Yb_2Pt_2Pb crystallizes in the Er_2Au_2Sn structure type (space group $P4_2/mnm$, No.136) [19],a ternary ordered version of the Zr_3Al_2 type[20]. Compounds such as LaPtPb and CePtPb adopt the Fe_2P structure type as described in Ref. [21]. A systematic investigation of RE_2Pt_2Pb ($RE=$ Y, La, Ce, Pr, Nd, Sm, Gd, Tb, Dy, Er, Tm, and Lu), and *RE*PtPb ($RE=$ La, Ce, Pr, Nd, Sm) has also been reported in the Ref.[22]. These *RE*–Pt–Pb systems span a wide range of crystal structures, including YbPb (CuAu type) [23] and $YbPt_2$ (cubic Laves phase $MgCu_2$) [24]. In the $Ce_{1-x}Pb_xPt_2$ ($0 \leq x < 0.5$) series samples, increasing Pb substitution induces a transition from face-center-cubic sublattice $CePt_2$ ($MgCu_2$) phase to a superlattice structure of cubic C15b ($MgSnCu_4$ type), concurrently suppresses the antiferromagnetic ordering temperature below 0.35K for $x = 0.43$ [25].

Additionally, europium [26], cerium [27–29], and ytterbium [30] comprising compounds are worth mentioning due to the substantial investigation into their valence instabilities when searching for materials, ie. Ce^{III}/ Ce^{IV}, Eu^{II}/ Eu^{III}, and Yb^{II}/ Yb^{III}. Here, the empty ($4f^0$), half-filled ($4f^7$), and filled ($4f^{14}$) $4f$ shells of Ce^{4+}, Eu^{2+}, and Yb^{2+}, respectively, exhibit slightly enhanced stability due to their specific electron configuration. For instance, Eu-pnictides EuPtP [31, 32] and EuPdAs [33], crystallize in the hexagonal $NiIn_2$ structure. Both compounds undergo a first-to-second-order phase transition, and the volume shrinks according to the smaller ionic radius of Eu^{3+} compared to Eu^{2+} [31, 33]. However, the c-axis of the compounds shrinks exceeds that predicted by Vegard's law, while the a-axis even expands slightly with decreasing temperature.

Despite substantial interest in *RE*–Pt–Pb systems and Pb-containing intermetallics, to the best of our knowledge, no previous reports exist on *RE*PtPb compounds incorporating alkaline earth elements. Given the similar atomic radii of Sr and Eu, this gap presents a promising opportunity for exploration. In this work, we report the synthesis and characterization of two novel compounds, EuPtPb and SrPtPb. We examine their crystal structures and investigate their physical properties, with the goal of understanding how alkaline earth substitution may influence the structural and electronic behavior within this class of Pb-based intermetallics.

4.3 Experimental Detail

Synthesis. Starting materials for the preparation of the title compound SrPtPb and EuPtPb were ingots of the Sr (Sigma Aldrich, 99.95%) and Eu (Alfa Aesar, 99.90%) elements. Pt powder (Agosi, 99.95%) and Pb tear drops (ThermoFisher, 99.999%). Therefore, a fully ordered compound EuPtPb phase would not be formed, unlike in the case of SrPtPb. The samples with a total mass of about 0.3 g were prepared by solid state synthesis in high purity argon atmosphere. All compounds were re-melted several times to ensure homogeneity. X-ray diffraction patterns of the samples were recorded using a Stadi P powder diffractometer (STOE & Cie GmbH, Darmstadt, Germany) in Debye-Scherrer geometry with a Ge(111) monochromator and Ag $K\alpha$ radiation. The EuPtPb phase appears only for Eu contents of 0.95-1; higher or lower ratios do not yield this phase.

Single Crystal X-ray Diffraction. Crystals of sufficient quality for diffraction experiments were selected under dried paraffin oil and mounted the crystal on a micro mount (MiTeGen, America, 50μ sample aperture). Diffraction was collected on a Brucker D8 Quest diffractometer with a microfocus Mo $K\alpha$ X-ray source, Göbel mirror optics, and Photon II detector. the software package APEX3 [34] was used for data reduction and absorption correctia on. Space group determination was carried out with XPREP [35] based on systematically absent reflections. SHELX-97 [36] was used for the structure solution and refinement.

Powder X-ray Diffraction. The phase pure polystalline sample was ground and sealed in Hilgenberg capillaries to avoid hydrolysis. Data were collected on a Stadi P powder diffractometer (STOE & Cie GmbH, Darmstadt, Germany) equipped with a Mythen 1K detector (Dectris, Baden, Switzerland) in Debye-Scherrer geometry with a Ge(111) monochromator and Ag $K\alpha$ radiation. Rietveld refinement based on single crystal diffraction data was performed with TOPAS [37] software.

High Temperature Powder X-ray diffraction. Samples were filled in silica capillaries of 0.4 mm in diameter (Hilgenberg GmbH) sealed by grease to compensate increasing pressure. Diffraction data were collected under argon atmosphere with a Stoe Stadi P diffractometer (Mo Kα1, Ge(111)-monochromator, IP-PSD detector) equipped with a graphite furnace. The samples were heated with 2 K min˘1. The data were visualized with WINXPOW [38].

4.4 Results and Discussion

4.4.1 Crystal chemistry

Figure 4.1 and Figure 4.2 shows the X-ray powder diffraction patterns of SrPtPb and EuPtPb, respectively. The reflections can be indexed based on an orthorhombic unit cell with space group *Pnma*. The measured extinction conditions rule out *Imma* (which requires h+k+$l = 2n$) and are in accordance with *Pnma*: $hk0$: $h = 2n$, $0k0$: $k = 2n$, $h0l$: h+$l = 2n$, with reflections of h+k+l odd observed. The SrPtPb sample contains approximately 2.26%

$SrPt_2$ as a side phase, while the EuPtPb sample contains more than 15% secondary phases. The binary phases $SrPt_2$ and $EuPt_2$ are known to be thermodynamically stable under the synthesis conditions. Both SrPtPb and EuPtPb crystallize in the TiNiSi-type structure, isotypic with EuTX-type intermetallics [26], exhibiting complete lead and platinum ordering. Details regarding the data collection and structure refinement are summarized in Table 4.1 and the selected distances are provided in Table 4.3.

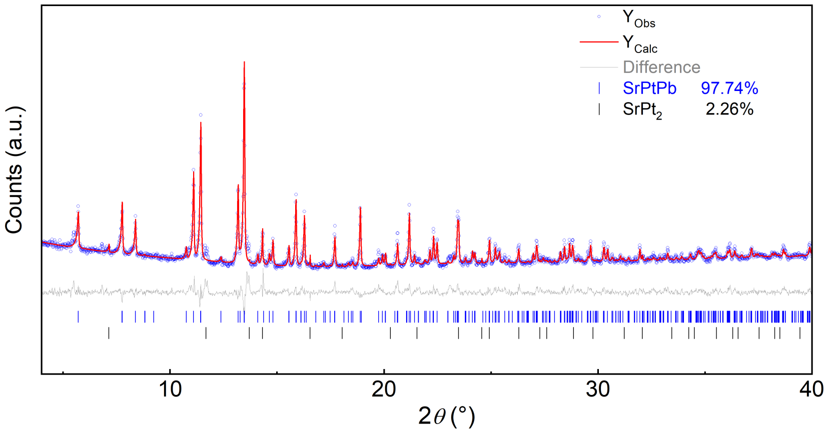

Figure 4.1: X-Ray powder pattern of SrPtPb (blue) with Rietveld fit (red) and difference plot(grey)

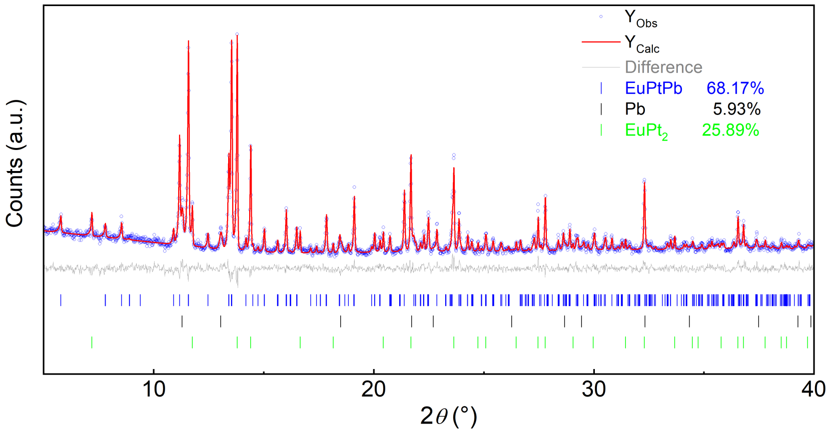

Figure 4.2: X-Ray powder pattern of EuPtPb (blue) with Rietveld fit (red) and difference plot(grey)

In both structures, each platinum atom is coordinated by four lead atoms in a strongly disordered tetrahedral geometry. The Pt-Pb distances rang from 2.7944(11) to 2.8990(11) Å in EuPtPb, and 2.8194(4) to 2.9117(4) Å in SrPtPb. These values are close to the sum of the covalent single bond radii [39, 40] for the lead and platinum (283 pm), and similar to those observed in the binary phases PtPb (NiAs-type structure) [41] and Pt_3Pb (Cu_3Au-type structure) [42], where the Pt-Pb distances are 281 and 287 pm, respectively. These

Table 4.1: Crystallographic data for the refinement of EuPtPb and SrPtPb.

Formula	EuPtPb	SrPtPb
Space Group	*Pnma* (No. 62)	*Pnma* (No. 62)
a / Å	7.5133(5)	7.6532(2)
b/ Å	4.7395(4)	4.77010(10)
c / Å	8.2443(6)	8.2709(2)
V_{cell} / Å^3	293.57(4)	301.942(12)
Z	4	4
$\rho_{\text{X-ray}}$ / g cm^{-3}	12.540	10.777
μ / mm^{-1}	125.488	119.096
Θ-range / °	3.669- 30.596	3.627- 30.518
reflections measured	5659	6896
independent reflections	499	509
parameters	19	20
R_σ	0.0564	0.0321
R_{int}	0.1171	0.0713
R_1 ($F^2>2\sigma$ (F^2)) / all	0.0437/0.0502	0.0214/0.0220
wR_2 ($F^2>2\sigma$ (F^2)) / all	0.0983/0.1011	0.0468/0.0470
GooF	1.064	1.052
$\Delta\rho_{\mathrm{max/min}}$ / e Å^{-3}	5.397/-6.937	3.096/-3.683

Table 4.2: Atomic coordinates and isotropic displacement parameters (U_{eq}) of SrPtPb and EuPtPb.

Atom	Wyckoff	x	y	z	U_{eq}
SrPtPb					
Sr1	4*c*	0.98302(9)	1/4	0.31005(9)	0.0107(2)
Pb1	4*c*	0.33147(4)	1/4	0.57636(3)	0.0098(1)
Pt1	4*c*	0.71095(4)	1/4	0.60153(4)	0.0109(1)
EuPtPb					
Eu1	4*c*	0.51849(13)	1/4	0.30967(14)	0.0108(3)
Pt1	4*c*	0.78427(11)	1/4	0.60223(10)	0.0105(2)
Pb1	4*c*	0.66901(10)	1/4	0.92449(10)	0.0099(2)

findings indicate the Pt-Pb interactions in EuPtPb and SrPtPb are weakly bonding and consistent with the covalent Pt-Pb bonding within the three-dimensional [Pt-Pb] network.

A structural visualization of EuPtPb and SrPtPb is shown in Figure 4.3. The europium and strontium are coordinated by two tilted and puckered Pt_3Pb_3 hexagonal rings, forming a distorted coordination environment. The interlayer Pt-Pb distances (2.8990(11) Å for EuPtPb and 2.9117(4) Å for SrPtPb) are only slightly longer than the intralayer bonds, underlining the three-dimensional character of the [PtPb] network. In both compounds, one platinum atom is significantly shifted off the first coordination sphere, lying at 3.8247(15) Å (EuPtPb) and 3.8266(13) Å (SrPtPb), compared with the Eu/Sr–Pt distances of 3.13–3.36 Å (EuPtPb) and 3.19–3.42 Å (SrPtPb) for the five closer neighbors. Each europium atom has two europium neighbors above and below the hexagons, as in the strontium sample. Besides Pt-Pb bonding, weak Pb-Pb contacts (3.6899(12) Å) are also observed, which are comparable to fcc lead (350 pm) [43]. The Pt-Pt distance of 277 pm in fcc platinum [43] is shorter than the Pt–Pb bonds. The local environments of Eu and Sr are illustrated in Figure 4.4, and these coordination patterns are consistent with the general features of the TiNiSi-type intermetallic family [29, 44–48].

We also compare EuPtPb and SrPtPb with REPdPb plumbides[49–52]. The phase EuPdPb also crystallizes in the TiNiSi-type structure, like EuPtPb and SrPtPb, and exhibits a stable divalent Eu^{2+} ground state. In contrast, LaPdPb adopts the ZrNiAl-type structure, and the larger cell volume per formula unit in EuPdPb reflects the larger size of divalent Eu relative to trivalent La [49]. The phases with RE = Y, La-Nd, Sm, and Gd-Yb all crystallize with the hexagonal ZrNiAl type structure [50–52]. Among these compounds, YbPdPb exhibits a positive deviation in cell volume, suggesting the presence of

Table 4.3: Selected distances (Å) in SrPtPb and EuPtPb.

atoms	distance(Å)	atoms	distance(Å)
SrPtPb			
Pb1—Sr3^{i}	3.5168(8)	Pb1—Sr3^{ii}	3.4589(12)
Pb1—Sr3^{iii}	3.3995(13)	Pb1—Sr3^{iv}	3.3826(9)
Pb1—Sr3^{v}	3.3826(9)	Pb1—Sr3^{vi}	3.5168(8)
Pt1—Sr3^{i}	3.2965(9)	Pt1—Sr3^{ii}	3.2965(9)
Pt1—Sr3^{iii}	3.4211(8)	Pt1—Sr3^{iv}	3.8266(13)
Pt1—Sr3^{v}	3.1852(13)	Pt1—Pb1	2.9117(6)
Pt1—Pb1^{i}	2.8214(3)	Pt1—Pb1^{ii}	2.8214(3)
Pt1—Sr3^{vi}	3.4211(8)	Pt1—Pb1^{iii}	2.8191(6)
EuPtPb			
Pb1—Pt1^{i}	2.7944(11)	Pb1—Pt1^{ii}	2.8083(6)
Pb1—Pt1^{iii}	2.8083(6)	Pb1—Pt1^{iv}	2.8990(11)
Pb1—Eu1^{v}	3.3656(10)	Pb1—Eu1^{vi}	3.3656(10)
Pb1—Eu1^{vii}	3.3710(15)	Pb1—Eu1^{viii}	3.4202(13)
Pb1—Eu1^{ix}	3.4676(9)	Pb1—Eu1^{x}	3.4676(9)
Pb1—Pb1^{xi}	3.6899(12)	Pb1—Pb1^{xii}	3.6899(12)
Pt1—Eu1^{xiii}	3.2767(9)	Pt1—Eu1^{xiv}	3.2767(9)
Pt1—Eu1^{xv}	3.3641(9)	Pt1—Eu1^{xvi}	3.3641(9)
Pt1—Eu1^{xvii}	3.8247(15)	Pt1—Eu1^{xviii}	3.1313(14)

intermediate-valent or divalent ytterbium. Notably, its unit cell volume exceeds even that of GdPdPb.

Although no Pauling electronegativity value is explicitly listed for strontium [39, 53], it can be reasonably assumed to be around 0.95, similar to calcium (1.00). In contrast, platinum (2.28) and lead (1.87) have much higher electronegativities, which supports the formation of polar-covalent Pt–Pb bonds within the structure.

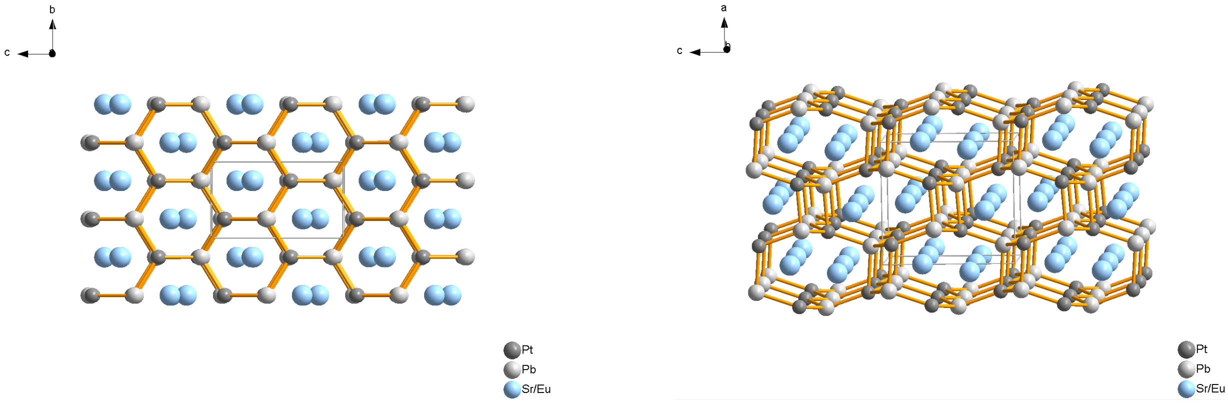

(a) (b)

Figure 4.3: View of the (Sr/Eu) PtPb structure approximately along the crystallographic *a* axis. Strotium and Europium are drawn as blue circles, while Platinum and lead atom are drawn as dark grey and medium grey, respectively.

4.4.2 Magnetic Susceptibility

Figure 4.5 presents the magnetic susceptibility data (χ = M/H) for the SrPtPb sample, measured while warming in a field of 3 T after zero field cooling to the lowest temperature 1.9 K. The susceptibility χ increases with decreasing temperature T, with an upturn below 100 K, but the values are extremely small and show only a weak temperature dependence. This behavior is characteristic of a response dominated by Pauli paramagnetism or diamagnetism. However, the temperature dependence of the susceptibility does not follow the Curie–Weiss (CW) behavior. An attempt to fit the data above 150 K using the Curie–Weiss law yields an unphysically large negative Curie temperature of -634 K and a small effective magnetic moment of 3.03 μ_B. The plot of χ^{-1} vs T shows a downward curvature that is most likely caused by trace paramagnetic impurities. Similar magnetic behavior has been observed in the related compound $SrPtPb_2$ [54]. In some metallic compounds, Pauli paramagnetism can even be overcompensated by the intrinsic diamagnetic contribution [55, 56]. Due to the impurity phases present in the EuPtPb sample, reliable susceptibility measurements were not possible. The data are included for completeness in the supporting information, as shown in Figure C.1, but are not discussed further in this chapter.

Magnetization isotherms for SrPtPb were measured at 1.9 K and 300 K in magnetic

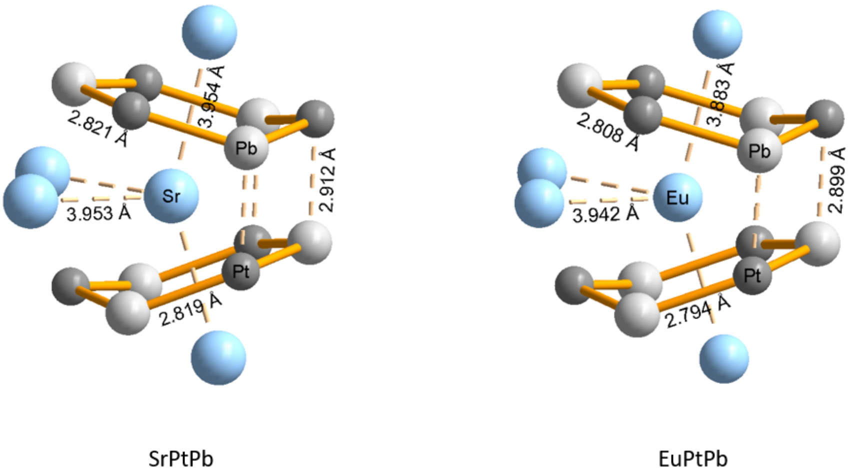

SrPtPb EuPtPb

Figure 4.4: Coordination of the strontium and europium atoms in the structures of SrPtPb and EuPtPb. Strontium or europium, platinum, and lead atoms are drawn as blue, dark grey, and medium grey.

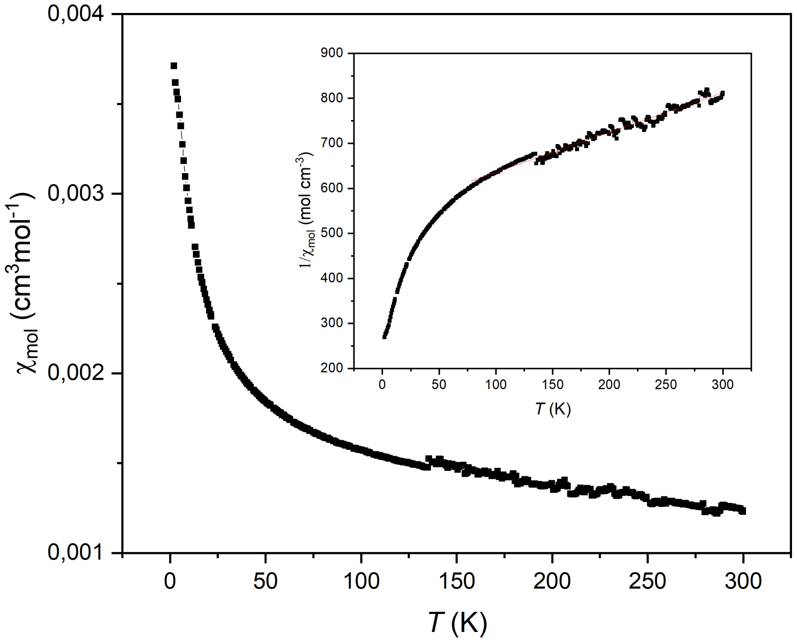

Figure 4.5: The temperature dependences of the molar magnetic susceptibility of SrPtPb and inverse magnetic susceptibility (inert) in a magnetic field of 3 T.

fields up to 50 kOe, as shown in Figure 4.6. At 300 K, the magnetization remains very small with only a weak field dependence, consistent with Pauli paramagnetism but with slight deviations due to minor impurities. At 1.9 K, the curve develops a pronounced S-shape, reflecting an additional weak ferromagnetic contribution superimposed on the paramagnetic background. In contrast, the EuPtPb sample exhibits unclear effects due to side phases during magnetization measurements, and the corresponding data are presented in Figure C.1, but will not be discussed here.

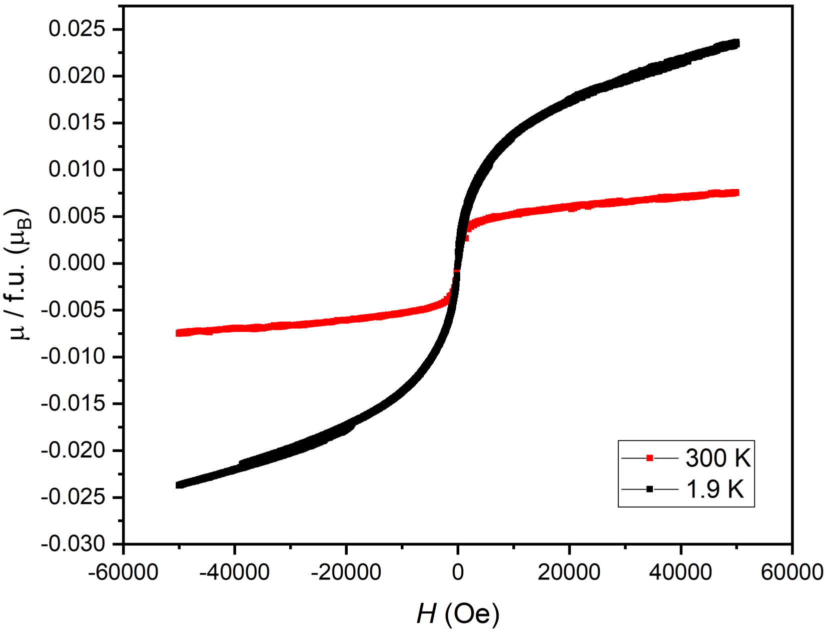

Figure 4.6: $M(H)$ curves for SrPtPb at 1.9 K and 300 K in the range of 2-300 K

4.4.3 Electrical Conductivity

The temperature-dependent electrical resistivity of SrPtPb is shown in Figure 4.7. The metallic behavior observed is consistent with the nature of intermetallic compounds, but it also suggests that residual structural disturbances may remain in the SrPtPb sample. These disturbances could arise from trace impurities undetectable by X-ray diffraction (XRD) or from strain distortions introduced by thermal stress during synthesis, possibly due to crucible–sample interaction.

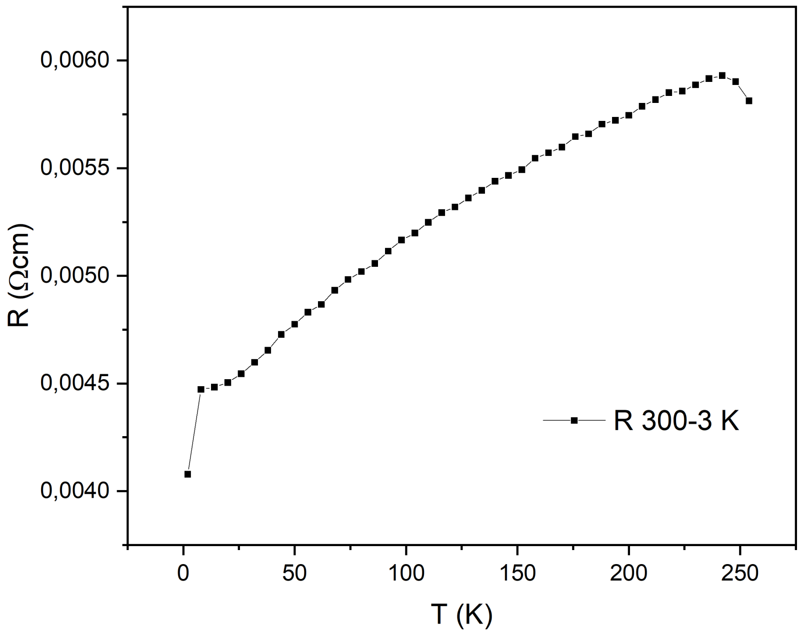

Figure 4.7: Temperature dependence of the electrical resistivity of SrPtPb.

4.5 Conclusion

The compounds SrPtPb and EuPtPb adopt the TiNiSi-type structure. While SrPtPb is structurally well-ordered and exhibits typical metallic conductivity, its resistivity anomaly near 275 K and non-Curie–Weiss magnetic response suggest subtle electronic or structural instabilities. The observed behavior is consistent with Pauli paramagnetism influenced by additional weak interactions, such as crystal field effects or conduction electron compensation. In contrast, EuPtPb contains significant secondary phases, preventing definitive conclusions regarding its physical properties. Further synthesis optimization and structural refinement are necessary, particularly for EuPtPb, to enable a more detailed investigation of its electronic and magnetic behavior.

References

[1] X. L. Qi and S. C. Zhang. Topological insulators and superconductors. *Rev. Mod. Phys.*, 83(4):1057–1110, 2011.

[2] J. Alicea. New directions in the pursuit of majorana fermions in solid state systems. *Rep. Prog. Phys.*, 75(7):076501, 2012.

[3] M. Mandal, N. C. Drucker, P. Siriviboon, T. Nguyen, A. Boonkird, T. N. Lamichhane, R. Okabe, A. Chotrattanapituk, and M. Li. Topological superconductors from a materials perspective. *Chem. Mater.*, 35(16):6184–6200, 2023.

[4] M. Sato and Y. Ando. Topological superconductors: a review. *Rep. Prog. Phys.*, 80(7):076501, 2017.

[5] L. Fu and E. Berg. Odd-parity topological superconductors: theory and application to $\mathrm{Cu_xBi_2Se_3}$. *Phys. Rev. Lett.*, 105(9):097001, 2010.

[6] P. Das, Y. Suzuki, M. Tachiki, and K. Kadowaki. Spin-triplet vortex state in the topological superconductor $\mathrm{Cu_xBi_2Se_3}$. *Phys. Rev. B Condens. Matter Mater. Phys.*, 83(22):220513, 2011.

[7] K. Matano, M. Kriener, K. Segawa, Y. Ando, and G. Q. Zheng. Spin-rotation symmetry breaking in the superconducting state of $\mathrm{Cu_xBi_2Se_3}$. *Nat. Phys.*, 12(9):852–854, 2016.

[8] L. M. Schoop, L. S. Xie, R. Chen, Q. D. Gibson, S. H. Lapidus, I. Kimchi, M. Hirschberger, N. Haldolaarachchige, M. N. Ali, C. A. Belvin, et al. Dirac metal to topological metal transition at a structural phase change in $\mathrm{Au_2Pb}$ and prediction of z2 topology for the superconductor. *Phys. Rev. B*, 91(21):214517, 2015.

[9] Y. Wu, G. Drachuck, L. L. Wang, D. D. Johnson, P. Swatek, B. Schrunk, D. X. Mou, L. N. Huang, S. L. Bud'Ko, P. C. Canfield, et al. Electronic structure of the topological superconductor candidate $\mathrm{Au_2Pb}$. *Phys. Rev. B*, 98(16):161107, 2018.

[10] T. Le, Y. Sun, H. K. Jin, L. Q. Che, L. C. Yin, J. Li, G. M. Pang, C. Q. Xu, L. X. Zhao, S. Kittaka, et al. Evidence for nematic superconductivity of topological surface states in $\mathrm{PbTaSe_2}$. *Sci. Bull.*, 65(16):1349–1355, 2020.

[11] K. Iwaya, Y. Kohsaka, K. Okawa, T. Machida, M. S. Bahramy, T. Hanaguri, and T. Sasagawa. Full-gap superconductivity in spin-polarised surface states of topological semimetal β-$\mathrm{pdbi_2}$. *Nat. Commun.*, 8(1):976, 2017.

[12] Y. Li, S. J. Yang, D. L. Sun, Y. B. Sun, Y. Li, E. Vetter, R. Sun, N. Li, X. Yang, L. Su, et al. Large spin to charge conversion in the topological superconductor β-$\mathrm{PdBi_2}$ at room temperature. *Phys. Rev. B*, 102(1):014420, 2020.

[13] Y. N. Li, Q. Q. Gu, C. Chen, J. Zhang, Q. Liu, X. Y. Hu, J. Liu, Y. Liu, L. S. Ling, M. L. Tian, et al. Nontrivial superconductivity in topological $\mathrm{MoTe_{2-x}S_x}$ crystals. *Proc. Natl. Acad. Sci*, 115(38):9503–9508, 2018.

[14] M. F. Gendron and R. E. Jones. Superconductivity in the $\mathrm{CuAl_2}$(C16) crystal class. *J. Phys. Chem. Solids*, 23(4):405–406, 1962.

[15] K. Lee, D. X. Mou, N. H. Jo, Y. Wu, B. Schrunk, J. M. Wilde, A. Kreyssig, A. Estry, S. L. Bud'ko, M. C. Nguyen, et al. Evidence for a large rashba splitting in $\mathrm{PtPb_4}$ from angle-resolved photoemission spectroscopy. *Phys. Rev. B*, 103(8):085125, 2021.

[16] T. Kong, K. Górnicka, S. Gołąb, B. Wiendlocha, T. Klimczuk, and R. J. Cava. A family of Pb-based superconductors with variable cubic to hexagonal packing. *J. Phys. Soc. Jpn.*, 87(7):074711, 2018.

[17] R. Pöttgen and R. Dronskowski. Structure, chemical bonding, and properties of $\mathrm{Sc_2Ni_2In}$. *Z. Anorg. Allg. Chem.*, 622(2):355–360, 1996.

[18] R. Pöttgen, A. Fugmann, R. D. Hoffmann, U. C. Rodewald, and D. Niepmann. Intermetallic cerium compounds with ordered $\mathrm{U_3Si_2}$ type structure. *Z. Naturforsch. B*, 55(2):155–161, 2000.

[19] R. Pöttgen. Ternary rare earth metal gold stannides and indides with ordered $\mathrm{U_3Si_2}$ and $\mathrm{Zr_3Al_2}$-type structure. *Z. Naturforsch. B*, 49(11):1525–1530, 1994.

[20] R. Pöttgen, P. E. Arpe, C. Felser, D. Kußmann, R. Müllmann, B. D. Mosel, B. Künnen, and G. Kotzyba. Structure and properties of $\mathrm{YbZnSn, YbAgSn}$, and $\mathrm{Yb_2Pt_2Pb}$. *J. Solid State Chem.*, 145(2):668–677, 1999.

[21] R. Movshovich, T. Graf, D. Mandrus, M. F. Hundley, J. D. Thompson, R. A. Fisher, N. E. Phillips, and J. L. Smith. Response of $\mathrm{CeRh_2Si_2}$ to pressure. *Phys. B*, 223:126–130, 1996.

[22] G. Melnyk, L. D. Gulay, and W. Tremel. Crystal structures of new ternary compounds in $\mathrm{RE-Pt-Pb}$ and $\mathrm{RE-Au-Pb}$ systems (RE= rare earth metal). *J. Alloys Compd.*, 528:70–73, 2012.

[23] G. Bruzzone and F. Merlo. The equilibrium phase diagram of the calcium-lead system and crystal structures of the compounds $\mathrm{CaPb, EuPb}$ and YbPb. *J. Less-Common Met.*, 48(1):103–109, 1976.

[24] A Iandelli and A Palenzona. The ytterbium-platinum system. *J. Less-Common Met.*, 43(1-2):205–209, 1975.

[25] K. T. Matsumoto, Y. Saiga, Y. F. Inoue, and T. Takabatake. Formation of a superlattice structure and suppression of the magnetic order in $\mathrm{Ce_{1-x}Pb_xPt_2}$ ($0 \leq \mathrm{x} < 0.5$). *J. Alloys Compd.*, 633:329–332, 2015.

[26] R. Pöttgen and D. Johrendt. Equiatomic intermetallic europium compounds: syntheses, crystal chemistry, chemical bonding, and physical properties. *Chem. Mater.*, 12(4):875–897, 2000.

[27] R. Pöttgen and B. Chevalier. Cerium intermetallics with ZrNiAl-type structure–a review. *Z. Naturforsch., B*, 70(5):289–304, 2015.

[28] R. Pöttgen, O. Janka, and B. Chevalier. Cerium intermetallics CeTX–review iii. *Z. Naturforsch., B*, 71(3):165–191, 2016.

[29] Oliver Janka, Oliver Niehaus, Rainer Pöttgen, and Bernard Chevalier. Cerium intermetallics with TiNiSi-type structure. *Z. Naturforsch., B*, 71(7):737–764, 2016.

[30] R. Pöttgen, D. Johrendt, and D. Kussmann. Structure-property relations of ternary equiatomic YbTX intermetallics. *Handbook on the physics and chemistry of rare earths*, 32:453–513, 2001.

[31] N. Lossau, H. Kierspel, J. Langen, W. Schlabitz, D. Wohlleben, A. Mewis, and Ch. Sauer. EuPtP: a new mixed valent europium-system. *Z. Phys. B: Condens. Matter*, 74:227–232, 1989.

[32] N. Lossau, H. Kierspel, F. Michels, G.and Oster, W. Schlabitz, D. Wohlleben, C. Sauer, and A. Mewis. Three magnetic order transitions in mixed valent EuPtP. *Z. Phys. B: Condens. Matter*, 77:393–397, 1989.

[33] G. Michels, S. Junk, N. Lossau, W. Schlabitz, D. Wohlleben, D. Johrendt, A. Mewis, Ch. Sauer, and Th. Woike. Mixed valency and first order phase transition in EuPdAs. *Z. Phys. B: Condens. Matter*, 86:53–58, 1992.

[34] Bruker AXS. *Apex3, version 2016.5–0.* Bruker AXS, Madison, Wisconsin, 2016.

[35] G. M. Sheldrick. Xprep, version 2008/2. bruker-axs, 2008.

[36] G. M. Sheldrick. Programs for crystallographic solution and refinement. *Acta Crystallogr. A*, 64:112–122, 2008.

[37] A Coelho. Topas-academic, version 4.1, coelho software, 2007.

[38] STOE & Cie GmbH. *Winxpow, Version 3.0.2.5.* STOE & Cie GmbH, Darmstadt, Germany, 2011. Software.

[39] L. Pauling. *The nature of the chemical bond and the structure of molecules and crystals: an introduction to modern structural chemistry*, volume 18. Cornell university press, 1960.

[40] J. Emsley. The elements: Oxford university press. *New York*, page p300, 1998.

[41] N. N. Zhuravlev, G. S. Zhdanov, and M. Smirnova Ye. Investigation of alloys of ternary alloys on a base of superconductive compounds. *Fiz. Met. Metalloved.*, 13(1):62–70, 1962.

[42] M. Ellner. Relationship between structural and thermodynamic properties in the copper group phases of $T_{10}B_4$ systems. *J. Less Common Met.*, 78(2), 1981.

[43] J. Donohue. Structures of the elements. *John Wiley and Sons, Inc.*, 1974.

[44] E. Parthé, L. Gelato, B. Chabot, M. Penzo, K. Cenzual, and R. Gladyshevskii. *TYPIX standardized data and crystal chemical characterization of inorganic structure types.* Springer Science & Business Media, Heidelberg, 2013.

[45] G. Nuspl, K. Polborn, J. Evers, G. A. Landrum, and R. Hoffmann. The four-connected net in the $CeCu_2$ structure and its ternary derivatives. its electronic and structural properties. *Inorg. Chem.*, 35(24):6922–6932, 1996.

[46] G. A. Landrum, R. Hoffmann, J. Evers, and H. Boysen. The TiNiSi family of compounds: structure and bonding. *Inorg. Chem.*, 37(22):5754–5763, 1998.

[47] R. D. Hoffmann and R. Pöttgen. AlB_2-related intermetallic compounds–a comprehensive view based on group-subgroup relations. *Kristallogr. – Cryst. Mater.*, 216(3):127–145, 2001.

[48] M. D. Bojin and R. Hoffmann. The re m e phases: I. an overview of their structural variety. *Helv. Chim. Acta.*, 86(5):1653–1682, 2003.

[49] L. Heletta, S. Klenner, T. Block, and R. Pöttgen. Antiferromagnetic ordering in the plumbide EuPdPb. *Z. Naturforsch., B*, 72(12):989–994, 2017.

[50] A. Iandelli. The structure of some ternary intermetallic compounds of the rare earths. *J. Alloys Compd.*, 203:137–138, 1994.

[51] R. Marazza, D. Mazzone, P. Riani, and G. Zanicchi. A contribution to the crystallochemistry of ternary 1: 1: 1 and 1: 1: 2 rare earth intermetallic phases with Pb and Pd. *J. Alloys Compd.*, 220(1-2):241–243, 1995.

[52] W. Hermes, S. Rayaprol, and R. Poettgen. Magnetic properties and specific heat studies of the plumbides CeTPb $(\mathrm{T} = \mathrm{Cu}, \mathrm{Pd}, \mathrm{Ag}, \mathrm{Au})$. *Z. Naturforsch. B*, 62(7):901–906, 2007.

[53] K. Ohwada. On the pauling electronegativity scales—ii. *Polyhedron*, 3(7):853–859, 1984.

[54] S. Klenner, J. Bönnighausen, and R. Pöttgen. Ternary plumbides $\mathrm{ATPb_2(A = Ca, Sr, Ba, Eu; T = Rh, Pd, Pt)}$ with distorted, lonsdaleite-related substructures of tetrahedrally connected lead atoms. *Z. Naturforsch. B*, 75(11):903–911, 2020.

[55] R. D. Hoffmann, U. C. Rodewald, and R. Pöttgen. $\mathrm{SrRhIn_2, SrPdIn_2, SrIrIn_2}$, and $\mathrm{SrPtIn_2}$–new intermetallic compounds with a filled variant of the $\mathrm{CaIn_2}$ structure. *Z. Naturforsch. B*, 54(1):38–44, 1999.

[56] R. D. Hoffmann, D. Kussmann, U. C. Rodewald, R. Poettgen, C. Rosenhahn, and B. D. Mosel. New stannides $\mathrm{CaTSn_2 (T = Rh, Pd, Ir)}$ and $\mathrm{Ca_2Pt_3Sn_5}$-synthesis, structure and chemical bonding. *Z. Naturforsch. B.*, 54(6):709–717, 1999.

Chapter 5

Synthesis and Structure of the Rubidium Phosphidosilicate $RbSi_2P_3$

5.1 Abstract

$RbSi_2P_3$ and a series of Al-substituted derivatives were synthesized by high-temperature solid-state reactions from the elements under an argon atmosphere at 1040 °C. Single-crystal X-ray diffraction shows that $RbSi_2P_3$ crystallizes in the centrosymmetric monoclinic space group $C2/c$ (No. 15), adopting the same structure type as KSi_2P_3. Its structure is built from T3 supertetrahedral units of corner-sharing SiP_4 tetrahedra, in which each T3 cluster shares a single tetrahedron with its neighbor, resulting in a layered arrangement of supertetrahedra separated by Rb^+ cations. Partial substitution of Si by Al and Ga suggests the possibility of a structural phase transition, with indications of T5-type supertetrahedral motifs emerging at doping levels below 10%. This observation points to the chemical flexibility of the phosphidosilicate framework and suggests that trivalent dopants such as Al^{3+} and Ga^{3+} may be able to modulate framework connectivity. Such aliovalent substitutions could provide a promising route to tune network dimensionality and enhance alkali-ion transport, positioning $RbSi_2P_3$ and related materials as candidate platforms for solid-state ion conductors.

For substitution experiments, silicon was partially replaced by aluminum or gallium according to the nominal compositions $Rb(Si_{1-x}M_x)_2P_3$ (M = Al, Ga; $x = 0.02$–0.10). The mixtures were prepared from the elements in the glovebox, loaded and sealed in the same manner, and subjected to the identical heating program as used for the parent $RbSi_2P_3$.

5.2 Introduction

Ternary phosphidosilicates exhibit diverse structures based on SiP_4 tetrahedra, which connect via corners or edges to form insular entities, chains, layers, or complex three-dimensional networks. Representative examples include $[Si_2P_6]^{10-}$ anions in Na_5SiP_3 [1], infinite $^1_\infty[SiP_{4/2}]^{2-}$ chains in K_2SiP_2 [2], double layers of SiP_4 tetrahedron in KSi_2P_3 [3], and interpenetrating three-dimensional networks $[SiP_{4/2}]^{2-}$ in $MgSiP_2$ [4], and unique trigonal-planar $[SiP_3]^{5-}$ in Cs_5SiP_3 [5]. These materials are structurally versatile and chemically rich.

In recent years, interest in phosphidosilicates has grown significantly since the discovery of Li_8SiP_4, which showed promising ionic conductivity of $1.2{\cdot}10^{-4}$ S cm^{-1} and low activation energy of 0.37 eV [6]. Further developments, such as $Li_{14}SiP_6$ with conductivity up to 10^{-3} S cm^{-1}, demonstrated their potential as solid-state electrolytes [7, 8]. The size of tetrahedra currently ranges from the smallest T2 [9] up to T6 [10]. Haffner et. al [11] reported a series of Na^+ ion fast solid-state conductors following the formula $Na_{23}Si_{9n+19}P_{12n+33}$ (n = 0-3), demonstrating the evolution T3T3 → T3T4 → T4T4 → T5T5 (or T4T5) can be rationalized by adding charge-neutral 3×"Si_3P_4". This demonstrates a controlled strategy to construct increasingly open frameworks, where the number of partially occupied Na^+ sites increases with cluster size, thereby enhancing ionic conductivity.

A representative example of supertetrahedral evolution is found in KSi_2P_3 [3, 12], which contains T3 supertetrahedra according to the Yaghi nomenclature [13]. These T3 entities are fused via a shared SiP_4 unit, forming layered structures with K^+ ions on two fully occupied general Wyckoff sites.[3] Upon heating above 1040°C, it transforms into a T5-type phase (KSi_2P_3-$tI960$, space group $I4_1/acd$), resembling the structure of homeotypic HT-$NaSi_2P_3$ [11]. Each T5 cluster has a central silicon vacancy, causing a slight shift of the four nearby phosphorus atoms towards the vacancy. The potassium ion resides in big cavities with high displacement and partial occupancy of 0.4. KSi_2P_3-$tI960$ undergoes enantiotropic displacive phase transitions upon heating and cooling, converting from the tetragonal phase (space group $I4_1/acd$) to orthorhombic (space group $Fddd$) and monoclinic (space group $C2/c$) subgroups via *translationsgleiche*(t2) symmetry reductions [12].

$RbSi_2P_3$ was synthesized under conditions similar to those for KSi_2P_3 and obtained a T3-type structure stable up to 1040°C. Group 13 dopants, particularly Al^{3+}, have been shown to preferentially occupy Si^{4+} sites in Li_2SiP_2, showing that trivalent doping $Al^{3+}$is more preferable on the Si^{4+} site than the Li^+, with Al^{3+} displaying the lowest incorporation energy among B^{3+}, Al^{3+}, and Ga^{3+} [14]. Similar incorporation behavior is known in the zeolites [15–19]. Doping Li_2SiP_2 with 10% Al_{Si}' dopand clustering leads to enhanced ionic conductivities at low temperature compared to undoped Li_2SiP_2 [6, 14]. Motivated by these insights, we introduced aluminum and gallium into $RbSi_2P_3$ to explore its influence on structural evolution.

5.3 Results and Discussion

5.3.1 Crystal chemistry of $RbSi_2P_3$

$RbSi_2P_3$ was synthesized by heating stoichiometric mixtures of the elements in alumina crucibles, which were sealed in evacuated silica tubes under a purified argon atmosphere. Optimized heating procedures yielded air-stable black polycrystalline samples. Single crystals suitable for X-ray diffraction were selected for structural analysis. The crystal structure was solved using single-crystal diffraction datasets via direct methods [20] and refined in monoclinic space group $C2/c$. The final parameters of the refinements are summarized in Table 5.1, while the atomic positions, equivalent and anisotropic displacement factors are listed in Table D.3 in the supporting information. Rietveld refinements based on powder X-ray diffraction data confirmed the structural model and high purity of the samples (Figure 5.1). Energy-dispersive X-ray spectra confirm the chemical compositions (Figure D.1).

Structurally, $RbSi_2P_3$ adopts the same framework as KSi_2P_3, which was first described by Feng et al.[3]. It consists of T3 supertetrahedra units, according to the nomenclature of Yaghi [13], composed of corner-sharing SiP_4 tetrahedra. Each T3 entity shares a single SiP_4 tetrahedron with neighboring units, resulting in a layered structure. Rb^+ ions are located at two fully occupied general Wyckoff sites between T3 supertetrahedra layers (Figure 5.2). This structure is stable up to 1040 °C. The asymmetric unit contains two crystallographically independent Rb atoms, five unique Si atoms, and six P atoms. Si_1 and Si_5 atoms are located on the $4e$ Wyckoff site, while other atoms are at the $8f$ sites. As no P-P bonds are observed in the structure, the oxidation states can be assigned as Rb^{1+}, Si^{4+}, and P^{3-}.

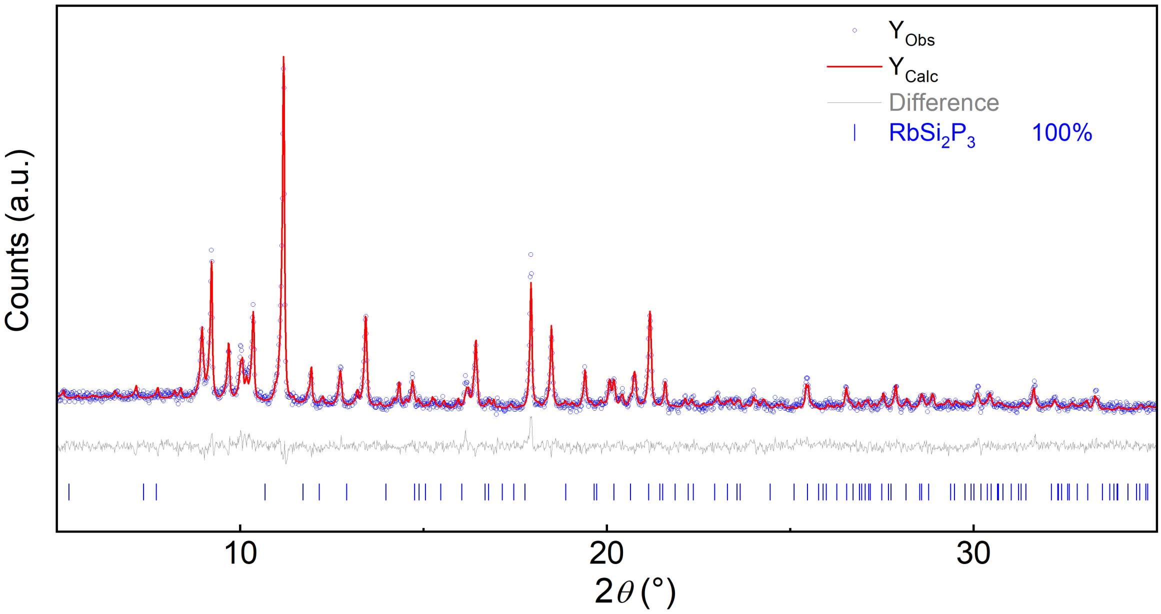

Figure 5.1: X-ray powder diffraction patterns of $RbSi_2P_3$

Each Si atom is tetrahedrally coordinated by four P atoms, forming SiP_4 tetrahedron. These tetrahedra are linked by corner-sharing P atoms to form two-dimensional ${}^2_\infty[Si_2P_3]$ layers. The Si-P bond lengths in $RbSi_2P_3$ range from 2.209(14) to 2.308(13) Å, as shown in Table 5.2, which are comparable to those in K_2SiP_2 (2.272(7)Å) [2], KSi_2P_3 (2.221(2) to 2.270(2) Å) [3], and Na_5SiP_3 (2.258(3) to 2.335(1) Å) [21]. The P-Si-P angles are between 104.0(7) and 118.3(9), a narrower range than in KSi_2P_3 and K_2SiP_2 (95.55(2) to 120.00(2))

Table 5.1: Crystallographic data for the refinement of $RbSi_2P_3$.

Formula	$RbSi_2P_3$
Space Group	$C2/c$ (No. 15)
a / Å	10.1586(4)
b / Å	10.1599(4)
c / Å	21.6830(8)
α / °	90
β / °	96.720(2)
V_{cell} / Å^3	2222.54(15)
Z	16
$\rho_{\text{X-ray}}$ / g cm^{-3}	2.804
μ / mm^{-1}	10.043
Θ-range / °	1.891- 30.541
reflections measured	24066
independent reflections	3409
parameters	110
R_σ	0.0355
R_{int}	0.0603
R_1 ($F^2>2\sigma$ (F^2)) / all	0.0558/0.0934
wR_2 ($F^2>2\sigma$ (F^2)) / all	0.1346/0.1581
GooF	1.051
$\Delta\rho_{\mathrm{max/min}}$ / e Å^{-3}	2.556/-0.817

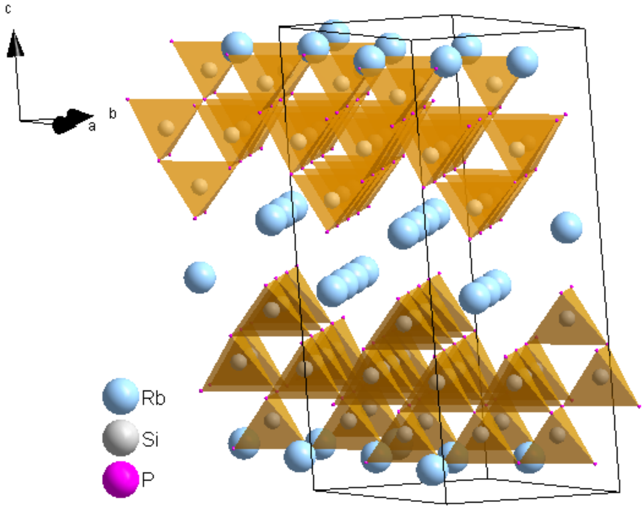

Figure 5.2: The crystal structure of $RbSi_2P_3$.

[3, 12], indicating reduced distortion of the SiP_4 tetrahedra in $RbSi_2P_3$. As illustrated in Figure 5.3, Rb^+ cations are coordinated by eight P atoms with bond distances ranging from 3.393(14) to 3.611(12)Å, resembling those in KSi_2P_3.

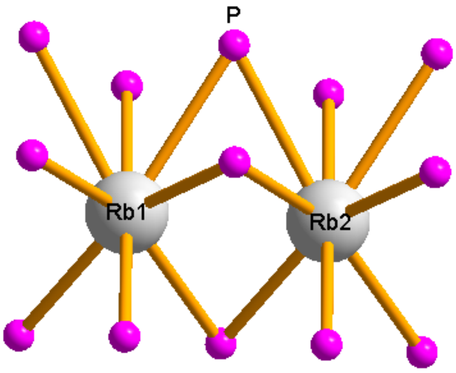

Figure 5.3: The coordination environments of Rb atoms in $RbSi_2P_3$

Table 5.2: Selected distances (Å) in $RbSi_2P_3$.

atoms	distance(Å)	atoms	distance(Å)
P1—Si4	2.229(3)	P1—Si5	2.231(3)
P2—Si5	2.231(3)	P2—Si4	2.229(3)
P3—Si3	2.262(4)	P3—Si5	2.249(3)
P3—Si1	2.260(3)	P4—Si2	2.263(4)
P4—Si3	2.270(3)	P4—Si4	2.260(3)
P5—Si4	2.258(3)	P5—Si3	2.268(3)
P5—Si1	2.269(4)	P6—Si5	2.246(3)
P6—Si2	2.261(4)	P6—Si3	2.263(3)
Rb1—Rb2^{i}	4.9304(9)	Rb1—Rb2^{ii}	3.599(2)
Rb1—Rb2^{iii}	3.585(2)	Rb1—Rb1	4.933(2)
Rb1—P2^{i}	3.593(4)	Rb1—P2^{ii}	3.591(4)
Rb1—P2^{iii}	3.4181(17)	Rb1—P1	3.417(3)
Rb1—P4	3.577(3)	Rb1—P5	3.575(3)
Rb1—P6	3.566(3)	Rb1—P3	3.563(3)
Rb2—Rb2	4.928(2)	Rb2—P1^{i}	3.593(4)
Rb2—P1^{ii}	3.4137(18)	Rb2—P1^{iii}	3.591(4)
Rb2—P5	3.574(3)	Rb2—P4	3.571(3)
Rb2—P3	3.563(3)	Rb2—P6	3.562(3)
Rb2—P2	3.416(4)		

5.3.2 Doping effects and structural Transitions

As reported in [14], Al^{3+} doping in Li_2SiP_2 preferentially occurs at silicon sites rather than lithium sites, with extremely low defect incorporation energy, remaining nearly constant up to 10% doping. While the energy per Al_{Si}' dopand clustering defect is small, indicating a tendency for stable systems. Compared to other trivalent group 13 dopands such as boron and gallium, aluminum shows the lowest incorporation energy. Experimental ionic conductivities correlate well with computed lithium diffusion coefficients, typically related via the Haven ratio [22]. Notably, 10% Al_{Si}' compensated doping results in significantly enhanced Li-ion conductivity at lower temperatures, with lower activation energies than in undoped Li_2SiP_2, confirming the beneficial role of trivalent doping on ionic transport properties [14]. By the same substitution principle, Ga^{3+} is also a chemically reasonable dopant for Si^{4+} sites.

Experimental evidence for such substitution is provided by several Ga–Si–As compounds. In MSiAs$_2$ (M = Sr, Eu), all tetrahedral sites are exclusively occupied by Si, corresponding to a Ga:Si ratio of 0:1. In MGaSiAs$_3$ (M = Sr, Eu), the Ga:Si ratio is 1:1, and single-crystal refinements reveal a non-random distribution, with Si preferentially located in fused tetrahedra. In $M_4Ga_5SiAs_9$ (Ga:Si=5:1), Ga and Si statistically share the (Ga/Si)As_4 tetrahedral with slightly different Ga–As and Si–As distances, while no long-range ordering is detected [23]. Additional evidence is found in $Li_{1.5}Ga_{0.9}Si_{3.1}As_4$ [24], which crystallizes in the monoclinic space group $C2/c$ (No. 15) and contains alternating layers along the c-axis. One layer consists of corner-sharing $(Si_{1-x}Ga_x)As_4$ tetrahedral, confirming the structural compatibility of Ga and Si in tetrahedral coordination. Together, these examples demonstrate that Ga can readily substitute for Si in tetrahedral sites, both from an energetic perspective and as validated by experimental crystal structures.

In contrast, we consider $RbSi_2P_3$ to have fully occupied Rb sites. Thus, the motivation for Al or Ga substitution is not related to filling Rb vacancies but rather to modifying the tetrahedral framework itself. Indeed, two reported studies already demonstrate that Ga can substitute for Si and that the substitution ratio can vary across different compounds. This implies that the Si–P tetrahedron can also be constructed with corner-sharing $Si_{1-x}Ga_xAs_4$ tetrahedra. Notably, both $RbSi_2P_3$ and $Li_{1.5}Ga_{0.9}Si_{3.1}As_4$ adopt T3-type supertetrahedral cluster motifs arranged in layered structures. We could not synthesize suitable single crystals of the compounds after diluting with Al, mainly due to twinning. Detailed investigations of the ionic conductivity of these materials are now in progress.

5.4 Conclusion

The new compound $RbSi_2P_3$ has been synthesized and crystallizes in the centrosymmetric space group $C2/c$. It has the same structure type as KSi_2P_3, built from T3 supertetrahedral units of corner-sharing SiP_4 tetrahedra. Each supertetrahedron shares a single SiP_4 tetrahedron with its neighbors, giving rise to a layered arrangement of T3 clusters separated by Rb^+ cations along the c-axis. Preliminary substitution experiments indicate that partial replacement of Si by Al induces structural instability and may trigger a phase transition. This chemical flexibility suggests that aliovalent substitution could be a viable route to tune the stability and potentially enhance the ionic transport properties of $RbSi_2P_3$.

5.5 Experimental Section

All experiments and measurements were performed in an argon-filled glovebox. The compounds were synthesized by solid state reaction of the elements in alumina crucibles at 750 to 1040°C. Further details on elemental analysis are in the supporting Information.

References

[1] B. Eisenmann and M. Somer. Neue ternäre alkaliphosphide mit kupfer, zink und cadmium: $K_2CuP, NaZnP$ und K_4CdP_2 on new ternary alkali metal phosphides: $K_2CuP, NaZnP$ and K_4CdP_2. *Z. Naturforsch. B*, 40(11):1419–1423, 1985.

[2] B. Eisenmann and M. Somer. K_2SiP_2, ein phosphidopolysilikat (iv)/K_2SiP_2, a phosphidopolysilicate (iv). *Z. Naturforsch. B*, 39(6):736–738, 1984.

[3] K. Feng, L. Kang, W. L. Yin, W. Y. Hao, Z. S. Lin, J. Y. Yao, and Y. C. Wu. KSi_2P_3: A new layered phosphidopolysilicate (iv). *J. Solid State Chem.*, 205:129–133, 2013.

[4] A. J. Springthorpe and J. G. Harrison. $MgSiP_2$: a new member of the $II\,IV\,V_2$ family of semiconducting compounds. *Nat.*, 222(5197):977–977, 1969.

[5] B. Eisenmann, J. Klein, and M. Somer. Co-isostere anionen in $Cs_5SiP_3, Cs_5SiAs_3, Cs_5GeP_3$ und Cs_5GeAs_3. *Angew. Chem.*, 102(1):92–93, 1990.

[6] L. Toffoletti, H. Kirchhain, J. Landesfeind, W. Klein, L. van Wüllen, H. A. Gasteiger, and T. F. Fässler. Lithium ion mobility in lithium phosphidosilicates: crystal structure, 7Li, 29Si, and 31 P MAS NMRspectroscopy, and impedance spectroscopy of Li_8SiP_4 and Li_2SiP_2. *Chem. Eur. J.*, 22(49):17635–17645, 2016.

[7] H. Eickhoff, L. Toffoletti, W. Klein, G. Raudaschl-Sieber, and T. F. Fässler. Synthesis and characterization of the lithium-rich phosphidosilicates $Li_{10}Si_2P_6$ and $Li_3Si_3P_7$. *Inorg. Chem.*, 56(11):6688–6694, 2017.

[8] S. Strangmüller, H. Eickhoff, D. Müller, W. Klein, G. Raudaschl-Sieber, H. Kirchhain, C. Sedlmeier, V. Baran, A. Senyshyn, V. L. Deringer, et al. Fast ionic conductivity in the most lithium-rich phosphidosilicate $Li_{14}SiP_6$. *JACS*, 141(36):14200–14209, 2019.

[9] A. Haffner, T. Bräuniger, and D. Johrendt. Supertetrahedral networks and lithium-ion mobility in Li_2SiP_2 and $LiSi_2P_3$. *Angew. Chem. Int. Ed.*, 55(43):13585–13588, 2016.

[10] X. F. Xu, W. Wang, D. L. Liu, D. D. Hu, T. Wu, X. H. Bu, and P. Y. Feng. Pushing up the size limit of metal chalcogenide supertetrahedral nanocluster. *JACS*, 140(3):888–891, 2018.

[11] A. Haffner, A. K. Hatz, I. Moudrakovski, B. V. Lotsch, and D. Johrendt. Fast sodium-ion conductivity in supertetrahedral phosphidosilicates. *Angew. Chem.*, 130(21):6263–6268, 2018.

[12] A. Haffner, A. K. Hatz, O. E. Zeman, C. Hoch, B. V. Lotsch, and D. Johrendt. Polymorphism and fast potassium-ion conduction in the T5 supertetrahedral phosphidosilicate KSi_2P_3. *Angew. Chem. Int. Ed.*, 60(24):13641–13646, 2021.

[13] H. Li, J. Kim, T. L. Groy, M. O'Keeffe, and O. M. Yaghi. 20 å $Cd_4In_{16}S_35_{14}$-supertetrahedral T4 clusters as building units in decorated cristobalite frameworks. *JACS*, 123(20):4867–4868, 2001.

[14] S. R. Yeandel, D. O. Scanlon, and P. Goddard. Enhanced li-ion dynamics in trivalently doped lithium phosphidosilicate Li_2SiP_2: a candidate material as a solid li electrolyte. *JMCA*, 7(8):3953–3961, 2019.

[15] G. R. Eulenberger, D. P. Shoemaker, and J. G. Keil. Crystal structures of hydrated and dehydrated synthetic zeolites with faujasite aluminosilicate frameworks. i. the dehydrated sodium, potassium, and silver forms. *J. Phys. Chem.*, 71(6):1812–1819, 1967.

[16] T. Xue, H. P. Liu, Y. Zhang, H. H. Wu, P. Wu, and M. Y. He. Synthesis of ZSM-5 with hierarchical porosity: In-situ conversion of the mesoporous silica-alumina species to hierarchical zeolite. *Microporous Mesoporous Mater.*, 242:190–199, 2017.

[17] R. M. Barrer and E. F. Freund. Hydrothermal chemistry of silicates. part XVI. replacement of aluminium by boron during zeolite growth. *J. Chem. Soc., Dalton Trans.*, (10):1049–1053, 1974.

[18] M. V. Shamzhy, C. Ochoa-Hernández, V. I. Kasneryk, M. V. Opanasenko, and M. Mazur. Direct incorporation of B, Al, and Ga into medium-pore ith zeolite: Synthesis, acidic, and catalytic properties. *Catal. Today*, 277:37–47, 2016.

[19] R. Fricke, H. Kosslick, G. Lischke, and M. Richter. Incorporation of gallium into zeolites: syntheses, properties and catalytic application. *Chem. Rev.*, 100(6):2303–2406, 2000.

[20] G. M. Sheldrick. A short history of SHELX. *Acta Crystallogr., A, Found. Crystallogr.*, 64(1):112–122, 2008.

[21] B. Eisenmann and M. Somer. Zur kenntnis von oligophosphidosilikaten (iv) und-germanaten (iv): $Na_{10}Si_2P_6$ und $Na_{10}Ge_2P_6$. *Z. Naturforsch. B*, 40(7):886–890, 1985.

[22] G. E. Murch. The haven ratio in fast ionic conductors. *Solid State Ion.*, 7(3):177–198, 1982.

[23] V. Weippert, A. Haffner, and D. Johrendt. New layered supertetrahedral compounds $T2-MSiAs_2$, $T3-MGaSiAs_3$ and polytypic $T4-M4Ga_5SiAs_9(M=Sr, Eu)$. *Z. Naturforsch. B.*, 75(11):983–989, 2020.

[24] M. Schöneich, L. G. Balzat, B. V. Lotsch, and D. Johrendt. Sodium filling in superadamantoide $Na_{1.36}(Si_{0.86}Ga_{0.14})_2As_{2.98}$ and the mixed valent arsenidosilicate-silicide $Li_{1.5}Ga_{0.9}Si_{3.1}As_4$. *Inorg.*, 12(6):166, 2024.

Chapter 6

Summary

This thesis presents a study of layered intermetallic and supertetrahedral phosphidosilicate compounds, focusing on their crystal structures and magnetic behavior. The research is divided into two main thematic parts: the first investigates honeycomb-related intermetallic compounds, while the latter part explores alkali-metal phosphidosilicates with tunable network dimensionality.

In Chapter 2, the synthesis and characterization of NdPtAs are presented. This compound crystallizes in the hexagonal YPtAs-type structure (space group $P6_3/mmc$), featuring puckered Pt–As honeycomb layers separated by Nd layers. Magnetic susceptibility measurements indicate antiferromagnetic ordering below $\sim$ 9 K, with an effective magnetic moment of μ_{eff} = 3.12 μ_{B} and a Weiss constant θ_{P} = -9.83(10) K. These results confirm the presence of localized Nd^{3+} moments and dominant antiferromagnetic exchange interactions. This study completes the *RE*PtAs (*RE* = La–Nd) series and reinforces structural and magnetic trends within the family.

Chapter 3 focuses on the synthesis and structural characterization of plumbides *AE*AuPb (*AE* = Ca, Sr, Ba). These compounds crystallize in a ternary variant of the KHg_2-type structure (space group *Imma*, No. 74), a distorted derivative of the AlB_2 prototype. Gold and lead are indistinguishable by X-ray analysis, which leads to the KHg_2-type and not to the TiNiSi-type with ordered distribution. Lattice parameters exhibit systematic expansion along the *b*-axis with increasing alkaline-earth cation size, from Ca to Ba. All three compounds display metallic conductivity and weak diamagnetism or temperature-independent paramagnetism, consistent with nonmagnetic ground states. Comparison with the isotypic compound EuAuPb suggests compatibility between Europium divalent rare-earth and alkaline-earth analogues in this structural family.

In Chapter 4, the TiNiSi-type intermetallics SrPtPb and EuPtPb are studied. Both compounds crystallize in the orthorhombic space group *Pnma* with complete ordering of platinum and lead atoms. While the SrPtPb sample is nearly phase pure, EuPtPb contains significant side phases. SrPtPb exhibits metallic conductivity, and magnetic susceptibility measurements suggest weak, temperature-independent paramagnetism. A resistivity anomaly was observed near 275 K in SrPtPb, showing no hysteresis and potentially indicating a subtle phase instability. The observed magnetic response, nonlinear χ^{-1} vs T, and a small effective moment can be attributed to Pauli paramagnetism. Due to impurity phases, no definitive physical property analysis was conducted for EuPtPb.

The final section, Chapter 5, focuses on supertetrahedral phosphidosilicate frameworks. The compound $RbSi_2P_3$ and a series of Al-substituted quaternary derivatives were synthesized via high-temperature solid-state reactions under an argon atmosphere. Single-crystal X-ray diffraction reveals that $RbSi_2P_3$ crystallizes in the centrosymmetric monoclinic space group $C2/c$ (No. 15), isotypic with KSi_2P_3, and is constructed from T3 supertetrahedral units of corner-sharing SiP_4 tetrahedra. Each T3 cluster shares a single tetrahedron with its neighbors, resulting in a layered arrangement of supertetrahedra separated by Rb^+ cations. Preliminary substitution experiments suggest that partial replacement of Si by Al may influence the framework connectivity. Such observations imply that trivalent dopants such as Al^{3+} and Ga^{3+} could tune structural features and potentially enhance alkali-ion transport properties, underscoring the promise of supertetrahedral phosphidosilicates as tunable platforms for solid-state ion conductors.

In conclusion, this thesis contributes to the understanding of both layered intermetallic systems and phosphidosilicate networks, offering new insights into their structural diversity, electronic behavior, and potential functional applications.

Appendix A

Supporting Information for Chapter 2

A.1 Crystallographic Data of NdPtAs

Table A.1: Anisotropic Displacement Parameters (Å^2) of NdPtAs from single crystal data.

Atom	U_{11}	U_{22}	U_{33}	U_{12}	U_{13}	U_{23}
Pt1	0.00660	0.00660	0.01110	0.00330	0.00000	0.00000
As1	0.00720	0.00720	0.01090	0.00360	0.00000	0.00000
Nd1	0.00640	0.00640	0.00670	0.00320	0.00000	0.00000
Nd2	0.00650	0.00650	0.00640	0.00320	0.00000	0.00000

Table A.2: Selected angle (°) in NdPtAs.

atoms	angle(°)	atoms	angle(°)
As1—Pt1—As1^{i}	119.617(11)	As1^{xi}—Nd1—Pt1^{xi}	46.211(9)
As1—Pt1—As1^{ii}	119.617(11)	As1^{ix}—Nd1—Pt1^{xi}	133.789(9)
As1^{i}—Pt1—As1^{ii}	119.616(10)	As1^{xii}—Nd1—Pt1^{xi}	46.212(9)
As1—Pt1—Nd2^{iii}	68.86(3)	As1—Nd1—Pt1^{xi}	133.789(9)

atoms	angle(°)	atoms	angle(°)
As1^{i}—Pt1—Nd2^{iii}	146.48(5)	Pt1^{viii}—Nd1—Pt1^{xi}	96.069(13)
As1^{ii}—Pt1—Nd2^{iii}	68.87(3)	Pt1^{x}—Nd1—Pt1^{xi}	83.931(12)
As1—Pt1—Nd2^{iv}	146.48(5)	As1^{x}—Nd1—Pt1^{ix}	76.71(2)
As1^{i}—Pt1—Nd2^{iv}	68.86(3)	As1^{viii}—Nd1—Pt1^{ix}	103.29(2)
As1^{ii}—Pt1—Nd2^{iv}	68.86(3)	As1^{xi}—Nd1—Pt1^{ix}	133.789(9)
Nd2^{iii}—Pt1—Nd2^{iv}	87.394(13)	As1^{ix}—Nd1—Pt1^{ix}	46.211(9)
As1—Pt1—Nd2^{v}	68.86(3)	As1^{xii}—Nd1—Pt1^{ix}	133.788(9)
As1^{i}—Pt1—Nd2^{v}	68.87(3)	As1—Nd1—Pt1^{ix}	46.212(9)
As1^{ii}—Pt1—Nd2^{v}	146.48(5)	Pt1^{viii}—Nd1—Pt1^{ix}	83.931(12)
Nd2^{iii}—Pt1—Nd2^{v}	87.394(13)	Pt1^{x}—Nd1—Pt1^{ix}	96.069(13)
Nd2^{iv}—Pt1—Nd2^{v}	87.394(13)	Pt1^{xi}—Nd1—Pt1^{ix}	180.000
As1—Pt1—Nd1^{i}	64.86(3)	As1^{x}—Nd1—Pt1^{xiii}	46.212(9)
As1^{i}—Pt1—Nd1^{i}	64.86(3)	As1^{viii}—Nd1—Pt1^{xiii}	133.788(9)
As1^{ii}—Pt1—Nd1^{i}	136.98(5)	As1^{xi}—Nd1—Pt1^{xiii}	46.212(9)
Nd2^{iii}—Pt1—Nd1^{i}	133.724(1)	As1^{ix}—Nd1—Pt1^{xiii}	133.788(9)
Nd2^{iv}—Pt1—Nd1^{i}	133.724(1)	As1^{xii}—Nd1—Pt1^{xiii}	103.29(2)
Nd2^{v}—Pt1—Nd1^{i}	76.543(2)	As1—Nd1—Pt1^{xiii}	76.71(2)
As1—Pt1—Nd1^{vi}	136.98(5)	Pt1^{viii}—Nd1—Pt1^{xiii}	96.070(12)
As1^{i}—Pt1—Nd1^{vi}	64.86(3)	Pt1^{x}—Nd1—Pt1^{xiii}	83.930(12)
As1^{ii}—Pt1—Nd1^{vi}	64.86(3)	Pt1^{xi}—Nd1—Pt1^{xiii}	83.930(13)
Nd2^{iii}—Pt1—Nd1^{vi}	133.724(1)	Pt1^{ix}—Nd1—Pt1^{xiii}	96.070(12)
Nd2^{iv}—Pt1—Nd1^{vi}	76.543(2)	As1^{x}—Nd1—Pt1^{xiv}	133.788(9)
Nd2^{v}—Pt1—Nd1^{vi}	133.724(1)	As1^{viii}—Nd1—Pt1^{xiv}	46.212(9)
Nd1^{i}—Pt1—Nd1^{vi}	83.930(12)	As1^{xi}—Nd1—Pt1^{xiv}	133.788(9)
As1—Pt1—Nd1^{ii}	64.86(3)	As1^{ix}—Nd1—Pt1^{xiv}	46.212(9)
As1^{i}—Pt1—Nd1^{ii}	136.98(5)	As1^{xii}—Nd1—Pt1^{xiv}	76.71(2)
As1^{ii}—Pt1—Nd1^{ii}	64.86(3)	As1—Nd1—Pt1^{xiv}	103.29(2)

atoms	angle(°)	atoms	angle(°)
$Nd2^{iii}$—Pt1—$Nd1^{ii}$	76.543(2)	$Pt1^{viii}$—Nd1—$Pt1^{xiv}$	83.930(12)
$Nd2^{iv}$—Pt1—$Nd1^{ii}$	133.724(1)	$Pt1^{x}$—Nd1—$Pt1^{xiv}$	96.070(12)
$Nd2^{v}$—Pt1—$Nd1^{ii}$	133.724(1)	$Pt1^{xi}$—Nd1—$Pt1^{xiv}$	96.070(12)
$Nd1^{i}$—Pt1—$Nd1^{ii}$	83.930(12)	$Pt1^{ix}$—Nd1—$Pt1^{xiv}$	83.930(12)
$Nd1^{vi}$—Pt1—$Nd1^{ii}$	83.930(12)	$Pt1^{xiii}$—Nd1—$Pt1^{xiv}$	180.000
$Pt1^{viii}$—As1—$Pt1^{ix}$	119.616(10)	$Pt1^{xv}$—Nd2—$Pt1^{xvi}$	132.987(6)
$Pt1^{viii}$—As1—Pt1	119.617(10)	$Pt1^{xv}$—Nd2—$Pt1^{xvii}$	74.176(18)
$Pt1^{ix}$—As1—Pt1	119.617(10)	$Pt1^{xvi}$—Nd2—$Pt1^{xvii}$	87.393(13)
$Pt1^{viii}$—As1—$Nd1^{i}$	146.31(7)	$Pt1^{xv}$—Nd2—$Pt1^{xviii}$	87.393(13)
$Pt1^{ix}$—As1—$Nd1^{i}$	68.93(2)	$Pt1^{xvi}$—Nd2—$Pt1^{xviii}$	74.176(18)
Pt1—As1—$Nd1^{i}$	68.93(2)	$Pt1^{xvii}$—Nd2—$Pt1^{xviii}$	132.987(6)
$Pt1^{viii}$—As1—Nd1	68.93(2)	$Pt1^{xv}$—Nd2—$Pt1^{xix}$	132.986(6)
$Pt1^{ix}$—As1—Nd1	68.93(2)	$Pt1^{xvi}$—Nd2—$Pt1^{xix}$	87.393(13)
Pt1—As1—Nd1	146.31(7)	$Pt1^{xvii}$—Nd2—$Pt1^{xix}$	87.393(13)
$Nd1^{i}$—As1—Nd1	87.14(4)	$Pt1^{xviii}$—Nd2—$Pt1^{xix}$	132.986(6)
$Pt1^{viii}$—As1—$Nd1^{ii}$	68.93(2)	$Pt1^{xv}$—Nd2—$Pt1^{xx}$	87.393(13)
$Pt1^{ix}$—As1—$Nd1^{ii}$	146.31(7)	$Pt1^{xvi}$—Nd2—$Pt1^{xx}$	132.986(6)
Pt1—As1—$Nd1^{ii}$	68.93(2)	$Pt1^{xvii}$—Nd2—$Pt1^{xx}$	132.986(6)
$Nd1^{i}$—As1—$Nd1^{ii}$	87.14(4)	$Pt1^{xviii}$—Nd2—$Pt1^{xx}$	87.393(13)
Nd1—As1—$Nd1^{ii}$	87.14(4)	$Pt1^{xix}$—Nd2—$Pt1^{xx}$	74.175(18)
$Pt1^{viii}$—As1—$Nd2^{iii}$	64.81(2)	$Pt1^{xv}$—Nd2—$As1^{xvi}$	177.79(3)
$Pt1^{ix}$—As1—$Nd2^{iii}$	137.14(7)	$Pt1^{xvi}$—Nd2—$As1^{xvi}$	46.323(7)
Pt1—As1—$Nd2^{iii}$	64.81(2)	$Pt1^{xvii}$—Nd2—$As1^{xvi}$	103.62(2)
$Nd1^{i}$—As1—$Nd2^{iii}$	133.740(3)	$Pt1^{xviii}$—Nd2—$As1^{xvi}$	94.198(16)
Nd1—As1—$Nd2^{iii}$	133.740(3)	$Pt1^{xix}$—Nd2—$As1^{xvi}$	46.324(7)
$Nd1^{ii}$—As1—$Nd2^{iii}$	76.553(3)	$Pt1^{xx}$—Nd2—$As1^{xvi}$	94.199(16)
$Pt1^{viii}$—As1—$Nd2^{vii}$	64.81(2)	$Pt1^{xv}$—Nd2—$As1^{xv}$	46.323(7)

atoms	angle(°)	atoms	angle(°)
Pt1^{ix}—As1—Nd2^{vii}	64.81(2)	Pt1^{xvi}—Nd2—As1^{xv}	177.79(3)
Pt1—As1—Nd2^{vii}	137.14(7)	Pt1^{xvii}—Nd2—As1^{xv}	94.198(16)
Nd1^{i}—As1—Nd2^{vii}	133.740(3)	Pt1^{xviii}—Nd2—As1^{xv}	103.62(2)
Nd1—As1—Nd2^{vii}	76.553(3)	Pt1^{xix}—Nd2—As1^{xv}	94.199(16)
Nd1^{ii}—As1—Nd2^{vii}	133.740(3)	Pt1^{xx}—Nd2—As1^{xv}	46.324(7)
Nd2^{iii}—As1—Nd2^{vii}	84.17(4)	As1^{xvi}—Nd2—As1^{xv}	134.470(17)
Pt1^{viii}—As1—Nd2^{v}	137.14(7)	Pt1^{xv}—Nd2—As1^{xviii}	103.62(2)
Pt1^{ix}—As1—Nd2^{v}	64.81(2)	Pt1^{xvi}—Nd2—As1^{xviii}	94.198(16)
Pt1—As1—Nd2^{v}	64.81(2)	Pt1^{xvii}—Nd2—As1^{xviii}	177.79(3)
Nd1^{i}—As1—Nd2^{v}	76.553(3)	Pt1^{xviii}—Nd2—As1^{xviii}	46.323(7)
Nd1—As1—Nd2^{v}	133.740(3)	Pt1^{xix}—Nd2—As1^{xviii}	94.199(16)
Nd1^{ii}—As1—Nd2^{v}	133.740(3)	Pt1^{xx}—Nd2—As1^{xviii}	46.324(7)
Nd2^{iii}—As1—Nd2^{v}	84.17(4)	As1^{xvi}—Nd2—As1^{xviii}	78.59(5)
Nd2^{vii}—As1—Nd2^{v}	84.17(4)	As1^{xv}—Nd2—As1^{xviii}	84.17(4)
As1^{x}—Nd1—As1^{viii}	180.000	Pt1^{xv}—Nd2—As1^{xvii}	94.198(16)
As1^{x}—Nd1—As1^{xi}	87.15(4)	Pt1^{xvi}—Nd2—As1^{xvii}	103.62(2)
As1^{viii}—Nd1—As1^{xi}	92.86(4)	Pt1^{xvii}—Nd2—As1^{xvii}	46.323(7)
As1^{x}—Nd1—As1^{ix}	92.86(4)	Pt1^{xviii}—Nd2—As1^{xvii}	177.79(3)
As1^{viii}—Nd1—As1^{ix}	87.14(4)	Pt1^{xix}—Nd2—As1^{xvii}	46.324(7)
As1^{xi}—Nd1—As1^{ix}	180.000	Pt1^{xx}—Nd2—As1^{xvii}	94.199(16)
As1^{x}—Nd1—As1^{xii}	87.14(4)	As1^{xvi}—Nd2—As1^{xvii}	84.17(4)
As1^{viii}—Nd1—As1^{xii}	92.86(4)	As1^{xv}—Nd2—As1^{xvii}	78.59(5)
As1^{xi}—Nd1—As1^{xii}	87.14(4)	As1^{xviii}—Nd2—As1^{xvii}	134.470(17)
As1^{ix}—Nd1—As1^{xii}	92.86(4)	Pt1^{xv}—Nd2—As1^{xxi}	94.199(16)
As1^{x}—Nd1—As1	92.86(4)	Pt1^{xvi}—Nd2—As1^{xxi}	46.324(7)
As1^{viii}—Nd1—As1	87.14(4)	Pt1^{xvii}—Nd2—As1^{xxi}	46.324(7)
As1^{xi}—Nd1—As1	92.86(4)	Pt1^{xviii}—Nd2—As1^{xxi}	94.199(16)

atoms	angle(°)	atoms	angle(°)
As1^{ix}—Nd1—As1	87.14(4)	Pt1^{xix}—Nd2—As1^{xxi}	103.62(2)
As1^{xii}—Nd1—As1	180.000	Pt1^{xx}—Nd2—As1^{xxi}	177.79(3)
As1^{x}—Nd1—Pt1^{viii}	133.789(9)	As1^{xvi}—Nd2—As1^{xxi}	84.17(4)
As1^{viii}—Nd1—Pt1^{viii}	46.211(9)	As1^{xv}—Nd2—As1^{xxi}	134.469(17)
As1^{xi}—Nd1—Pt1^{viii}	76.71(2)	As1^{xviii}—Nd2—As1^{xxi}	134.469(17)
As1^{ix}—Nd1—Pt1^{viii}	103.29(2)	As1^{xvii}—Nd2—As1^{xxi}	84.17(4)
As1^{xii}—Nd1—Pt1^{viii}	133.788(9)	Pt1^{xv}—Nd2—As1^{xxii}	46.324(7)
As1—Nd1—Pt1^{viii}	46.211(9)	Pt1^{xvi}—Nd2—As1^{xxii}	94.199(16)
As1^{x}—Nd1—Pt1^{x}	46.211(9)	Pt1^{xvii}—Nd2—As1^{xxii}	94.199(16)
As1^{viii}—Nd1—Pt1^{x}	133.789(9)	Pt1^{xviii}—Nd2—As1^{xxii}	46.324(7)
As1^{xi}—Nd1—Pt1^{x}	103.29(2)	Pt1^{xix}—Nd2—As1^{xxii}	177.79(3)
As1^{ix}—Nd1—Pt1^{x}	76.71(2)	Pt1^{xx}—Nd2—As1^{xxii}	103.62(2)
As1^{xii}—Nd1—Pt1^{x}	46.212(9)	As1^{xvi}—Nd2—As1^{xxii}	134.469(17)
As1—Nd1—Pt1^{x}	133.789(9)	As1^{xv}—Nd2—As1^{xxii}	84.17(4)
Pt1^{viii}—Nd1—Pt1^{x}	180.000	As1^{xviii}—Nd2—As1^{xxii}	84.17(4)
As1^{x}—Nd1—Pt1^{xi}	103.29(2)	As1^{xvii}—Nd2—As1^{xxii}	134.469(17)
As1^{viii}—Nd1—Pt1^{xi}	76.71(2)	As1^{xxi}—Nd2—As1^{xxii}	78.59(5)

Symmetry notes: (i) x, 1+y, z; (ii) -1+x, y, z; (iii) -1+x, y, -2+z; (iv) -1+x, 1+y, -2+z; (v) x, 1+y, -2+z; (vi) -1+x, 1+y, z; (vii) x, y, -2+z; (viii) x, -1+y, z; (ix) 1+x, y, z; (x) 2-x, 1-y, -4-z; (xi) 1-x, -y, -4-z; (xii) 2-x, -y, -4-z; (xiii) 1-x, 1-y, -4-z; (xiv) 1+x, -1+y, z; (xv) x, -1+y, -2.5-z; (xvi) 1+x, y, 2+z; (xvii) x, -1+y, 2+z; (xviii) 1+x, y, -2.5-z; (xix) 1+x, -1+y, 2+z; (xx) 1+x, -1+y, -2.5-z; (xxi) x, y, 2+z; (xxii) x, y, -2.5-z.

A.2 Elemental analysis of NdPtAs

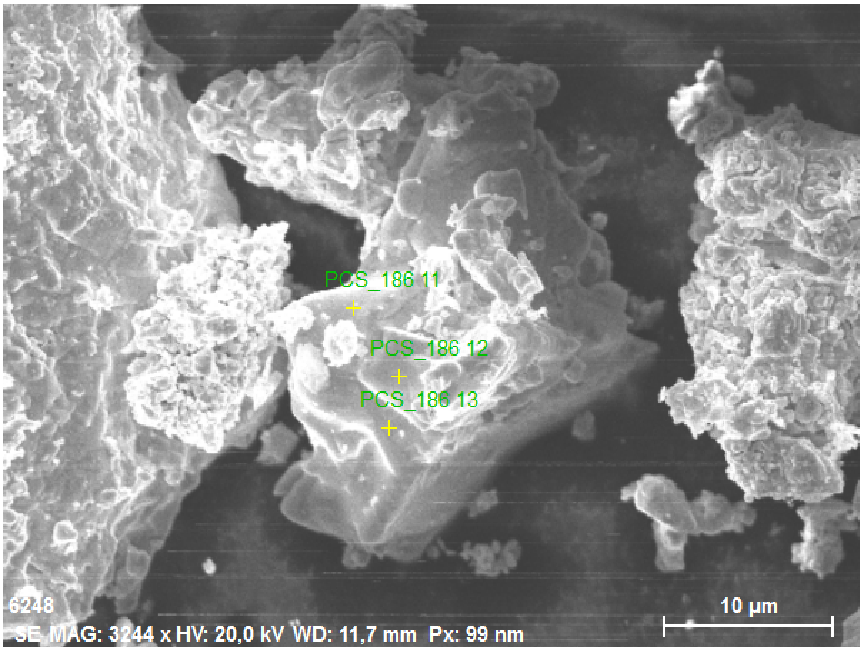

Figure A.1: Representative scanning electron microscopic photographs of NdPtAs

Table A.3: Elemental analysis by EDX of NdPtAs, signals of oxygen were not taken into account due to hydrolysis.

Spektrum	As	Nd	Pt
EDX point 11 / atom-%	38,07	21,25	40,68
EDX point 12 / atom-%	35,91	22,21	41,89
EDX point 13 / atom-%	37,75	21,44	40,81
Average / atom-%	37,24	21,63	41,13
Calculated / atom-%	33.3	33.3	33.3

Appendix B

Supporting Information for Chapter 3

B.1 Crystallographic Data of ***AE*AuPb (*AE* = Sr, Ba, Ca)**

Table B.1: Anisotropic Displacement Parameters (Å^2) of SrAuPb from single crystal data.

Atom	U_{11}	U_{22}	U_{33}	U_{12}	U_{13}	U_{23}
Pb1	0.0081(6)	0.0226(7)	0.0097(6)	0.000	0.000	0.0002(3)
Au1	0.0081(6)	0.0226(7)	0.0097(6)	0.000	0.000	0.0002(3)
Sr1	0.0146(14)	0.0114(12)	0.0144(13)	0.000	0.000	0.000

Table B.2: Selected angle (°) in SrAuPb.

atoms	angle(°)	atoms	angle(°)
Au1|Pb1—Au1|Pb1—Au1|Pb1	119.37(5)	Au1|Pb1—Au1|Pb1—Au1|Pb1	119.44(3)
Au1|Pb1—Au1|Pb1—Au1|Pb1	119.44(3)	Au1|Pb1—Au1|Pb1—Au1|Pb1	90.000
Au1|Pb1—Au1|Pb1—Au1|Pb1	90.000	Au1|Pb1—Au1|Pb1—Au1|Pb1	103.16(4)
Au1|Pb1—Au1|Pb1—Sr1	68.13(4)	Au1|Pb1—Au1|Pb1—Sr1	151.13(2)
Au1|Pb1—Au1|Pb1—Sr1	67.88(5)	Au1|Pb1—Au1|Pb1—Sr1	61.43(2)

atoms	angle(°)	atoms	angle(°)
Au1|Pb1—Au1|Pb1—Sr1	151.13(2)	Au1|Pb1—Au1|Pb1—Sr1	68.13(4)
Au1|Pb1—Au1|Pb1—Sr1	67.88(5)	Au1|Pb1—Au1|Pb1—Sr1	61.43(2)
Sr1—Au1|Pb1—Sr1	92.60(6)	Au1|Pb1—Au1|Pb1—Sr1	67.92(3)
Au1|Pb1—Au1|Pb1—Sr1	67.92(3)	Au1|Pb1—Au1|Pb1—Sr1	124.98(6)
Au1|Pb1—Au1|Pb1—Sr1	131.85(4)	Sr1—Au1|Pb1—Sr1	133.67(3)
Sr1—Au1|Pb1—Sr1	133.67(3)	Au1|Pb1—Au1|Pb1—Sr1	63.39(3)
Au1|Pb1—Au1|Pb1—Sr1	63.39(3)	Au1|Pb1—Au1|Pb1—Sr1	165.73(6)
Au1|Pb1—Au1|Pb1—Sr1	62.56(3)	Sr1—Au1|Pb1—Sr1	102.83(6)
Sr1—Au1|Pb1—Sr1	102.83(6)	Sr1—Au1|Pb1—Sr1	69.290(19)
Au1|Pb1—Au1|Pb1—Sr1	139.40(3)	Au1|Pb1—Au1|Pb1—Sr1	63.78(4)
Au1|Pb1—Au1|Pb1—Sr1	63.05(5)	Au1|Pb1—Au1|Pb1—Sr1	130.23(2)
Sr1—Au1|Pb1—Sr1	130.93(2)	Sr1—Au1|Pb1—Sr1	69.47(2)
Sr1—Au1|Pb1—Sr1	78.65(7)	Sr1—Au1|Pb1—Sr1	125.21(6)
Au1|Pb1—Au1|Pb1—Sr1	63.78(4)	Au1|Pb1—Au1|Pb1—Sr1	139.40(3)
Au1|Pb1—Au1|Pb1—Sr1	63.05(5)	Au1|Pb1—Au1|Pb1—Sr1	130.24(2)
Sr1—Au1|Pb1—Sr1	69.47(2)	Sr1—Au1|Pb1—Sr1	130.93(2)
Sr1—Au1|Pb1—Sr1	78.65(7)	Sr1—Au1|Pb1—Sr1	125.21(6)
Sr1—Au1|Pb1—Sr1	88.16(4)	Au1|Pb1—Sr1—Au1|Pb1	57.15(4)
Au1|Pb1—Sr1—Au1|Pb1	120.19(10)^{i}	Au1|Pb1—Sr1—Au1|Pb1	92.60(6)^{ii}
Au1|Pb1—Sr1—Au1|Pb1	57.15(4)	Au1|Pb1—Sr1—Au1|Pb1	133.67(3)^{iii}
Au1|Pb1—Sr1—Au1|Pb1	92.995(15)^{iv}	Au1|Pb1—Sr1—Au1|Pb1	83.71(8)
Au1|Pb1—Sr1—Au1|Pb1	48.48(4)^{v}	Au1|Pb1—Sr1—Au1|Pb1	77.17(6)^{vi}
Au1|Pb1—Sr1—Au1|Pb1	165.58(7)^{vii}	Au1|Pb1—Sr1—Au1|Pb1	110.70(1)^{viii}
Au1|Pb1—Sr1—Au1|Pb1	54.87(6)	Au1|Pb1—Sr1—Au1|Pb1	165.60(8)^{vii}
Au1|Pb1—Sr1—Au1|Pb1	110.530(16)^{viii}	Au1|Pb1—Sr1—Au1|Pb1	49.07(2)^{ix}
Au1|Pb1—Sr1—Au1|Pb1	87.866(15)^{x}	Au1|Pb1—Sr1—Au1|Pb1	48.31(3)^{xi}
Au1|Pb1—Sr1—Au1|Pb1	101.35(7)^{xii}	Au1|Pb1—Sr1—Au1|Pb1	125.21(6)^{xiii}

atoms	angle(°)	atoms	angle(°)
Au1|Pb1—Sr1—Au1|Pb1	88.93(3)^{xiv}	Au1|Pb1—Sr1—Au1|Pb1	143.36(10)
Au1|Pb1—Sr1—Au1|Pb1	80.47(4)	Au1|Pb1—Sr1—Au1|Pb1	88.16(4)

Symmetry notes: (i) x, y, z; (ii) $-x, -y+\frac{1}{2}, z$; (iii) $-x, y+\frac{1}{2}, -z$; (iv) $x, -y, -z$; (v) $x+\frac{1}{2}, y+\frac{1}{2}, z+\frac{1}{2}$; (vi) $-x+\frac{1}{2}, -y+1, z+\frac{1}{2}$; (vii) $-x+\frac{1}{2}, y+1, -z+\frac{1}{2}$; (viii) $x+\frac{1}{2}, -y+\frac{1}{2}, -z+\frac{1}{2}$; (ix) $-x, -y, -z$; (x) $x, y-\frac{1}{2}, -z$; (xi) $x, -y-\frac{1}{2}, z$; (xii) $-x, y, z$; (xiii) $-x+\frac{1}{2}, -y+\frac{1}{2}, -z+\frac{1}{2}$; (xiv) $x+\frac{1}{2}, y, -z+\frac{1}{2}$; (xv) $x+\frac{1}{2}, -y, z+\frac{1}{2}$; (xvi) $-x+\frac{1}{2}, y+\frac{1}{2}, z+\frac{1}{2}$.

B.2 Magnetization isotherms of $\boldsymbol{AE}$AuPb ($\boldsymbol{AE}$ = Ca, Sr, Ba)

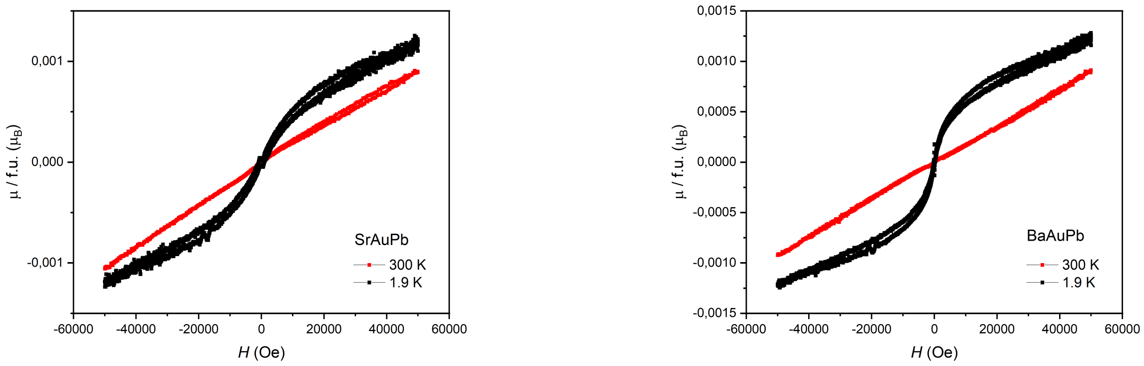

(a) SrAuPb

(b) BaAuPb

Figure B.1: Magnetization isotherms of (a) SrAuPb and (b) BaAuPb measured at 1.9 and 300K with fields up to 50 kOe

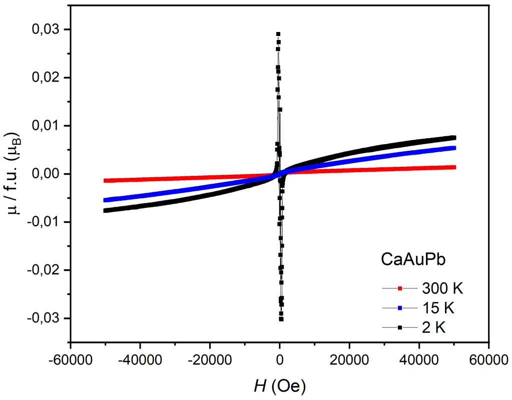

Figure B.2: Magnetization isotherms of CaAuPb measured at 2K, 15K and 300K with fields up to 50 kOe

Appendix C

Supporting Information for Chapter 4

C.1 Crystallographic Data of (Eu, Sr)PtPb

Table C.1: Anisotropic Displacement Parameters (Å^2) of SrPtPb from single crystal data.

Atom	U_{11}	U_{22}	U_{33}	U_{12}	U_{13}	U_{23}
Sr1	0.0085(4)	0.0120(3)	0.0116(3)	0	-0.0006(2)	0
Pb1	0.00966(19)	0.00956(17)	0.01004(17)	0	-0.00051(9)	0
Pt1	0.00995(19)	0.01047(18)	0.01218(18)	0	0.00134(10)	0

Table C.2: Anisotropic Displacement Parameters (Å^2) of EuPtPb from single crystal data.

Atom	U_{11}	U_{22}	U_{33}	U_{12}	U_{13}	U_{23}
Pb1	0.0138(4)	0.0061(4)	0.0098(4)	0	-0.0005(2)	0
Pt1	0.0128(4)	0.0068(4)	0.0119(4)	0	-0.0013(3)	0
Eu1	0.0121(5)	0.0084(5)	0.0120(6)	0	0.0009(3)	0

Table C.3: Selected angle (°) in SrPtPb.

atoms	angle(°)	atoms	angle(°)
Pb1—Pt1—Pb1	122.051(11)	Pb1—Pt1—Pb1	122.051(11)
Pb1—Pt1—Pb1	115.42(2)	Pb1—Pt1—Pb1	113.23(2)
Pb1—Pt1—Pb1	81.208(19)	Pb1—Pt1—Pb1	81.208(19)
Pb1—Pt1—Sr3	120.10(3)	Pb1—Pt1—Sr3	71.382(16)
Pb1—Pt1—Sr3	71.382(16)	Pb1—Pt1—Sr3	126.67(3)
Pb1—Pt1—Sr3	69.70(2)	Pb1—Pt1—Sr3	146.34(3)
Pb1—Pt1—Sr3	66.990(19)	Pb1—Pt1—Sr3	65.69(2)
Sr3—Pt1—Sr3	133.656(16)	Pb1—Pt1—Sr3	69.70(2)
Pb1—Pt1—Sr3	66.990(19)	Pb1—Pt1—Sr3	146.34(3)
Pb1—Pt1—Sr3	65.69(2)	Sr3—Pt1—Sr3	133.656(16)
Sr3—Pt1—Sr3	92.69(3)	Pb1—Pt1—Sr3	64.81(2)
Pb1—Pt1—Sr3	141.24(2)	Pb1—Pt1—Sr3	66.490(19)
Pb1—Pt1—Sr3	134.268(14)	Sr3—Pt1—Sr3	73.40(3)
Sr3—Pt1—Sr3	72.081(11)	Sr3—Pt1—Sr3	134.515(19)
Pb1—Pt1—Sr3	64.81(2)	Pb1—Pt1—Sr3	66.490(19)
Pb1—Pt1—Sr3	141.24(2)	Pb1—Pt1—Sr3	134.268(14)
Sr3—Pt1—Sr3	73.40(3)	Sr3—Pt1—Sr3	134.515(19)
Sr3—Pt1—Sr3	72.081(10)	Sr3—Pt1—Sr3	88.40(3)
Pb1—Pt1—Sr3	171.96(3)	Pb1—Pt1—Sr3	58.877(12)
Pb1—Pt1—Sr3	58.877(12)	Pb1—Pt1—Sr3	58.74(2)
Sr3—Pt1—Sr3	67.936(11)	Sr3—Pt1—Sr3	105.07(2)
Sr3—Pt1—Sr3	105.07(2)	Sr3—Pt1—Sr3	120.14(3)
Sr3—Pt1—Sr3	120.14(3)	Pt1—Pb1—Pt1	117.066(12)
Pt1—Pb1—Pt1	117.066(12)	Pt1—Pb1—Pt1	115.42(2)
Pt1—Pb1—Pt1	104.972(18)	Pt1—Pb1—Pt1	98.792(19)

atoms	angle(°)	atoms	angle(°)
Pt1—Pb1—Pt1	98.792(19)	Pt1—Pb1—Sr3	66.24(2)
Pt1—Pb1—Sr3	160.51(2)	Pt1—Pb1—Sr3	75.560(18)
Pt1—Pb1—Sr3	62.640(19)	Pt1—Pb1—Sr3	66.24(2)
Pt1—Pb1—Sr3	75.560(18)	Pt1—Pb1—Sr3	160.51(2)
Pt1—Pb1—Sr3	62.640(19)	Sr3—Pb1—Sr3	89.67(3)
Pt1—Pb1—Sr3	179.17(3)	Pt1—Pb1—Sr3	63.199(12)
Pt1—Pb1—Sr3	63.199(12)	Pt1—Pb1—Sr3	74.20(3)
Sr3—Pb1—Sr3	113.23(2)	Sr3—Pb1—Sr3	113.23(2)
Pt1—Pb1—Sr3	110.43(3)	Pt1—Pb1—Sr3	65.093(15)
Pt1—Pb1—Sr3	65.094(15)	Pt1—Pb1—Sr3	144.60(3)
Sr3—Pb1—Sr3	133.429(12)	Sr3—Pb1—Sr3	133.429(12)
Sr3—Pb1—Sr3	70.400(14)	Pt1—Pb1—Sr3	61.54(2)
Pt1—Pb1—Sr3	59.13(2)	Pt1—Pb1—Sr3	129.31(2)
Pt1—Pb1—Sr3	131.574(17)	Sr3—Pb1—Sr3	127.780(16)
Sr3—Pb1—Sr3	69.895(10)	Sr3—Pb1—Sr3	118.98(3)
Sr3—Pb1—Sr3	69.03(3)	Pt1—Pb1—Sr3	61.54(2)
Pt1—Pb1—Sr3	129.31(2)	Pt1—Pb1—Sr3	59.13(2)
Pt1—Pb1—Sr3	131.574(17)	Sr3—Pb1—Sr3	69.895(10)
Sr3—Pb1—Sr3	127.780(16)	Sr3—Pb1—Sr3	118.98(3)
Sr3—Pb1—Sr3	69.03(3)	Sr3—Pb1—Sr3	85.41(3)
Pt1—Sr3—Pt1	95.83(2)	Pt1—Sr3—Pt1	95.83(2)
Pt1—Sr3—Pt1	92.69(3)	Pt1—Sr3—Pb1	134.984(15)
Pt1—Sr3—Pb1	51.671(15)	Pt1—Sr3—Pb1	113.58(4)
Pt1—Sr3—Pb1	134.984(15)	Pt1—Sr3—Pb1	113.58(4)
Pt1—Sr3—Pb1	51.671(15)	Pb1—Sr3—Pb1	89.67(3)
Pt1—Sr3—Pb1	119.27(4)	Pt1—Sr3—Pb1	49.811(18)
Pt1—Sr3—Pb1	49.811(18)	Pb1—Sr3—Pb1	66.77(2)

atoms	angle(°)	atoms	angle(°)
Pb1—Sr3—Pb1	66.77(2)	Pt1—Sr3—Pt1	106.60(3)
Pt1—Sr3—Pt1	157.57(4)	Pt1—Sr3—Pt1	85.157(10)
Pb1—Sr3—Pt1	109.05(3)	Pb1—Sr3—Pt1	48.953(13)
Pb1—Sr3—Pt1	115.72(3)	Pt1—Sr3—Pt1	106.60(3)
Pt1—Sr3—Pt1	85.157(10)	Pt1—Sr3—Pt1	157.57(4)
Pb1—Sr3—Pt1	48.953(13)	Pb1—Sr3—Pt1	109.05(3)
Pb1—Sr3—Pt1	115.72(3)	Pt1—Sr3—Pt1	88.40(3)
Pt1—Sr3—Pb1	91.27(3)	Pt1—Sr3—Pb1	132.874(16)
Pt1—Sr3—Pb1	132.874(15)	Pb1—Sr3—Pb1	92.31(2)
Pb1—Sr3—Pb1	92.31(2)	Pb1—Sr3—Pb1	149.46(4)
Pt1—Sr3—Pb1	48.416(15)	Pt1—Sr3—Pb1	48.416(15)
Pt1—Sr3—Pb1	49.489(15)	Pt1—Sr3—Pb1	48.752(14)
Pt1—Sr3—Pb1	108.79(3)	Pb1—Sr3—Pb1	87.809(10)
Pb1—Sr3—Pb1	156.66(4)	Pb1—Sr3—Pb1	91.02(2)
Pt1—Sr3—Pb1	152.17(4)	Pt1—Sr3—Pb1	86.487(12)
Pb1—Sr3—Pb1	110.97(3)	Pt1—Sr3—Pb1	49.489(15)
Pt1—Sr3—Pb1	108.79(3)	Pt1—Sr3—Pb1	48.752(14)
Pb1—Sr3—Pb1	156.66(4)	Pb1—Sr3—Pb1	87.809(10)
Pb1—Sr3—Pb1	91.02(2)	Pt1—Sr3—Pb1	86.487(12)
Pt1—Sr3—Pb1	152.17(4)	Pb1—Sr3—Pb1	110.97(3)
Pb1—Sr3—Pb1	85.41(3)	Pt1—Sr3—Pt1	166.33(4)
Pt1—Sr3—Pt1	74.93(2)	Pt1—Sr3—Pt1	74.93(2)
Pb1—Sr3—Pt1	45.563(17)	Pb1—Sr3—Pt1	45.563(17)
Pb1—Sr3—Pt1	47.068(18)	Pt1—Sr3—Pt1	82.98(2)
Pt1—Sr3—Pt1	82.98(2)	Pb1—Sr3—Pt1	102.40(3)
Pb1—Sr3—Pt1	123.37(2)	Pb1—Sr3—Pt1	123.37(2)

Symmetry notes: (i) x, y, z; (ii) $-x+\frac{1}{2}, -y, z+\frac{1}{2}$; (iii) $-x, y+\frac{1}{2}, -z$; (iv) $x+\frac{1}{2}, -y-\frac{1}{2}, -z-\frac{1}{2}$;

(v) $-x, -y, -z$; (vi) $x - \frac{1}{2}, y, -z - \frac{1}{2}$; (vii) $x, -y - \frac{1}{2}, z$; (viii) $-x - \frac{1}{2}, y - \frac{1}{2}, z - \frac{1}{2}$.

Table C.4: Selected angle (°) in EuPtPb.

atoms	angle(°)	atoms	angle(°)
Pt01—Pb01—Pt01	117.22(2)	Pt01—Pb01—Pt01	117.22(2)
Pt01—Pb01—Pt01	115.10(4)	Pt01—Pb01—Pt01	103.70(3)
Pt01—Pb01—Pt01	99.46(3)	Pt01—Pb01—Pt01	99.46(3)
Pt01—Pb01—Eu01	65.44(2)	Pt01—Pb01—Eu01	161.05(3)
Pt01—Pb01—Eu01	75.96(2)	Pt01—Pb01—Eu01	62.55(2)
Pt01—Pb01—Eu01	65.44(2)	Pt01—Pb01—Eu01	75.96(2)
Pt01—Pb01—Eu01	161.05(3)	Pt01—Pb01—Eu01	62.55(2)
Eu01—Pb01—Eu01	89.52(3)	Pt01—Pb01—Eu01	178.45(4)
Pt01—Pb01—Eu01	63.28(2)	Pt01—Pb01—Eu01	63.28(2)
Pt01—Pb01—Eu01	74.76(3)	Eu01—Pb01—Eu01	113.57(3)
Eu01—Pb01—Eu01	113.57(3)	Pt01—Pb01—Eu01	111.80(3)
Pt01—Pb01—Eu01	64.51(2)	Pt01—Pb01—Eu01	64.51(2)
Pt01—Pb01—Eu01	144.51(4)	Eu01—Pb01—Eu01	133.543(13)
Eu01—Pb01—Eu01	133.543(13)	Eu01—Pb01—Eu01	69.751(18)
Pt01—Pb01—Eu01	62.01(2)	Pt01—Pb01—Eu01	58.74(3)
Pt01—Pb01—Eu01	129.38(3)	Pt01—Pb01—Eu01	130.87(2)
Eu01—Pb01—Eu01	127.45(3)	Eu01—Pb01—Eu01	69.247(13)
Eu01—Pb01—Eu01	118.97(3)	Eu01—Pb01—Eu01	69.82(3)
Pt01—Pb01—Eu01	62.01(2)	Pt01—Pb01—Eu01	129.38(3)
Pt01—Pb01—Eu01	58.74(2)	Pt01—Pb01—Eu01	130.87(2)
Eu01—Pb01—Eu01	69.247(13)	Eu01—Pb01—Eu01	127.45(3)
Eu01—Pb01—Eu01	118.97(3)	Eu01—Pb01—Eu01	69.82(3)
Eu01—Pb01—Eu01	86.22(3)	Pt01—Pb01—Pb01	122.28(3)

atoms	angle(°)	atoms	angle(°)
Pt01—Pb01—Pb01	116.86(4)	Pt01—Pb01—Pb01	50.80(2)
Pt01—Pb01—Pb01	48.65(2)	Eu01—Pb01—Pb01	56.86(2)
Eu01—Pb01—Pb01	110.96(3)	Eu01—Pb01—Pb01	56.72(3)
Eu01—Pb01—Pb01	108.19(3)	Eu01—Pb01—Pb01	175.57(4)
Eu01—Pb01—Pb01	96.848(16)	Pt01—Pb01—Pb01	122.28(3)
Pt01—Pb01—Pb01	50.80(2)	Pt01—Pb01—Pb01	116.86(4)
Pt01—Pb01—Pb01	48.65(2)	Eu01—Pb01—Pb01	110.96(3)
Eu01—Pb01—Pb01	56.86(2)	Eu01—Pb01—Pb01	56.72(2)
Eu01—Pb01—Pb01	108.19(3)	Eu01—Pb01—Pb01	96.848(16)
Eu01—Pb01—Pb01	175.57(4)	Pb01—Pb01—Pb01	79.92(3)
Pb01—Pt01—Pb01	122.335(19)	Pb01—Pt01—Pb01	122.335(19)
Pb01—Pt01—Pb01	115.10(4)	Pb01—Pt01—Pb01	112.41(3)
Pb01—Pt01—Pb01	80.54(3)	Pb01—Pt01—Pb01	80.54(3)
Pb01—Pt01—Eu01	122.32(4)	Pb01—Pt01—Eu01	71.20(2)
Pb01—Pt01—Eu01	71.20(2)	Pb01—Pt01—Eu01	125.27(4)
Pb01—Pt01—Eu01	69.14(3)	Pb01—Pt01—Eu01	145.70(4)
Pb01—Pt01—Eu01	66.77(2)	Pb01—Pt01—Eu01	65.71(2)
Eu01—Pt01—Eu01	133.666(18)	Pb01—Pt01—Eu01	69.14(3)
Pb01—Pt01—Eu01	66.77(2)	Pb01—Pt01—Eu01	145.70(4)
Pb01—Pt01—Eu01	65.71(2)	Eu01—Pt01—Eu01	133.666(18)
Eu01—Pt01—Eu01	92.64(3)	Pb01—Pt01—Eu01	65.49(3)
Pb01—Pt01—Eu01	66.59(2)	Pb01—Pt01—Eu01	142.33(4)
Pb01—Pt01—Eu01	133.678(17)	Eu01—Pt01—Eu01	74.64(3)
Eu01—Pt01—Eu01	134.63(3)	Eu01—Pt01—Eu01	71.560(13)
Pb01—Pt01—Eu01	65.49(3)	Pb01—Pt01—Eu01	142.33(4)
Pb01—Pt01—Eu01	66.59(2)	Pb01—Pt01—Eu01	133.678(17)
Eu01—Pt01—Eu01	74.64(3)	Eu01—Pt01—Eu01	71.560(13)

atoms	angle(°)	atoms	angle(°)
Eu01—Pt01—Eu01	134.63(3)	Eu01—Pt01—Eu01	89.56(3)
Pb01—Pt01—Eu01	170.66(4)	Pb01—Pt01—Eu01	58.61(2)
Pb01—Pt01—Eu01	58.61(2)	Pb01—Pt01—Eu01	58.25(3)
Eu01—Pt01—Eu01	67.015(17)	Eu01—Pt01—Eu01	104.79(3)
Eu01—Pt01—Eu01	104.79(3)	Eu01—Pt01—Eu01	120.18(3)
Eu01—Pt01—Eu01	120.18(3)	Pt01—Eu01—Pt01	96.52(2)
Pt01—Eu01—Pt01	92.64(3)	Pt01—Eu01—Pt01	105.36(3)
Pt01—Eu01—Pt01	158.11(4)	Pt01—Eu01—Pt01	84.781(15)
Pt01—Eu01—Pt01	105.36(3)	Pt01—Eu01—Pt01	84.781(15)
Pt01—Eu01—Pt01	158.11(4)	Pt01—Eu01—Pt01	89.56(3)
Pt01—Eu01—Pb01	135.134(16)	Pt01—Eu01—Pb01	113.53(4)
Pt01—Eu01—Pb01	51.73(2)	Pt01—Eu01—Pb01	49.07(2)
Pt01—Eu01—Pb01	109.68(3)	Pt01—Eu01—Pb01	135.134(16)
Pt01—Eu01—Pb01	51.73(2)	Pt01—Eu01—Pb01	113.53(4)
Pt01—Eu01—Pb01	109.68(3)	Pt01—Eu01—Pb01	49.07(2)
Pb01—Eu01—Pb01	89.52(3)	Pt01—Eu01—Pb01	120.78(4)
Pt01—Eu01—Pb01	49.95(2)	Pt01—Eu01—Pb01	49.95(2)
Pt01—Eu01—Pb01	115.48(3)	Pt01—Eu01—Pb01	115.48(3)
Pb01—Eu01—Pb01	66.43(3)	Pb01—Eu01—Pb01	66.43(3)
Pt01—Eu01—Pb01	89.77(3)	Pt01—Eu01—Pb01	132.974(17)
Pt01—Eu01—Pb01	132.974(17)	Pt01—Eu01—Pb01	48.895(18)
Pt01—Eu01—Pb01	48.895(18)	Pb01—Eu01—Pb01	92.65(2)
Pb01—Eu01—Pb01	92.65(2)	Pb01—Eu01—Pb01	149.45(4)
Pt01—Eu01—Pb01	50.055(19)	Pt01—Eu01—Pb01	48.85(2)
Pt01—Eu01—Pb01	109.30(3)	Pt01—Eu01—Pb01	151.68(4)
Pt01—Eu01—Pb01	85.269(17)	Pb01—Eu01—Pb01	157.10(4)
Pb01—Eu01—Pb01	87.638(15)	Pb01—Eu01—Pb01	91.72(2)

atoms	angle(°)	atoms	angle(°)
Pb01—Eu01—Pb01	110.18(3)	Pt01—Eu01—Pb01	50.055(19)
Pt01—Eu01—Pb01	109.30(3)	Pt01—Eu01—Pb01	48.85(2)
Pt01—Eu01—Pb01	85.269(18)	Pt01—Eu01—Pb01	151.68(4)
Pb01—Eu01—Pb01	87.638(15)	Pb01—Eu01—Pb01	157.10(4)
Pb01—Eu01—Pb01	91.72(2)	Pb01—Eu01—Pb01	110.18(3)
Pb01—Eu01—Pb01	86.22(3)	Pt01—Eu01—Pt01	167.77(4)
Pt01—Eu01—Pt01	75.21(3)	Pt01—Eu01—Pt01	75.21(3)
Pt01—Eu01—Pt01	83.14(2)	Pt01—Eu01—Pt01	83.14(2)
Pb01—Eu01—Pt01	45.423(17)	Pb01—Eu01—Pt01	45.423(17)
Pb01—Eu01—Pt01	46.99(2)	Pb01—Eu01—Pt01	102.46(3)
Pb01—Eu01—Pt01	123.63(3)	Pb01—Eu01—Pt01	123.63(3)

Symmetry notes: (i) x, y, z; (ii) $\frac{3}{2}-x, 1-y, \frac{1}{2}+z$; (iii) $\frac{3}{2}-x, -y, \frac{1}{2}+z$; (iv) $-\frac{1}{2}+x, y, \frac{3}{2}-z$; (v) $1-x, -y, 1-z$; (vi) $1-x, 1-y, 1-z$; (vii) $x, y, 1+z$; (viii) $\frac{1}{2}+x, y, \frac{3}{2}-z$; (ix) $\frac{3}{2}-x, 1-y, \frac{1}{2}+z$; (x) $\frac{3}{2}-x, -y, \frac{1}{2}+z$; (xi) $1-x, -y, 2-z$; (xii) $1-x, 1-y, 2-z$; (xiii) $\frac{3}{2}-x, 1-y, \frac{1}{2}+z$; (xiv) $\frac{3}{2}-x, -y, \frac{1}{2}+z$; (xv) $1-x, -y, 1-z$; (xvi) $1-x, 1-y, 1-z$; (xvii) $\frac{1}{2}+x, y, \frac{1}{2}-z$; (xviii) x, y, z.

C.2 Magnetic measurement of EuPtPb

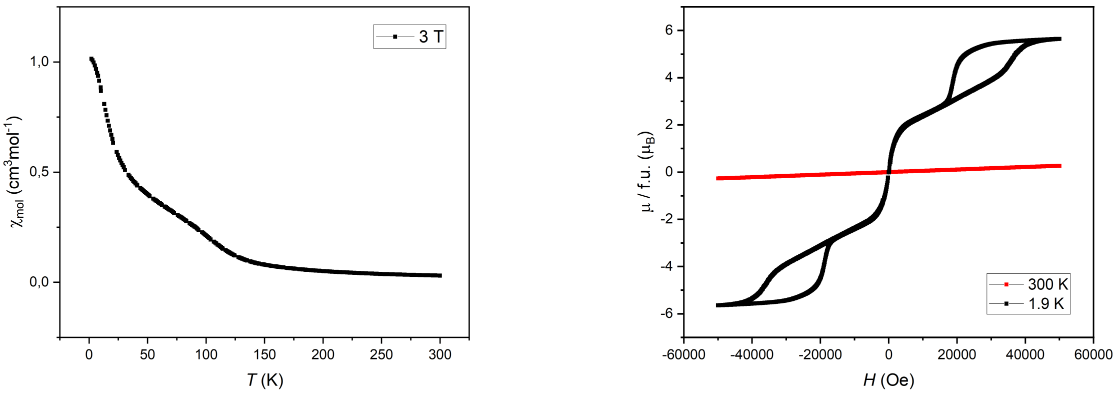

(a) (b)

Figure C.1: Temperature dependence of magnetic susceptibility of EuPtPb measured under 2.9 to 300K in the zero-field-cooled/field-cooled (ZFC/FC) mode with an applied field of 3T (left). Magnetization isotherms of EuPtPb, measured at 1.9 K and 300 K with fields up to 50 kOe (right).

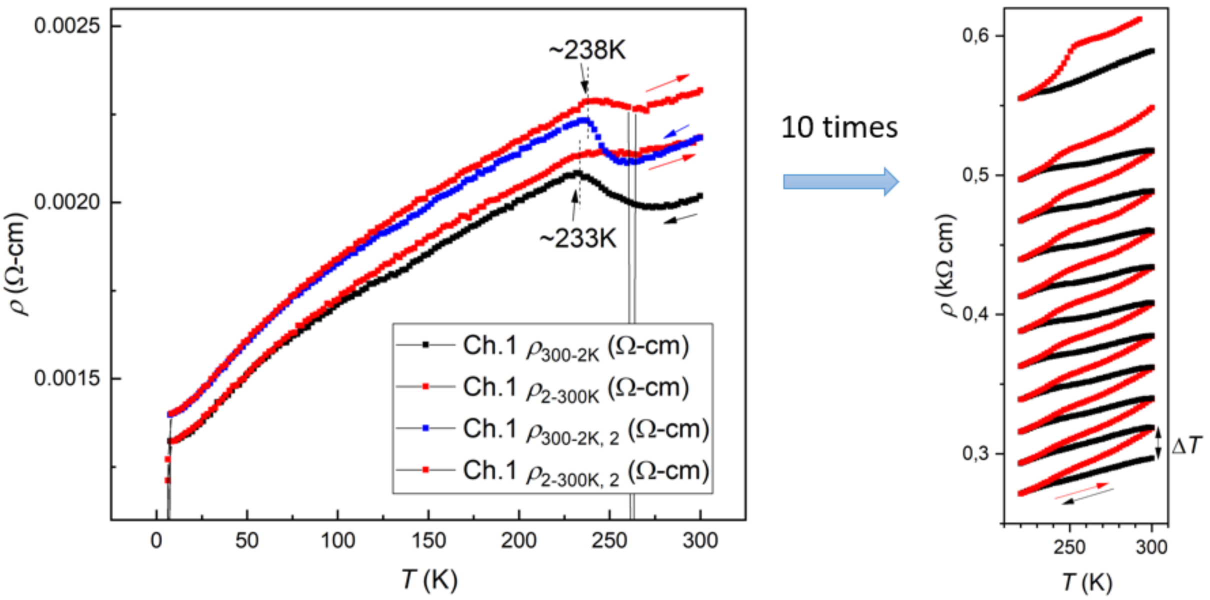

Figure C.2: Temperature dependence of the specific resistivity of SrPtPb measured ten times between 220 K and 300 K. The resistivity splitting consistently appears in all runs, indicating a reproducible feature of the material.

Additional measurements performed in the reverse warming sequence (3–300 K), reveal a small resistivity anomaly near 275 K with almost no hysteresis between warming and cooling. Such high-temperature anomalies are characteristic of first-order phase transitions for EuPtP. To further investigate the origin and reproducibility of this anomaly, we conducted ten successive resistivity measurements in the temperature range 220–300 K. These results are shown in Figure C.2 and the corresponding resistivity differences between the warming and cooling cycles are plotted in Figure C.3. With repeated cycling, a progressive increase in the resistivity split is observed, which may be related to extrinsic factors such as grain-boundary scattering or surface effects during measurement.

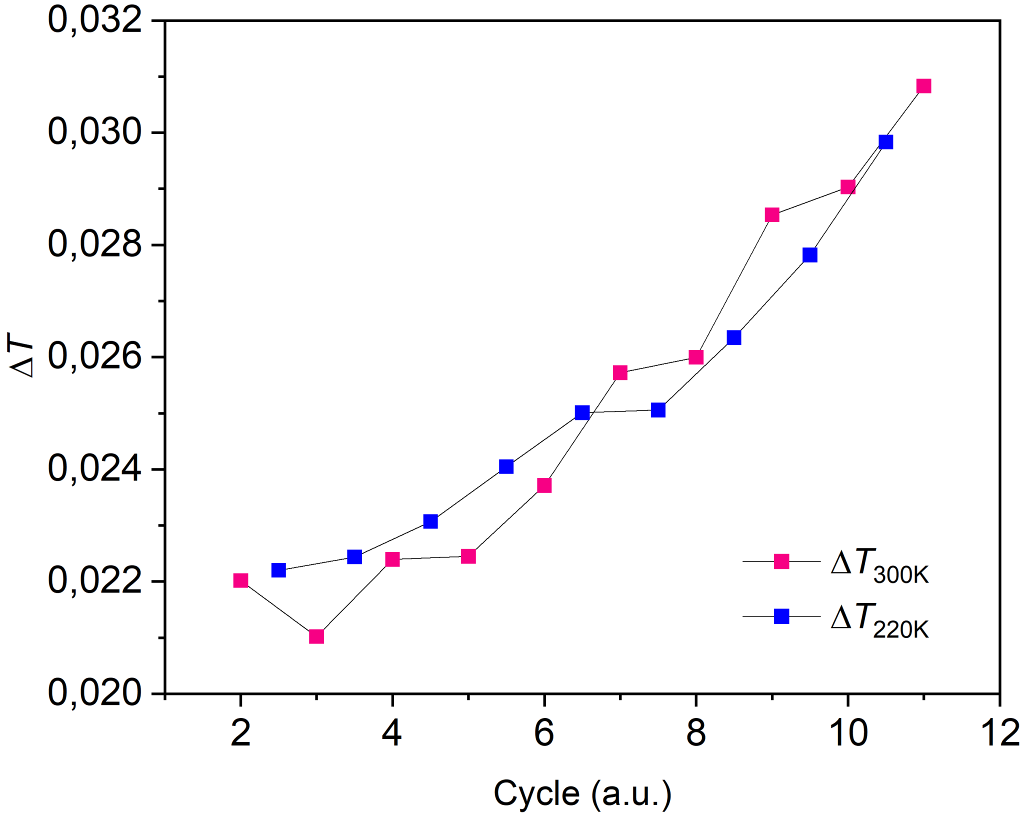

Figure C.3: Difference in resistivity at 300 K between cooling (300 K to 220 K) and warming (220 K to 300 K) cycles of SrPtPb, showing reproducible hysteresis behavior.

C.3 High temperature powder X-ray diffraction pattern of EuPtPb

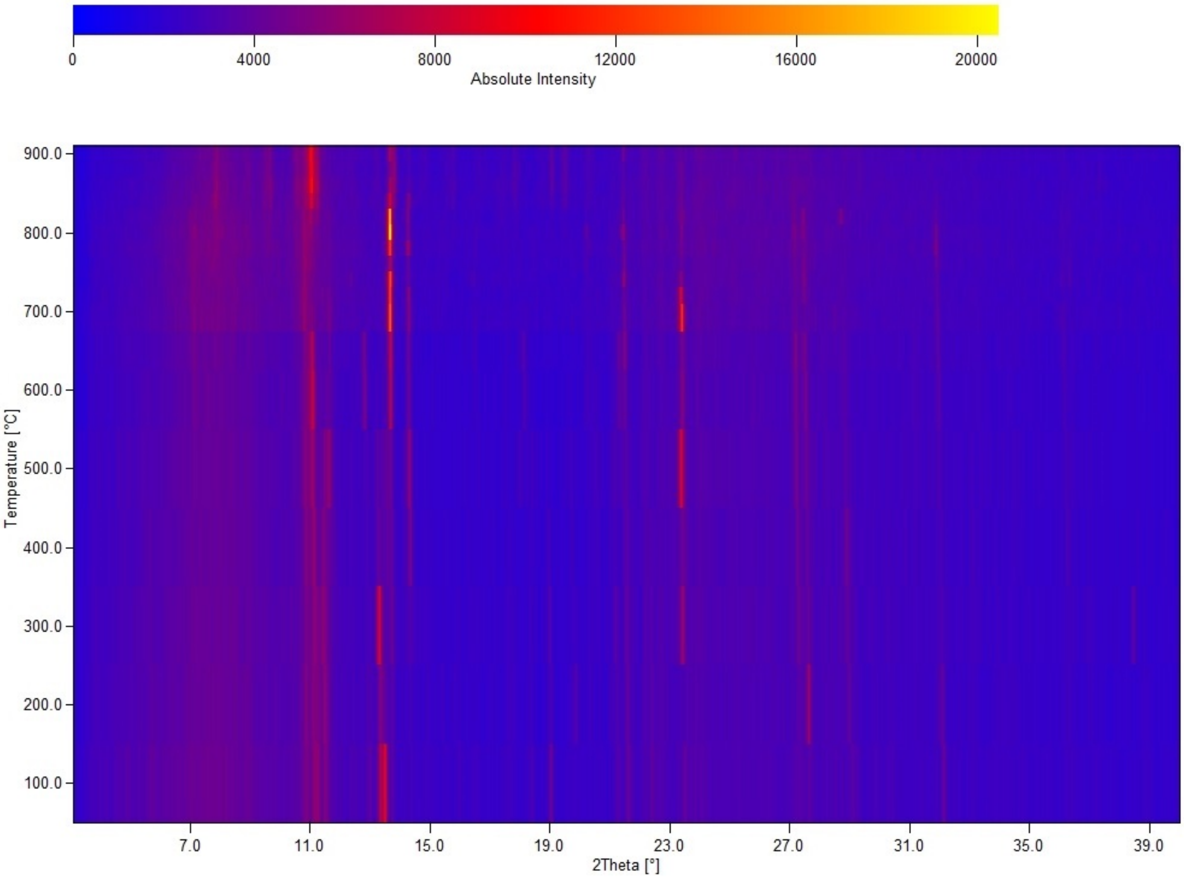

Figure C.4: High temperature powder X-ray diffraction patterns Ag $K\alpha1$ of EuPtPb between 100 K and 900K.

Appendix D

Supporting Information for Chapter 5

D.1 Experimental procedure

D.1.1 Experimental procedure

$RbSi_2P_3$ was synthesized as an air-sensitive, dark red polycrystalline powder by direct reaction of the elements. Metallic rubidium (purity 99.75%), silicon powder (99.999%), and red phosphorus (99.999%) were weighed in an argon-filled glovebox, loaded into an aluminum crucible, and sealed in silica ampoules under argon atmosphere. To prevent bursting of the ampoules, the temperature was raised slowly to 750 °C at a rate of 20 °C/h. The mixture was subsequently heated to 1040 °C and kept at this temperature for 60 h. The furnace was then cooled to room temperature at a rate of 40 °C/h, yielding $RbSi_2P_3$ as the main product.

For substitution experiments, silicon was partially replaced by aluminum or gallium according to the nominal compositions $Rb_{1+x}Si_{2-x}M_xP_3$ (M = Al, Ga; x = 0.02–0.20). The mixtures were prepared directly from the elements in the glovebox, loaded and sealed in the same manner, and subjected to the identical heating program as used for the parent $RbSi_2P_3$.

D.1.2 X-ray powder and Single Crystal Data

X-ray powder diffraction patterns were recorded using a Stadi-P diffractometer (STOE & Cie GmbH, Darmstadt, Germany, Ag $K\alpha$ radiation, $\lambda = 0.56\,\text{Å}$). Rietveld refinements based on structure models from single-crystal diffraction were performed using the TOPAS software. Single-crystal X-ray data for $RbSi_2P_3$ were collected on a Bruker D8 Quest diffractometer with a Mo$K\alpha$ microfocus source, Göbel mirror optics, and a Photon II detector. APEX3 was used for data reduction and absorption correction. Space group determination was carried out with XPREP based on systematically absent reflections. SHELX-97 was used for the structure solution and refinement.

D.2 Crystallographic Data of $RbSi_2P_3$

Table D.1: Atomic coordinates and equivalent displacement parameters (Å^2) for the $RbSi_2P_3$ compound.

Atom	Wyckoff	x	y	z	U_{eq}
Rb1	8*f*	0.57884(11)	0.18776(13)	0.06639(5)	0.0190(2)
Rb2	8*f*	0.32943(11)	0.43731(12)	0.06649(5)	0.0188(2)
P1	8*f*	0.0799(2)	0.1872(3)	0.06856(11)	0.0068(4)
P2	8*f*	0.1706(2)	0.4379(3)	0.43156(11)	0.0064(4)
P3	8*f*	0.1159(3)	0.4447(2)	0.18562(13)	0.0076(4)
P4	8*f*	0.3985(2)	0.4303(2)	0.31328(13)	0.0066(4)
P5	8*f*	0.3665(2)	0.1948(2)	0.18670(13)	0.0059(4)
P6	8*f*	0.1480(2)	0.1804(3)	0.31434(13)	0.0072(4)
Si1	4*e*	0	0.5606(4)	1/4	0.0083(7)
Si2	4*e*	0	0.0640(4)	1/4	0.0089(8)
Si3	8*f*	0.24825(11)	0.3125(4)	0.24997(5)	0.0053(7)
Si4	8*f*	0.22010(15)	0.06247(14)	0.13010(7)	0.0073(3)
Si5	8*f*	0.03020(14)	0.31251(15)	0.37028(7)	0.0075(3)

Table D.2: Selected angle (°) $RbSi_2P_3$.

atoms	angle(°)	atoms	angle(°)
P1—Rb1—P2	63.58(7)	P1—Rb1—P3	151.45(10)
P2—Rb1—P3	110.21(6)	P1—Rb1—P6	151.43(9)
P2—Rb1—P6	110.21(5)	P3—Rb1—P6	56.77(7)
P1—Rb1—P5	110.66(7)	P2—Rb1—P5	151.63(5)
P3—Rb1—P5	60.40(7)	P6—Rb1—P5	87.48(6)

atoms	angle(°)	atoms	angle(°)
P1—Rb1—P4	110.62(8)	P2—Rb1—P4	151.70(5)
P3—Rb1—P4	87.47(7)	P6—Rb1—P4	60.47(7)
P5—Rb1—P4	56.41(7)	P1—Rb1—P2	90.60(8)
P2—Rb1—P2	90.58(6)	P3—Rb1—P2	61.05(6)
P6—Rb1—P2	117.81(8)	P5—Rb1—P2	61.20(6)
P4—Rb1—P2	117.60(8)	P1—Rb1—Rb2	58.31(5)
P2—Rb1—Rb2	121.89(4)	P3—Rb1—Rb2	120.30(6)
P6—Rb1—Rb2	120.30(6)	P5—Rb1—Rb2	59.90(5)
P4—Rb1—Rb2	59.83(5)	P2—Rb1—Rb2	90.01(6)
P1—Rb1—Rb2	121.77(8)	P2—Rb1—Rb2	58.19(5)
P3—Rb1—Rb2	59.65(5)	P6—Rb1—Rb2	59.62(5)
P5—Rb1—Rb2	120.05(6)	P4—Rb1—Rb2	120.09(7)
P2—Rb1—Rb2	90.01(7)	Rb2—Rb1—Rb2	179.92(8)
P1—Rb1—P2	90.59(9)	P2—Rb1—P2	90.63(6)
P3—Rb1—P2	117.81(8)	P6—Rb1—P2	61.04(6)
P5—Rb1—P2	117.63(7)	P4—Rb1—P2	61.23(6)
P2—Rb1—P2	178.59(11)	Rb2—Rb1—P2^{i}	89.97(7)
Rb2—Rb1—P2^{ii}	90.00(6)	P1—Rb1—Rb2	46.75(6)
P2—Rb1—Rb2^{i}	72.52(3)	P3—Rb1—Rb2	161.49(5)
P6—Rb1—Rb2	104.82(5)	P5—Rb1—Rb2	125.62(5)
P4—Rb1—Rb2	83.89(5)	P2—Rb1—Rb2^{ii}	137.34(6)
Rb2—Rb1—Rb2^{i}	68.65(4)	Rb2—Rb1—Rb2^{ii}	111.38(4)
P2—Rb1—Rb2^{iii}	43.85(6)	P1—Rb1—Rb1	72.50(6)
P2—Rb1—Rb1^{i}	46.72(5)	P3—Rb1—Rb1	83.51(5)
P6—Rb1—Rb1	125.38(6)	P5—Rb1—Rb1	105.01(5)
P4—Rb1—Rb1	161.35(6)	P2—Rb1—Rb1^{ii}	43.86(4)
Rb2—Rb1—Rb1^{i}	111.48(5)	Rb2—Rb1—Rb1^{ii}	68.58(4)

atoms	angle(°)	atoms	angle(°)
P2—Rb1—Rb1^{iii}	137.34(7)	Rb2—Rb1—Rb1^{iii}	109.10(3)
P1—Rb2—P2	63.29(7)	P1—Rb2—P6	151.42(5)
P2—Rb2—P6	110.35(8)	P1—Rb2—P3	151.40(5)
P2—Rb2—P3	110.28(7)	P6—Rb2—P3	56.80(7)
P1—Rb2—P4	110.82(5)	P2—Rb2—P4	151.68(9)
P6—Rb2—P4	60.37(7)	P3—Rb2—P4	87.48(6)
P1—Rb2—P5	110.74(5)	P2—Rb2—P5	151.58(9)
P6—Rb2—P5	87.51(7)	P3—Rb2—P5	60.46(7)
P4—Rb2—P5	56.46(7)	P1—Rb2—P1^{i}	90.61(7)
P2—Rb2—P1	90.64(9)	P6—Rb2—P1	61.02(6)
P3—Rb2—P1	117.82(8)	P4—Rb2—P1	61.20(6)
P5—Rb2—P1	117.65(8)	P1—Rb2—Rb1^{i}	58.38(5)
P2—Rb2—Rb1	121.68(8)	P6—Rb2—Rb1	120.35(7)
P3—Rb2—Rb1	120.38(6)	P4—Rb2—Rb1	59.98(5)
P5—Rb2—Rb1	59.92(5)	P1—Rb2—Rb1^{ii}	90.01(6)
P1—Rb2—Rb1^{iii}	121.54(4)	P2—Rb2—Rb1^{i}	58.25(5)
P6—Rb2—Rb1	59.73(5)	P3—Rb2—Rb1	59.67(5)
P4—Rb2—Rb1	120.10(6)	P5—Rb2—Rb1	120.13(6)
P1—Rb2—Rb1^{iv}	90.02(7)	Rb1—Rb2—Rb1	179.92(8)
P1—Rb2—P1^{i}	90.58(6)	P2—Rb2—P1	90.58(8)
P6—Rb2—P1	117.84(8)	P3—Rb2—P1	61.04(6)
P4—Rb2—P1	117.62(8)	P5—Rb2—P1	61.17(6)
P1—Rb2—P1^{ii}	178.58(11)	Rb1—Rb2—P1^{i}	89.97(7)
Rb1—Rb2—P1^{ii}	90.01(6)	P1—Rb2—Rb2^{i}	46.77(5)
P2—Rb2—Rb2	72.35(6)	P6—Rb2—Rb2	104.78(6)
P3—Rb2—Rb2	161.48(6)	P4—Rb2—Rb2	83.98(5)
P5—Rb2—Rb2	125.70(6)	P1—Rb2—Rb2^{ii}	43.84(4)

atoms	angle(°)	atoms	angle(°)
Rb1—Rb2—Rb2^{i}	68.71(3)	Rb1—Rb2—Rb2^{ii}	111.26(5)
P1—Rb2—Rb2^{iii}	137.35(7)	P1—Rb2—Rb1	72.34(3)
P2—Rb2—Rb1^{ii}	46.78(6)	P6—Rb2—Rb1	83.55(5)
P3—Rb2—Rb1	125.46(5)	P4—Rb2—Rb1	105.00(5)
P5—Rb2—Rb1	161.38(5)	P1—Rb2—Rb1^{v}	43.86(6)
Rb1—Rb2—Rb1^{i}	111.36(4)	Rb1—Rb2—Rb1^{ii}	68.62(4)
P1—Rb2—Rb1	137.36(6)	Rb2—Rb2—Rb1	42.64(3)
Si4—P1—Si5	107.35(11)	Si4—P1—Rb2	94.90(8)
Si5—P1—Rb2	157.75(10)	Si4—P1—Rb1	158.21(12)
Si5—P1—Rb1	94.44(10)	Rb2—P1—Rb1	63.31(5)
Si4—P1—Rb2^{i}	90.44(10)	Si5—P1—Rb2^{i}	90.40(9)
Rb2—P1—Rb2^{i}	89.38(7)	Rb1—P1—Rb2^{i}	89.39(8)
Si4—P1—Rb2^{ii}	90.42(9)	Si5—P1—Rb2^{ii}	90.42(10)
Rb2—P1—Rb2^{ii}	89.42(6)	Rb1—P1—Rb2^{ii}	89.39(9)
Rb2—P1—Rb2^{iii}	178.58(11)	Si4—P2—Si5	107.19(11)
Si4—P2—Rb2	94.84(10)	Si5—P2—Rb2	157.97(12)
Si4—P2—Rb1	158.41(10)	Si5—P2—Rb1	94.41(8)
Rb2—P2—Rb1	63.56(5)	Si4—P2—Rb1^{i}	90.44(10)
Si5—P2—Rb1^{i}	90.47(9)	Rb2—P2—Rb1^{i}	89.44(9)
Rb1—P2—Rb1^{i}	89.42(6)	Si4—P2—Rb1^{ii}	90.41(9)
Si5—P2—Rb1^{ii}	90.36(10)	Rb2—P2—Rb1^{ii}	89.37(8)
Rb1—P2—Rb1^{ii}	89.37(6)	Rb1—P2—Rb1^{iii}	178.59(11)
Si5—P3—Si1	106.57(12)	Si5—P3—Si3	106.57(14)
Si1—P3—Si3	104.08(14)	Si5—P3—Rb1	90.9(1)
Si1—P3—Rb1	93.93(11)	Si3—P3—Rb1	149.73(12)
Si5—P3—Rb2	90.92(9)	Si1—P3—Rb2	149.80(14)
Si3—P3—Rb2	93.82(8)	Rb1—P3—Rb2	60.67(6)

atoms	angle(°)	atoms	angle(°)
Si4—P4—Si2	106.40(14)	Si4—P4—Si3	106.16(12)
Si2—P4—Si3	105.75(14)	Si4—P4—Rb2	90.45(9)
Si2—P4—Rb2	93.55(8)	Si3—P4—Rb2	149.31(13)
Si4—P4—Rb1	90.34(9)	Si2—P4—Rb1	149.40(11)
Si3—P4—Rb1	93.40(11)	Rb2—P4—Rb1	60.19(6)
Si4—P5—Si3	106.32(12)	Si4—P5—Si1	106.26(14)
Si3—P5—Si1	105.81(14)	Si4—P5—Rb1	90.39(9)
Si3—P5—Rb1	149.29(13)	Si1—P5—Rb1	93.47(8)
Si4—P5—Rb2	90.44(9)	Si3—P5—Rb2	93.42(10)
Si1—P5—Rb2	149.32(11)	Rb1—P5—Rb2	60.19(5)
Si5—P6—Si2	106.74(12)	Si5—P6—Si3	106.57(13)
Si2—P6—Si3	104.15(14)	Si5—P6—Rb2	90.91(9)
Si2—P6—Rb2	93.83(11)	Si3—P6—Rb2	149.68(11)
Si5—P6—Rb1	90.82(10)	Si2—P6—Rb1	149.68(14)
Si3—P6—Rb1	93.82(8)	Rb2—P6—Rb1	60.65(6)
P3—Si1—P3	117.2(2)	P3—Si1—P5^{i}	104.91(8)
P3—Si1—P5^{ii}	111.66(11)	P3—Si1—P5^{iii}	111.66(11)
P3—Si1—P5^{iv}	104.91(8)	P5—Si1—P5	106.1(2)
P5—Si1—P5	106.1(2)	P4—Si2—P4	106.2(2)
P4—Si2—P6^{i}	104.89(8)	P4—Si2—P6^{ii}	111.76(11)
P4—Si2—P6^{iii}	111.76(11)	P4—Si2—P6^{iv}	104.89(8)
P6—Si2—P6	117.0(2)	P6—Si3—P3	117.05(12)
P6—Si3—P5	111.64(19)	P3—Si3—P5	104.98(9)
P6—Si3—P4	105.01(9)	P3—Si3—P4	111.6(2)
P5—Si3—P4	106.11(12)	P2—Si4—P1	106.97(10)
P2—Si4—P4	108.84(12)	P1—Si4—P4	108.61(10)
P2—Si4—P5	108.75(10)	P1—Si4—P5	108.71(11)

atoms	angle(°)	atoms	angle(°)
P4—Si4—P5	114.69(10)	P1—Si5—P2	107.57(10)
P1—Si5—P6	108.40(11)	P2—Si5—P6	108.60(11)
P1—Si5—P3	108.41(11)	P2—Si5—P3	108.41(11)
P6—Si5—P3	115.19(10)	-	-

Symmetry notes: (i) x, y, z; (ii) $-x, y, -z+\frac{1}{2}$; (iii) $x+\frac{1}{2}, y+\frac{1}{2}, z$; (iv) $-x+\frac{1}{2}, y+\frac{1}{2}, -z+\frac{1}{2}$; (v) $-x, -y, -z$; (vi) $x, -y, z-\frac{1}{2}$; (vii) $-x+\frac{1}{2}, -y+\frac{1}{2}, -z$; (viii) $x+\frac{1}{2}, -y+\frac{1}{2}, z-\frac{1}{2}$.

Table D.3: Anisotropic Displacement Parameters (Å^2) of $RbSi_2P_3$ compound from single crystal data.

Atom	U_{11}	U_{22}	U_{33}	U_{12}	U_{13}	U_{23}
Rb1	0.0202(6)	0.0198(4)	0.0171(6)	0.0035(4)	0.0030(4)	0.0010(4)
Rb2	0.0201(6)	0.0197(4)	0.0167(6)	0.0023(4)	0.0031(4)	-0.0007(4)
P1	0.0091(12)	0.0095(8)	0.0021(11)	0.0072(9)	0.0018(8)	0.0021(8)
P2	0.0094(12)	0.0080(8)	0.0019(11)	-0.0053(9)	0.0008(8)	0.0015(8)
P3	0.0077(9)	0.0067(8)	0.0083(9)	0.0026(6)	0.0006(6)	-0.0001(7)
P4	0.0062(8)	0.0061(7)	0.0076(9)	-0.0018(6)	0.0012(6)	-0.0015(6)
P5	0.0062(8)	0.0054(7)	0.0067(9)	0.0004(6)	0.0028(6)	-0.0012(6)
P6	0.0078(9)	0.0071(7)	0.0074(9)	-0.0010(6)	0.0040(6)	0.0008(7)
Si1	0.0065(19)	0.0108(13)	0.008(2)	0.000	0.0026(14)	0.000
Si2	0.008(2)	0.0108(13)	0.009(2)	0.000	0.0033(14)	0.000
Si3	0.0067(18)	0.0014(10)	0.0076(18)	-0.0005(4)	0.0006(12)	-0.0010(4)
Si4	0.0077(6)	0.0066(6)	0.0078(7)	0.0018(5)	0.0017(5)	0.0002(5)
Si5	0.0077(6)	0.0062(6)	0.0088(7)	-0.0018(5)	0.0022(5)	0.0001(5)

D.3 Elemental analysis of $RbSi_2P_3$

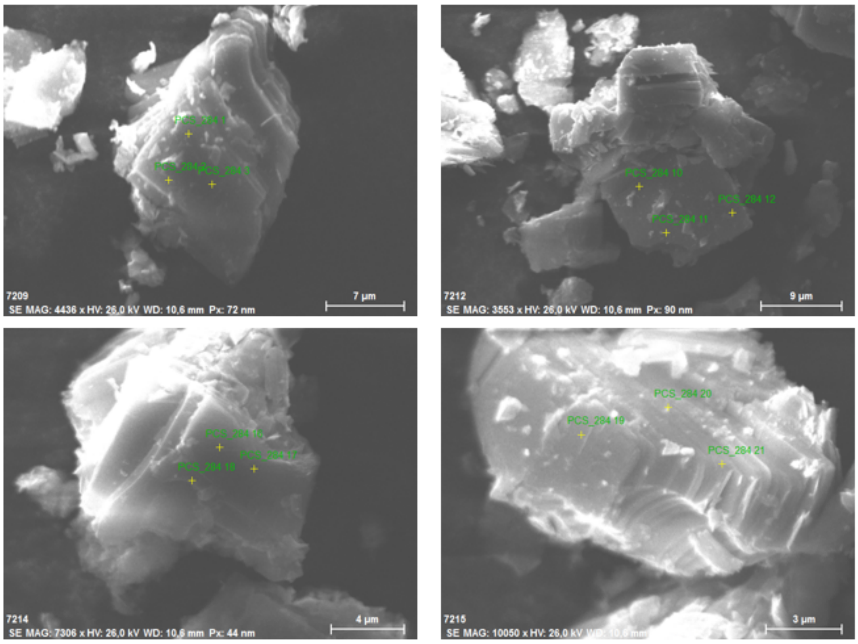

Figure D.1: Representative scanning electron microscopic photographs of $RbSi_2P_3$

Table D.4: Elemental analysis by EDX of $RbSi_2P_3$, signals of oxygen were not taken into account due to hydrolysis.

Spektrum	Si / atom-%	P / atom-%	Rb / atom-%
EDX point 1 / atom-%	31.01	49.63	19.36
EDX point 2 / atom-%	29.26	54.02	16.72
EDX point 3 / atom-%	33.54	48.01	18.45
EDX point 4 / atom-%	30.38	51.88	17.74
EDX point 5 / atom-%	29.91	53.15	16.94
EDX point 6 / atom-%	28.92	53.39	17.68
EDX point 7 / atom-%	30.63	47.92	21.45
EDX point 8 / atom-%	31.61	50.75	17.64
EDX point 9 / atom-%	30.48	48.71	20.82
EDX point 10 / atom-%	28.57	55.08	16.35
EDX point 11 / atom-%	32.77	48.46	18.77
EDX point 12 / atom-%	29.12	53.64	17.24
Average / atom-%	30.39	51.39	18.22
Calculated / atom-%	33.33	50.00	16.67

D.4 X-ray powder diffraction pattern of $Rb_{1.14}Si_{1.86}Al_{1.14}P_3$

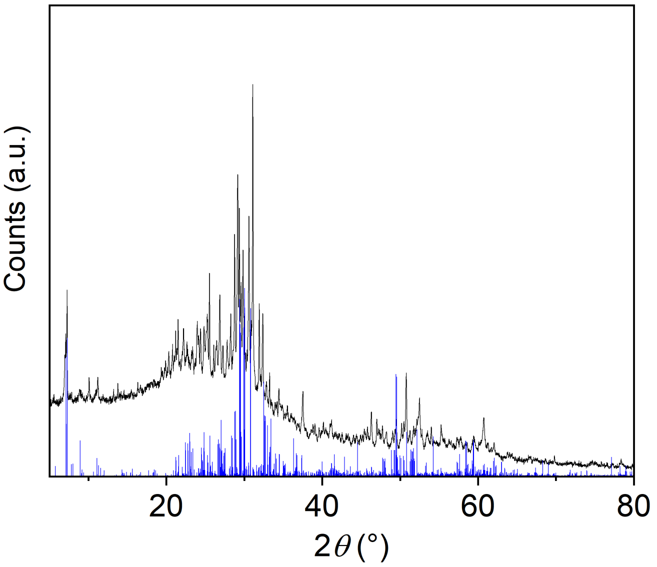

Figure D.2: X-ray powder diffraction pattern (black, Cu$K\alpha$ radiation) of $Rb_{1.14}Si_{1.86}Al_{1.14}P_3$ compared with the known pattern of KSi_2P_3-*tI960* (blue).